Semiconducting Devices and Nanomaterials: Insight from Computational Chemistry

by

Alexandra Ross McIsaac

B.S., Chemistry
University of Chicago, 2016

Submitted to the Department of Chemistry
in partial fulfillment of the requirements for the degree of

Doctor of Philosophy in Chemistry

at the

MASSACHUSETTS INSTITUTE OF TECHNOLOGY

September 2021

Author .....
Department of Chemistry
June 17, 2021

Certified by .....
Troy Van Voorhis
Department Head and Haslam and Dewey Professor of Chemistry
Thesis Supervisor

Accepted by .....
Adam Willard
Associate Professor
Graduate Officer

This doctoral thesis has been examined by a Committee of the
Department of Chemistry as follows:

Professor Adam Willard .....
Chair, Thesis Committee
Associate Professor of Chemistry

Professor Troy Van Voorhis .....
Thesis Supervisor
Department Head and Haslam and Dewey Professor of Chemistry

Professor Bin Zhang .....
Member, Thesis Committee
Pfizer-Laubach Career Development Assistant Professor

Semiconducting Devices and Nanomaterials: Insight from Computational Chemistry

by

Alexandra Ross McIsaac

Submitted to the Department of Chemistry
on June 17, 2021, in partial fulfillment of the
requirements for the degree of
Doctor of Philosophy in Chemistry

Abstract

In the past two decades, new technologies such as organic light emitting diodes (OLEDs) and quantum dots have emerged as promising candidates for applications from displays to solid state lighting. Many phenomenological and empirical models exist to explain the properties of these materials, and have succeeded in describing some of their properties. However, both of these systems have high degrees of disorder; for OLEDs, this manifests due to the molecular makeup of the emitting layer, and for quantum dots, due to their highly non-crystalline surface. Explaining properties that arise due to this disorder requires models that go beyond the phenomenological, in particular, it requires methods that can explicitly model the atoms and molecules causing disorder. In this thesis, we investigate the properties of quantum dot surfaces using density functional theory, which is an atomistic, all-electron electronic structure method. This allows us to identify specific features on the quantum dot surface and tie these features to the optical properties of the quantum dot. We find that undercoordinated surface atoms on the surface of CdSe can cause optical traps even when there are no traps in the ground state band structure, show that surface reorganization and annealing can significantly improve the optical properties of CdSe, and also explore sources of traps in CdSe/CdS core/shell quantum dots. In addition, we develop a model for OLED kinetics, which is able to incorporate the effects of molecular disorder but is very computationally efficient. We show that this model can extract molecular rate constants from a device-level measurement, and can help identify sources of efficiency loss in OLED devices.

Thesis Supervisor: Troy Van Voorhis
Title: Department Head and Haslam and Dewey Professor of Chemistry

Acknowledgments

First and foremost I would like to thank my advisor Prof. Troy Van Voorhis. Troy gave me a chance to learn theoretical chemistry when I was just a freshman in college, and has been a wonderful mentor throughout my PhD. He is a brilliant scientist and a genuinely caring person, which has made working in his group for 5 years of graduate school extremely rewarding. I would also like to thank my other mentors throughout my career. Thank you to my thesis committee chair Prof. Adam Willard and thesis committee memeber Prof. Bin Zhang for all of the advice throughout the years. Thank you to Prof. David Mazziotti at UChicago for being an excellent undergraduate advisor and to Prof. Laurie Butler at UChicago for sparking my interest in physical chemistry. Thank you to Anthony Schlimgen, Chad Heaps, Takahiro Sawano, and Mike Mavros for being wonderfully supportive grad student and postdoc mentors to me when I was an undergrad, I would not have come to love research without their patient and kind guidance. And thank you to my high school chemistry teachers Rebecca Jackman and Michelle Cyrier for inspiring me to study chemistry in the first place, and my high school advisor Jessica Wasilewski for always encouraging me to pursue STEM.

I would like to thank all the members of the Van Voorhis group, who have taught me so much and shared in many ups and downs of graduate school. Thank you in particular to James Shepherd and Nadav Geva for mentoring me in my projects during my first few years in the group. To Henry Tran, Andrew Kim, Ali Raeber, Jacq Tan, Oinam Meitei, Natasha Seelam, Nathan Ricke, Hongzhou Ye, Zhou Lin, Tianyu Zhu, Ricardo Pedro, Alex Kohn, Piotr de Silva, Valerie Vassier Welborn, Leah Weisburn, and Ezra Alexander, thank you for your many helpful suggestions, support, and laughter throughout the years. Thank you to Lin Rogers and Ben Chien for the opportunity to be your mentor, I learned so much from you guys. A special thanks to Tami Goldzak and Yael Cytter, my fellow members of the "girls' room" (our very rare all-woman theory office), as well as the mouse that we shared the office with—I like to think it was a female mouse. Thanks for all the GNIs, hours of entertainment when

we should have been working, and many trips to the vending machine! And thank you also to all of the members of the Zoo, in particular Andrew Latham, Ardy, Maria, Amogh, Aditya, Yifeng, Helena, Michiel, Liza, Wendu, Zhongling, and Dina, for all the Fikas, lunches, and friendship. And of course, thank you to everyone in the PChem 2016 cohort—the many long PSet nights and much more civilized pre-seminar catch ups will never be forgotten. Thank you to Markus Einzinger and Matthias Ginterseder for fruitful experimental collaborations, and to Katie Shulenberger for requesting the seemingly impossible quantum dot calculations that began this thesis! And thank you to all of the administrative staff in the chemistry department, and particularly Li Miao, Jennifer Weisman, Rebecca Teixeira, Jay Matthews, Michele Harris, and Shannon Wagner, without whom my research would not have been possible, as the Van Voorhis group and the department would not function without them.

Thank you additionally to all of my friends and family who have made this journey possible. Thanks to Ray, Michael, Crystal, Megan, Mari, Tom, and Audrey–thank you for all the countless trips to the Muddy, dance parties, dinners out, sing alongs, and more. Thank you to Kaitlyn and Adam for many game nights, ski trips, hang outs, and most importantly for letting me hang out with your cats. Thanks to Julia for always being down for anything from a night on the town to a Love Island marathon at home, and for a friendship that is now old enough to drink with us. Thanks to Emma, Darcy, and Anaïs for being wonderful roommates and friends, and for making me remember that there are things going on outside of grad school (or at least, outside of MIT...). Thanks to Emily for indulging in Taylor Swift conspiracies with me, and to Alina for always pretending it hasn't been years since we talked last. Thanks to Mariyam, Rohan, Adam, Matt, Yujia, and Ruben for all the visits, long phone/Skype calls, support, and reminiscing. Thank you to Kade for always being around to commiserate. To Amr, thank you for always being there for me through everything and always being able to put a smile on my face. Thank you to my mom and dad, whose unwavering love and support has gotten me through many difficult times and who are always encouraging me. (Also, thanks for all the brownie mix from Costco). Thank you to my brother Colin for always keeping me young. Thank you

to my grandparents for always pretending to be interested in what I'm working on, and cheering me on even when they weren't quite sure what they were cheering for. I don't have the words to describe how grateful I am for all of your support, I couldn't have done it without you!

Contents

Chapter 1

Introduction

This thesis focuses on using computational methods, specifically density functional theory and kinetics modeling, to understand the properties of electrons and excitons in semiconducting materials. In particular, we will discuss the electronic structure of CdSe and CdSe/CdS quantum dots studied using both density functional theory and time-dependent density functional theory, and we will develop a new model to describe the kinetics of excitons and charge carriers in organic light emitting diodes. In this chapter, we focus on the pre-requisite background material that underlies the coming chapters. In section 1.3 of this chapter, we outline the remaining chapters.

1.1 Quantum dots

1.1.1 Physical structure of quantum dots

Quantum dots (QDs) are nanocrystals of semiconducting material that are typically 1–10 nm in size.[1] Due to their tunable spectrum and high luminescence, QDs have been successfully used in many applications and optoelectronic devices,[2] such as solar cells,[3–6] photodetectors,[7,8] light emitting diodes,[9,10] displays,[11] and biological sensing and imaging.[12,13] Many different semiconducting materials can be made into quantum dots, some common types include CdSe, PbS, InP, InGaP, CdS, ZnSe, and many more.[14]

There are two major categories of quantum dot: core-only and core/shell. A core-only quantum dot usually contains 2 major regions: the core, or the internal part of the QD whose geometry typically resembles that of the bulk semiconducting material, and the surface, which typically deviates significantly from the bulk structure.[1,14] A core/shell quantum dot typically contains 4 regions: the core, which is the same as the core of a core-only dot; the interface, which is where the core and the shell meet; the shell, which is made up of a different kind of semiconducting material than the core and exists to shield the core from the surface/environment; and the surface of the shell, which again deviates significantly from the bulk structure of the shell.[14,15] In addition to these regions, or perhaps better viewed as part of the surface, both core-only and core/shell QDs will typically have organic ligands attached to the surface both to solubilize the QDs and to passivate the surface. These ligands are typicaly Lewis bases, and include primary amines, trioctylphosphine oxide (TOPO), carboxylic acids such as oleic acid, and others.[14] Each of these different components of the quantum dot affects their electronic structure.

1.1.2 Core electronic structure

The electronic structure of quantum dots is intermediate between that of an atom/molecule and that of a solid,[14] and is illustrated in the left panel of Fig. 1.1. Near the band edge (in solid state parlance) or frontier orbitals (in molecular quantum chemistry parlance), there are discrete states as you would see in an atom or molecule. Moving to lower energies in the valence band (or occupied orbitals) and higher energies in the conduction band (or virtual orbitals), the orbitals begin to form a continuum as would be seen in a solid. The terminology for QD orbitals is typically taken from the parlance of solid state chemistry; the occupied orbitals are referred to as the valence band (VB), the highest occupied molecular orbital (or highest occupied orbital delocalized over the core) is referred to as the valence band maximum (VBM), the virtual orbitals are referred to as the conduction band (CB), and the lowest unoccupied molecular orbital (or lowest unoccupied orbital delocalized over the core) is referred to as the conduction band minimum (CBM).

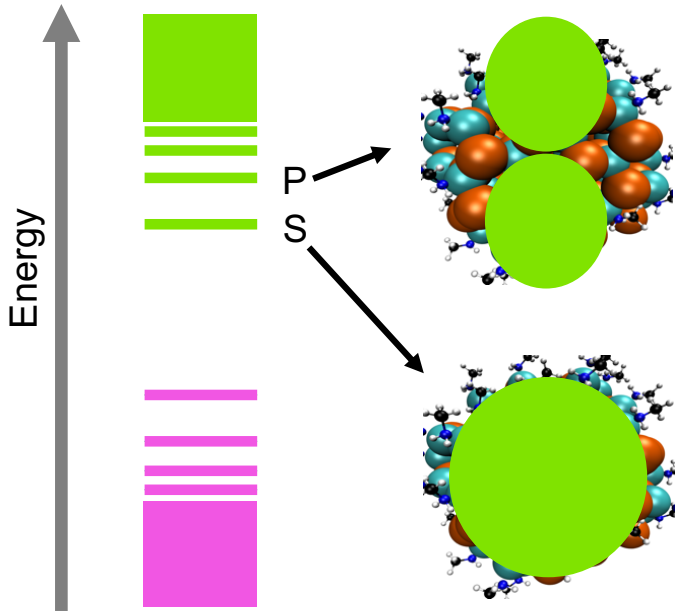

Figure 1.1: Left: MO diagram illustrating the electronic structure of a core-only QD. Green orbitals indicate the conduction band or electron states, and magenta orbitals indicate the valence band or hole states. Right: Cartoon depiction of the S and P states in a CdSe QD.

The discrete states at the edge of the valence and conduction bands arise because the size of a quantum dot is smaller than the Bohr exciton radius for the material, leading to a confinement effect and giving rise to quantum dots' interesting optical properties.[1,14,16,17] These states are generally described using effective mass models or k dot p theory; both of these Hamiltonians resemble the Hamiltonian for the hydrogen atom or a particle in a spherical well, and thus give rise to wavefunctions featuring the spherical harmonics.[1] This description leads to "S" and "P" states for the quantum dot, which qualitatively resemble S and P atomic orbitals, as shown in the right panel of Fig. 1.1. This also gives rise to a band gap that is decreases as the QD size increases, similar to a particle in a spherical well model. As a result, the emission energy of the QD is size-dependent, with larger QDs emitting lower energy light and smaller QDs emitting higher energy light, so the band gap and emission properties can be tuned based on the size of the QD.

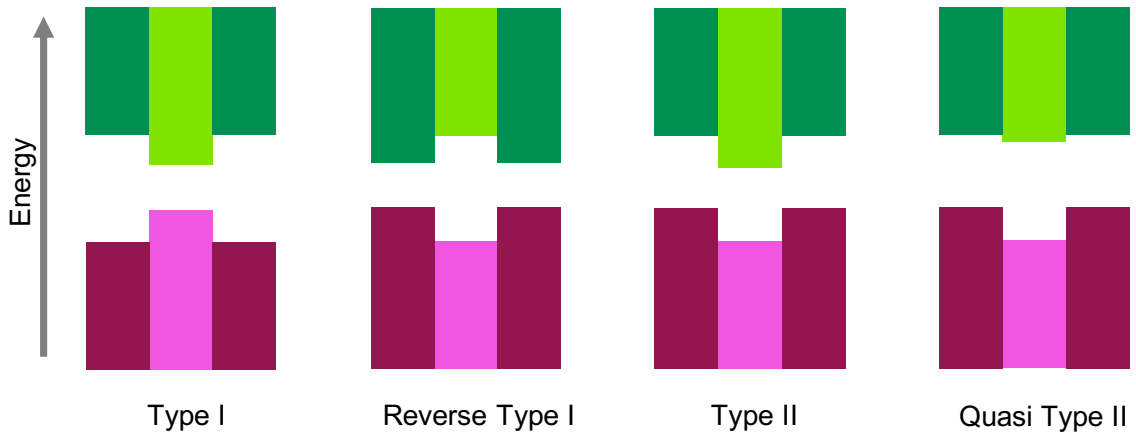

Figure 1.2: Diagram showing the band alignment of different types of core/shell quantum dots. Dark green represents the conduction band of the shell, light green represents the conduction band of the core, maroon represents the valence band of the shell, and magenta represents the valence band of the core. The arrow indicates the relative energy of the electron state, while the hole state's energy will be reversed. For simplicity, we do not show the discrete S and P states as separate from the bands.

1.1.3 Core/shell electronic structure

The electronic structure of core/shell QDs is also typically understood in the context of the effective mass approximation described in section 1.1.2, with S and P atomic-like envelope functions for the electron and hole.[18–20] However, the electronic structure now depends on the identity of both the core and shell material; in particular, the relative energy of the VBM and CBM of the core and shell. There are 4 types of core/shell QDs, based on the relative energy of the VBM and CBM, described below and summarized in Fig. 1.2. First, it is important to note that in the parlance of excitonics, while an electron has lower energy in a lower energy orbital, a hole counterintuitively has lower energy in a higher energy orbital.[15] Thus, if one material (say the core) has a higher energy VBM than the other material (say the shell), that means the hole will have *lower* energy in the core material than in the shell material.

A type I core/shell QD means that the hole and electron are confined to the core of the QD. This happens when the hole and electron energies are both lower in the

core than the shell (core VBM energy > shell VBM energy and core CBM energy < shell CBM energy).[15,21] In a type I core/shell QD, the electronic structure of the material is primarily controlled by the properties of the core, and the shell simply acts as a way to passivate the surface of the core.[15]

In a reverse-type I core/shell QD, both the hole and electron are located in the shell of the QD. This happens when the hole and electron energy are both lower in the shell than in the core (core VBM energy < shell VBM energy and core CBM energy > shell VBM energy).[15] In this case, the optical properties are primarily controlled by the shell material.

In a type II core/shell QD, the electron and hole are spatially separated in the QD. One way this can arise is if the hole energy is lower in the core and the electron energy is lower in the shell (core VBM energy > shell VBM energy and core CBM energy > shell CBM energy), leading to the hole state being located in the core and the electron state being located in the shell.[15] The opposite scenario is also possible, leading to the electron being located in the core and the hole in the shell.[15] In either case, there is a strong separation of carriers with very little overlap between the electron and the hole.

In a quasi-type II core/shell QD, one carrier is delocalized over the core and shell while the other is confined to one area of the QD. One situation where this could arise is if the hole energy is lower in the core than the shell (core VBM energy > shell VBM energy) and the electron energy is quasi-degenerate in the core and the shell (core CBM energy $\approx$ shell CBM energy), so the hole is confined to the core but the electron is delocalized over core and shell. Alternatively, the reverse scenario can occur, leading to the hole being delocalized over the core and shell with the electron confined to the core.[15,21] Other alignment schemes can also exist, but for any of these scenarios, the QD will exhibit a red shift of the band gap with increasing shell thickness, and a decrease in carrier overlap with increasing shell thickness.[15]

1.1.4 Surface traps

Because quantum dots are so small, a large percentage of the atoms in the QD are on the surface. This is more pronounced for smaller QDs, as the surface to bulk ratio increases as the size of the dot decreases.[22] In the core of the QD, meaning away from the surface, the geometry is expected to resemble that of the bulk crystal structure of the solid material. However, on the surface, the crystal structure is interrupted, leading to features such as dangling bonds, vacancies, charging, and adsorbed atoms.[14] These features can lead to trap states on the surface of the QD. Surface trap states can be desirable in some cases; they have been shown to facilitate catalysis[23] and energy transfer to nearby ligands.[24,25] However, they are typically regarded as a nuisance, as they compete with radiative recombination of the exciton, leading to reduced photoluminescence quantum yield (PLQY)[14] and blinking.[1,26,27]

Numerous strategies exist to reduce the presence of surface traps on QDs, which is desirable for the vast majority of QD applications. One common strategy is improving the surface passivation by changing the ligands or adding an inorganic shell, to bind to surface atoms.[14] Surface electron traps are often caused by dangling bond orbitals on cationic species of the QD surface (e.g. Cd in CdSe) and hole traps are often caused by dangling bond orbitals on anionic species (e.g. Se in CdSe).[28–32] Surface atoms bond with ligands or shell materials to fill danging bond orbitals, removing traps associated these orbitals.[28–32] Typical organic ligands used in experiments are relatively bulky, so achieving full surface coverage is impossible; ligands lead to a reduction in the number of surface states but not their elimination.[14] In addition, surface ligands are usually electron donors that only bind to the cationic species of the QD; this leads to the elimination of electron traps, but hole traps remain a problem.[33,34]

On the other hand, an inorganic shell material is theoretically able to fully passivate both the cationic and anionic surface species. This could involve coating the surface with a CdX_2 (X=Br, Cl, F) "ligand,"[35] which for CdSe would create a core-only QD with a Cd-rich, fully passivated surface. Alternatively, coating the core with a shell of another material (such as CdSe coated with CdS or ZnS), would create

a core/shell QD.[15] Passivation with an inorganic shell leads to strongly improved optical properties, including high PLQY, reduced blinking, and shorter exciton lifetimes.[14,36,37] For a core/shell QD, in principle, there can still be surface defects on the surface of the shell; however, in most systems the exciton is intentionally confined to the core, leading to decoupling of the bulk exciton from surface defects.[14,38] On the other hand, introducing an inorganic shell can create defects at the interface between the core and shell, due to problems during shell growth or poor alignment of the crystal structures between the core and the shell.[21] These defects have been shown to cause behavior similar to surface traps.[21]

Another common strategy to remove surface traps is annealing. This refers to heating the QD in order to promote the surface atoms to rearrange, eliminating adsorbed atoms, dangling bonds, or other defects.[14] It has been shown for both core/shell CdSe/CdS[36] and core-only CdSe[39] to strongly improve the optical properties, including narrower full width half max, reduced to eliminated blinking, and higher PL intensity.

1.1.5 Electronic structure methods for quantum dots

Due to their large size, simulating QDs with electronic structure theory can be quite challenging. In particular, one must balance accuracy of the method with simulating a realistically sized QD. In order to simulate large, experimentally-sized QDs, relatively simple methods must be used, such as effective mass theory or k dot p theory.[1,17] Typically these methods will ignore any atomistic details of the QDs, taking into account only the lattice crystal structure of the bulk, material-specific parameters such as the effective mass, and the size of the QD. They are also empirical, as the parameters that cannot be obtained from the bulk solid are fit to experimental data.[17,40] However, they do describe the rough features of QD optical spectra well,[1,16] and can be used to study very large QDs.

One step more sophisticated would be methods such as semiempirical pseudopotentials[41] or tight binding,[42] which balance fast computation time with taking into account some atomic-level features of the QDs. With both methods, the user can

specify the atomic positions of the QD explicitly, allowing for some atomistic detail. For tight binding, each atom is described using only its valence orbitals, typically an s orbital, 3 p orbitals, and a virtual s* orbital, and sometimes others to simulate surface defects.[29] Each atom and its orbitals can only interact with its nearest neighbors or sometimes second nearest neighbors, with all other atomic interactions neglected.[1] With semiempirical pseudopotentials, the electrons associated with each atom are described using a pseudopotential that is parameterized according to both experimental results and density functional theory (DFT) within the local density approximation (LDA).[41] Then the properties of the QD are obtained by solving the single-particle Schrödinger equation for the system. The major benefit of both methods is that they take into account individual atoms explicitly, allowing for consideration of the surface of the QD or deviation from the bulk crystal structure. These models generally give relatively accurate results for describing QD optical properties, with more detail than the effective mass methods, but are still very simplistic.[1]

The most sophisticated electronic structure method that can be realistically used to simulate QDs is density functional theory (DFT), which allows for the simulation of reasonably sized (1–3 nm diameter) quantum dots at reasonable accuracy.[22,43] The accuracy (and cost) of DFT can be tuned by selecting a density functional, anywhere from the simplest local density approximation (LDA)[44,45] to a high-cost range-separated functional (such as ω-PBE)[46] have been used. One significant problem with DFT is large errors in calculating band gap due to delocalization error, so typically a DFT functional will be chosen based on its comparison to the experimental band gap. In particular, it has been shown that a hybrid functional (such as PBE0 or B3LYP) is needed to reproduce the band gap of QDs with reasonable accuracy; LDA and GGA functionals significantly underestimate the band gap and range-separated hybrids significantly overestimate the band gap.[46] Typically the core electrons of the transition metal atoms will be treated with an effective core potential (ECP) in order to lower the computational cost as well as account for relativistic effects, however, all other electrons are treated explicitly.[43] In addition, realistic ligands can be added to these calculations and modeled with explicit electrons, allowing for the exploration of

many different types of properties that cannot be explored with other methods such as ligand binding energies,[28] ligand binding motifs,[47] or the effects of different ligands on the QD.[32]

Many DFT studies of quantum dots will focus on ground state properties, such as the orbital density of states (DOS)/band structure. The ground state DOS can give information about the band gap of the QD as well as the presence of any transport traps for electrons or holes, but can only approximate the optical properties. To really probe the optical properties of QDs with DFT, an excited state method like time dependent DFT (TDDFT) must be used.[43] TDDFT allows for linear combinations of excitations, and thus goes beyond the ground state orbital picture of approximating the first excitation using the HOMO and LUMO.[48] This is especially important for DFT, because the DFT Kohn-Sham orbitals are not physical, and are simply a construction to simplify the calculation of the kinetic energy. However, TDDFT is quite expensive, which often limits its use to relatively small QDs.

1.1.6 Electronic structure of core-only CdSe quantum dots

Chapters 2 and 3 focus on core-only CdSe QDs. CdSe QDs can exist in either wurtzite or zinc blende structures, although this thesis will focus on wurtzite CdSe. CdSe has a bulk band gap of 1.8 eV, but CdSe QDs can emit anywhere between 1.8 eV to 3 eV depending on their size.[17] The optical spectrum of CdSe quantum dots are generally well described using effective mass theory, however more sophisticated theoretical methods are needed to explain surface effects in these systems.[1,22] There have been a number of experimental works investigating surface states in CdSe, suggesting that hole traps associated with Se atoms or Se-rich QDs are prevalent experimentally.[33,49–53] Many theoretical studies using tight binding,[29,54] semiempirical pseudopotentials,[30,31,55] and density functional theory[32,35,44,45,47,56–60] have been conducted. A number of these studies investigate the role of dangling bonds in creating surface traps in the ground state DOS, finding that undercoordinated Cd atoms can create electron traps (trap orbitals that are unoccupied), and undercoordinated Se atoms can cause hole traps (trap orbitals that are occupied).[29–31,35,44,45] DFT studies

using the local density approximation have also confirmed that annealing, or "self-healing" as it is termed in the theoretical literature, will lead to significant surface reorganization on the QD that will saturate dangling bonds and eliminate trap states from the DOS even for QDs without ligands.[44,45] In addition, DFT studies have successfully reproduced the experimental results that for core-only CdSe, primary amines are the best organic ligand,[28,61] and Cd-rich dots or CdX_2 ligands are the best surface passivation.[35,37,50] There have been a few studies using TDDFT to investigate the excited states of CdSe,[32,57,62,63] however the vast majority of DFT studies focus on the ground state. The exploration of excited state properties of core-only CdSe QDs is largely an open question within the electronic structure literature.

1.1.7 Electronic structure of core/shell CdSe/CdS quantum dots

Chapter 4 focuses on core/shell CdSe/CdS QDs. CdSe/CdS core/shell quantum dots are tunable between type I and quasi-type II QDs.[15,64,65] For quasi-type II CdSe/CdS QDs, the hole is confined to the core and the electron is delocalized over both the core and the shell.[15] Both types of CdSe/CdS show increased PLQY and decreased blinking compared to core-only CdSe,[36,64,65] which is attributed to the fact that the shell passivates the core Se atoms and separates the hole wavefunction from any traps on the surface of the shell, and the surface Cd atoms are passivated by the shell (type I) or organic ligands (quasi-type II), removing any electron traps.

CdSe and CdS both have wurtzite crystal structures and only a very small (4%) mismatch in lattice constant, leading to few to no traps at the interface between the core and the shell.[20] However, despite improved PLQY and blinking behavior, some CdSe/CdS QDs still show some blinking and other properties indicative of trapped hole states.[20,66–68] Structures with a very thick shell have been used to eliminate this behavior,[38] leading to the hypothesis that these traps arise from the hole tunneling into the shell and getting trapped in surface defects,[20] despite the structure being formally type I or quasi-type II with the hole confined to the core. The probability

of a hole tunneling through the potential barrier between the core and the shell will decrease with increasing shell thickness, explaining the observed behavior.

The vast majority of theoretical work on CdSe/CdS core/shell structures has been conducted with tight binding methods,[18–20] although a few studies have been published using LDA.[69–71] This is because of the large size of core/shell QDs; modeling a reasonably sized core-only QD is already expensive, and the number of atoms in the QD grows quickly with increasing radius, making even a small core/shell QD hundreds of atoms before accounting for ligands. Most of these studies focus on the nature of the band edge orbitals for CdSe/CdS with no ligands or with pseudohydrogens passivating the surface, determining type I vs quasi-type II alignment and size dependence of the band gap. Little if any work has explored more sophisticated DFT methodologies or realistic surface passivation for CdSe/CdS, despite the importance of using a hybrid functional for the correct description of core-only CdSe.

1.2 OLEDs

1.2.1 Background

Organic light-emitting diodes (OLEDs) are light-emitting devices whose emission source is made up of organic molecules. A typical OLED is shown in Fig. 1.3, and consists of an anode, a cathode, an emitting layer, and often other layers such as hole- or electron-transport layers to improve the efficiency of the device.[72] They have been widely adopted for display purposes, and are promising candidates for applications in organic lasing[73–79] and solid-state lighting.[80–86]

1.2.2 Efficiency roll-off

OLEDs designed for displays do not need to be very bright, and have been engineered to operate at relatively low current density. However, newer applications like lasing or lighting require significantly higher brightness than displays, creating demand for OLEDs that operate at significantly higher current density than is needed

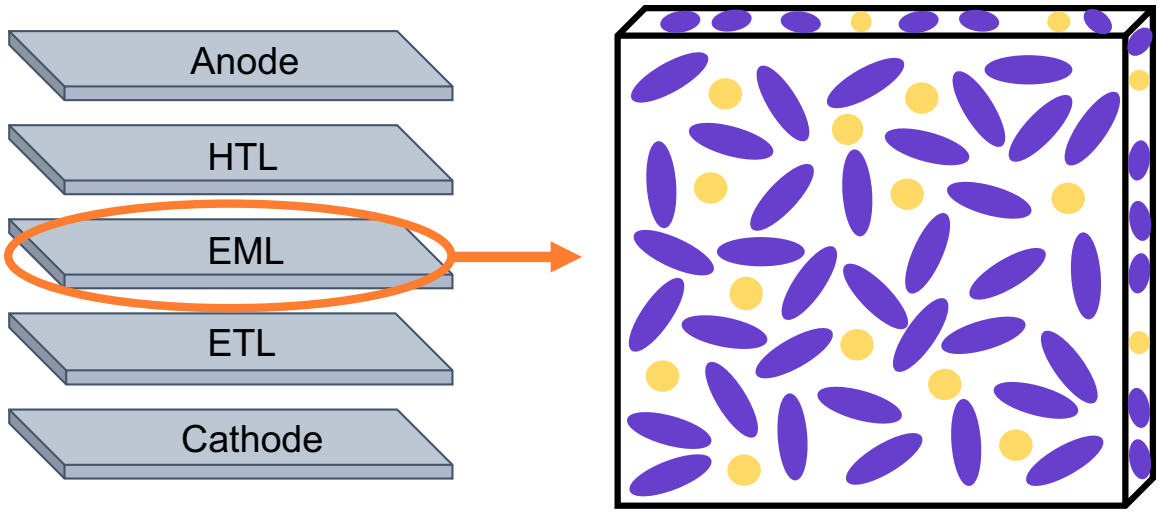

Figure 1.3: Cartoon illustrating the makeup of an OLED device. The left part of the figure shows the different components of an OLED, consisting of an anode, a hole transporting layer (HTL), an emitting layer (EML), an electron transport layer (ETL), and a cathode. The right part of the figure zooms in on the emitting layer, which is a host/guest system made up of organic molecules. The guest molecules are typically responsible for emission.

for displays. At high brightness and current density, OLED performance is significantly limited due to efficiency "roll-off" or "droop," a phenomenon where the external quantum efficiency decreases with increasing current density.[72] The mechanism for efficiency roll-off is unclear. The two most likely mechanisms are exciton-exciton annihilation and exciton-charge annihilation, and the relative importance of these mechanisms is highly controversial.[72] In order to engineer improved OLED devices for lighting and lasing applications, the mechanism of efficiency roll-off must be identified, in order to facilitate rational design of new devices.

Much work has been done to identify the mechanism of OLED roll-off. Experimental studies deduce the mechanism by fitting phenomenological kinetic models to time-resolved photoluminescent data. A number of these studies have been conducted for different devices, coming to contradictory conclusions about the mechanism.[87–92] Theoretical studies typically employ kinetic Monte Carlo (KMC) to model this problem, as it allows for molecular-scale simulations of OLED devices.[93–95] However, despite many KMC studies on OLED roll-off, no clear answer has emerged, as these studies

also come to contradictory conclusions about the most important mechanism.[96–99] These findings, both experimental and theoretical, that different mechanisms seem to dominate in different devices suggests that the relative role of exciton-exciton and exciton-charge annihilation may be device dependent, with no universal mechanism that describes all devices.

If different mechanisms dominate in different devices, researchers will have to identify the roll-off mechanism in a given device before attempting any rational design to improve the device. Experimental determination is difficult as the methods for determining the roll-off mechanism involve complicated experiments, and theoretical approaches have the advantage of allowing the decoupling of the various mechanisms suspected to govern OLED performance. However, KMC models can be quite computationally expensive, and given the multitude of possible variations of OLED and potential modifications to each device, it is infeasible to develop and run a KMC model for every device. A microscopic model that is fast enough to study the large number of different OLEDs and ways they can be modified would be a powerful tool for enabling rational design of high-brightness OLED devices.

1.2.3 The mean field steady-state method

Previous work from the Van Voorhis group[100] developed a mean-field approximation to KMC, called the mean field steady-state (MFSS) approximation, which has been shown to give similar accuracy to kinetic Monte Carlo for disordered systems at a fraction of the computational cost. The MFSS method employs a lattice model, similar to KMC, but instead of solving for the population at each site using explicit interactions with the entire lattice, the mean field approximation is employed, so each site's population is calculated considering only the interaction with the average population of the lattice. However, unlike traditional mean field approaches, this procedure is done self-consistently, as described below and illustrated in Fig. 1.4.

For a given species, say x, we start with an initial guess for the average population of x on the lattice ($\bar{x}$). We then solve for the population of x at each lattice site (x_i for site i) using a mean field description of its nearest neighbors, as shown in the

central panel of Fig. 1.4. Then, we average the resulting populations (shown in the right panel of Fig. 1.4), and compare this average to the initial guess for $\bar{x}$. If the averages agree, we stop the procedure and proceed with the calculated populations. If not, we replace the initial guess average with the new average, and repeat the process, solving for the population on each lattice site. This self-consistent procedure has been shown to be essential in obtaining a good description of disorder in the system, as it allows us to treat each lattice site as a separate site with a different population and energy.[100] This model could be extremely useful for modeling OLED kinetics, given its high accuracy and low computational cost.

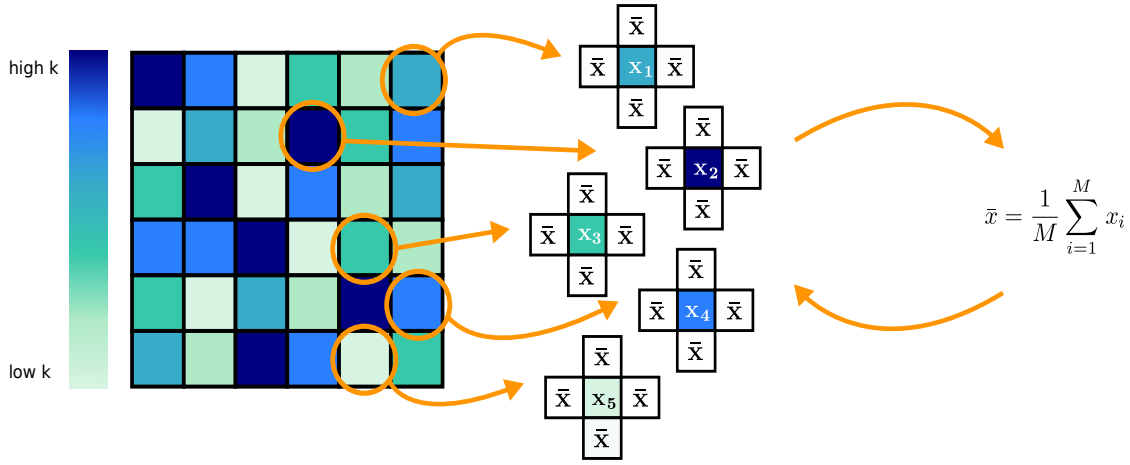

Figure 1.4: Illustration of the self-consistent field procedure. We start with a lattice model (left) where each site has a different rate constant (k), with an initial guess for the average population over the lattice, $\bar{x}$. We then calculate the population of x at each site (x_i), using the guess of $\bar{x}$ (center). Using the populations we calculate at each site, we compute the new average, $\bar{x}$ (right). This process is repeated until $\bar{x}$ does not change.

1.3 Structure of this thesis

Chapter 1 of this thesis was the overall introduction. Chapters 2–4 of this thesis will be devoted to studying the electronic structure of CdSe and CdSe/CdS quantum dots, in both the ground and excited states. Then, in chapter 5, we pivot to studying exciton kinetics in OLEDs.

In chapter 2 we focus on the excited state properties of core-only CdSe quantum dots, investigating the absorption spectrum of several different sizes of CdSe with several different surface passivation schemes. We find that CdSe core-only quantum dots are inherently defective, meaning QDs that would be considered trap-free by conventional definitions (fully passivated with ligands, relaxed surface geometry, clean band gap, and no vacancies, adsorbed atoms, or doping) are still plagued by surface hole traps associated with undercoordinated Se atoms. This is true across several passivation schemes, and the number of hole traps increases with increasing QD size.

In chapter 3, we investigate the effects of annealing, or self-healing, on the excited state spectrum of CdSe core-only QDs. We find that the ligands used have a strong effect on surface reorganization, and that surface reorganization leads to reduction in the number of undercoordinated atoms, reduction in the number of surface trap states, increased delocalization of the core (S- and P-like) states, and increased brightness of the core states in the QD. However, we also find that extensive surface reorganization can lead to new geometric features on the surface, such as clashing Cd-Cd pairs, that create new surface trap states that had not been identified before.

In chapter 4, we study the ground state electronic structure of CdSe/CdS core/shell QDs, paying particular attention to the location of the valence band maximum and conduction band minimum, and the presence of surface trap states. We find that, similar to core-only CdSe, CdSe/CdS QDs are plagued by intrinsic hole traps even after relaxing the surface and passivating all Cd atoms. We also find that the valence band is delocalized over the core and shell of the QD, despite the effective mass approximation and experimental predictions that the VBM should be located in the core. However, we find that both the VBM and CBM are located on half the QD, rather than fully delocalized over the entire core and shell.

In chapter 5, we develop a computationally inexpensive model to describe exciton and charge carrier kinetics in OLED devices. This model agrees very well with experiment, and is able to extract microscopic details such as rates of different processes from a routine device-level experimental measurements. Using this model, we are able to identify the mechanism of roll-off in two different OLED devices, and it has

the potential to be used in many more.

Chapter 2

TDDFT calculations reveal that core-only CdSe quantum dots are inherently defective

The basis for this chapter is published as:

Tamar Goldzak*, Alexandra R. McIsaac*, and Troy Van Voorhis. Colloidal CdSe nanocrystals are inherently defective. *Nature Communications*, 12(1):890, February 2021. *These authors contributed equally to the work.

2.1 Introduction

Colloidal semiconductor nanocrystals (NCs), or quantum dots (QDs), are solution-processed materials that typically consist of hundreds of semiconductor core atoms surrounded by a ligand shell that both passivates the surface and imparts solubility. Semiconductor NCs exhibit discrete optical spectra that are qualitatively different from the bulk due to quantum confinement.[102–104] The NCs' spectrum and optical properties can be tuned by changing the NC size, shape, and composition.[105–107] Due to their tunable spectrum and high luminescence, colloidal NCs have been successfully used in many applications and optoelectronic devices,[2] such as solar cells,[3–6] photodetectors,[7,8] light emitting diodes,[9,10] displays,[11] and biological sensing and

imaging.[12,13]

The low-energy absorption spectra of NCs are typically dominated by a bright peak or peaks[16,104] and the way in which these peaks shift with NC size, as well as the spacing between them, can be qualitatively explained by simple particle-in-a-sphere (PiS), or effective mass, models.[17] For this reason, NCs are sometimes referred to as artificial atoms,[103] despite the fact that, aside from their absorption spectra, NC photophysics is very different from atomic photophysics: the photoluminescence (PL) spectra of NCs often displays a significant Stokes shift;[108] the PL quantum yield (QY) is significantly less than unity;[14] and under constant illumination, single NC PL displays an on-off intermittency known as blinking.[1,26,109,110]

In each of these situations, the unusual photophysics of NCs is intimately tied to the existence of surface defect states that compete with the bulk-like PiS states. For example, blinking is thought to be tied to surface charge defects,[26,111] while PL QY can be improved by using ligands that better passivate the surface.[112] The chemical nature of these defects has been the source of much study and speculation: incomplete ligand passivation,[28] off-stoichiometry NCs,[113] charging,[26,111] vacancy formation,[114,115] and dopants[116] have all been implicated as potential sources of surface defect states. The common assumption is that defects arise from imperfections in the synthesis—if one could only create dopant-free NCs with perfect passivation, these surface states could be removed. Indeed, this picture is supported by the fact that core-shell NCs have dramatically improved PL QY and significantly reduced blinking.[14,36]

It has been shown computationally that unpassivated surface Cd atoms create electron traps and unpassivated surface Se atoms create hole traps in the ground state band structure.[30,31,35,44,45,117] These traps will affect electron transport, although often the surface of a NC will rearrange or undergo self-healing to eliminate mid-gap traps, resulting in a clean band gap.[28,44] Despite many experimental and theoretical works suggesting that surface traps strongly affect the optical properties of NCs, these effects have been largely unexplored from an *ab initio* computational point of view. A few studies have used *ab initio* tools to simulate optical absorption spectra of CdSe

quantum dots[32,57,62] but the connection of the computed spectra to surface states or the processes described above has yet to be addressed.

In this chapter, we present computational evidence that CdSe NCs are inherently defective. That is, we present data suggesting that CdSe nanoparticles possess dark surface excitations that cannot be eliminated by any commonly used ligand for surface passivation and are not associated with any compositional defect. Using time dependent density functional theory (TD-DFT),[48] we simulate several stoichiometric, uncharged, fully passivated, fully relaxed NCs of various sizes and find that despite clean band structures with no mid-gap states, in all cases, most of the low lying excited states are surface associated and optically dark. By examining the size dependence of our results, we conclude that these states become more prevalent as the size of the NC increases. Careful examination of the NC geometry reveals that, despite significant surface rearrangement, there remain several undercoordinated surface Se atoms. Examination of the electron and hole spatial distributions reveals that the majority of the dark states have holes that are strongly localized on these undercoordinated surface Se atoms. This observation explains why these defects are essentially unavoidable in most core-only CdSe NCs—no commonly used NC ligand coordinates with the chalcogenide. Indeed, simulating three different passivation schemes, we find that these defect states are present in every case. Our results have significant implications for the understanding of semiconductor NC photophysics and could have a significant impact on the design of NC-based photcatalytic and photon upconversion systems.

2.2 Results

We created stoichiometric, defect-free CdSe NCs of various sizes following a protocol used previously for PbS[118] and CdSe NCs.[119] Briefly, we use the Wulff construction procedure to create a quantum dot of a given diameter cut from the bulk Wurtzite CdSe structure. We remove any singly-coordinated atoms from the structure, and check to make sure it is roughly spherical and is stoichiometric. We then passivate all of the the surface Cd's with ligands, and fully relax the structure using density

functional theory (DFT). Careful analysis of the resulting atomic structures and band structures (see appendix A) confirms that this process results in NCs that do not have obvious defects such as charging or detached ligands, and have a clean band gap with no mid-gap trap states for electrons or holes.

For a diameter of 2 nm, this procedure results in a $Cd_{91}Se_{91}$ NC, whose TD-PBE0[120] excitation energies with their corresponding oscillator strengths and absorption spectrum are shown in Figure 2.1 (black sticks and solid red line, respectively). More information on calculating the absorption spectrum is presented in the Methods section. The absorption peak around ~ 2.95 eV is in good agreement the experimental peak for NCs of comparable size,[16] once one accounts for the fact that PBE0 slightly overestimates the bandgap of CdSe.[121] To the red of the bright peak, there is a weakly absorptive tail that is typically not observed in experiment. However, due to the fact that these states are quite dim and broad, it would be difficult to differentiate these from background noise in any realistic situation. Thus, it seems likely that, in addition to the bright state, the simulations are revealing a set of states that would simply be overlooked in the experimental absorption spectrum. In addition to the absorption spectrum, which only reveals optically active states, Figure 2.1 displays the density of transitions—that is, the density of excited states at a given energy—as a broadened curve (blue line). Clearly there are many dark states both at low energies—below the lowest bright state—as well as at energies comparable to and even above the first bright state. Absorption spectra of this type have been computed before for $Cd_{33}Se_{33}$ NCs and dark states below the bright state were also observed,[32,57] but the nature of these non-bright states has been largely unexplored.

In order to characterize these states, we have examined the attach and detach densities[122] for the transitions in Figure 2.1. Roughly speaking, the detach density is the density of the excited hole and the attach density is the density of the excited electron. These excited state densities can be broken down into charge contributions from different atoms, in a similar manner to Löwdin charge analysis for the ground state.[123] We can then use the inverse participation ratio (IPR) to estimate the number of atoms that contribute significantly to the electron or hole density:

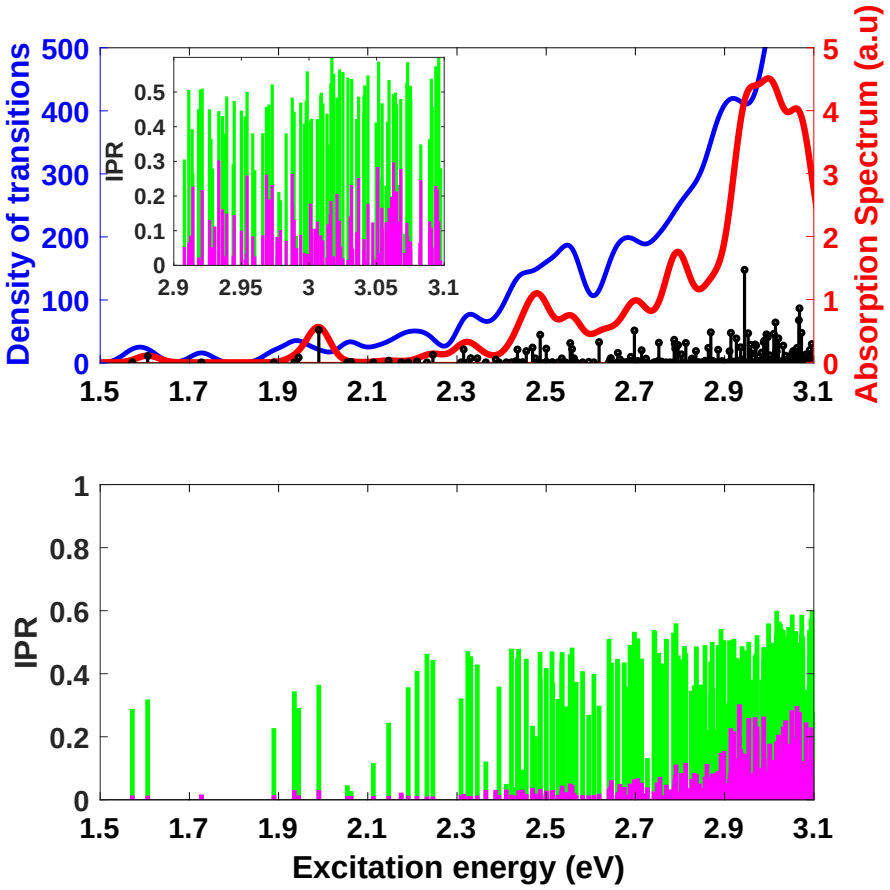

Figure 2.1: Spectrum and IPR for the 2 nm, methylamine-passivated $Cd_{91}Se_{91}$. Top: Absorption spectrum in arbitrary units (red) and density of transitions (blue). Black sticks show individual excited states, whose oscillator strengths have been broadened to create the absorption spectrum. Note the high density of states with little or no oscillator strength (i.e. dark states). Bottom: Inverse participation ratio (IPR) for electrons (green) and holes (magenta) for each excitation. A larger IPR corresponds to a more delocalized wavefunction. Clearly the dark, low energy states are associated with localized states, while the bright states are significantly delocalized. Inset: Enlarged plot of the IPR for the higher-energy part of the excitation spectrum, i.e. $E_{\text{ex}} > 2.9$ eV.

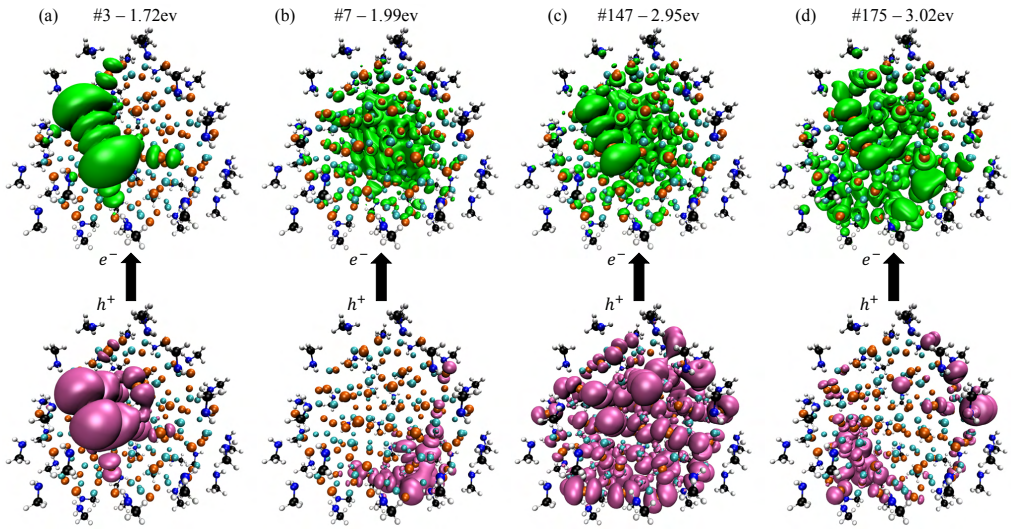

Figure 2.2: Representative attach and detach densities for $Cd_{91}Se_{91}$. Attach(top, green) and detach(bottom, magenta) densities for four representative excited states of the 2 nm diameter methylamine-passivated $Cd_{91}Se_{91}$ NC, showing the locations of the electron and hole, respectively. From left to right, these are the 3^{rd},7^{th}, 147^{th} and 175^{th} excited states of the NC, which correspond to surface-to-surface, surface-to-bulk, bulk-to-bulk and surface-to-bulk. The bright states are delocalized in a similar way to the 147^{th} excitation in the way that would be expected from the particle-in-a-sphere model. The colors of the atoms in the NC are: Cd—cyan, Se—orange, C—black, N—blue, H—white.

$$\mathrm{IPR}^{\mathrm{e}} \equiv \frac{1}{N\sum_A (q_A^{\mathrm{e}})^2} \qquad \mathrm{IPR}^{\mathrm{h}} \equiv \frac{1}{N\sum_A (q_A^{\mathrm{h}})^2} \tag{2.1}$$

where q_A^{e} is the charge from the electron (attach) density associated with atom A, q_A^{h} is the charge from the hole (detach) density associated with atom A, and N is the total number of semiconductor atoms (e.g. 182 for the 2 nm NC). If the electron or hole is delocalized equally over all atoms then the IPR will be equal to 1, since $q_A = \frac{1}{N}$ for all atoms. Meanwhile, if the electron or hole is localized on a single atom, $\mathrm{IPR} = \frac{1}{N}$. Thus, the IPR gives a single number that allows us to distinguish surface (localized, low IPR) from bulk (delocalized, high IPR) states,[35] as well as recognizing when something is between these two limits.

The electron and hole IPRs for the 2 nm NC are shown in the bottom panel of Figure 2.1 (green and magenta, respectively). We directly visualize the electron and hole densities for a number of representative states in Figure 2.2. Qualitatively, these hole-to-electron excitations can be divided into three types of states: surface-to-surface (Figure 2.2a), surface-to-bulk (Figure 2.2b,d), and bulk-to-bulk (Figure 2.2c), such that a surface or bulk state corresponds to a density localized on the surface of the NC or delocalized over the whole NC, respectively. Across the entire energy range of the spectrum, the majority of the states we observe for this 2 nm NC are surface-to-bulk states. Quantitatively, the IPR clearly shows that the hole density is localized for almost all excitations below ∼2.95 eV, and Figure 2.2a–b show that these densities are localized on the surface of the NC. Above 2.95 eV, the IPR shows that some of holes are now quite delocalized, with 25% of the atoms routinely being involved in each excitation. Note that even the delocalized holes are almost entirely confined to the Se atoms, so 25% of the total number of atoms corresponds to 50% of the practically available sites, meaning that these correspond to quite delocalized hole states, as shown in Figure 2.2c. We will use 25% as a cutoff to distinguish between localized and delocalized states. However, even at high energies there are a large number of localized hole states interspersed with the delocalized states, as well as states that are hybrids between localized and delocalized states, which can be seen

in Figure 2.2d. The electron density is localized in a few cases (Figure 2.2a), but is typically very delocalized even for low energy states, and remains delocalized for the vast majority of bright states (Figure 2.2b–d).

Based on this analysis, the low-energy excitations can all be classified as either surface-to-surface or surface-to-bulk. This result is consistent with the orbital density of states (reported in appendix A)—the lowest conduction band orbitals are all localized on the surface for this NC. However, it is important to note that these surface orbitals are not in the gap; rather, they form the edge of the quasi-continuous band of available energies in these NCs. Furthermore, the TDDFT excited electron and hole states are comprised of a linear combination of orbitals, and thus a few surface orbitals lead to a large number of surface hole states. This analysis thus reveals a situation in which the dark states are primarily associated with highly localized hole densities. We observe that, among the dark states, those with higher oscillator strength tend to be surface-to-bulk excitations (cf the small peak at 2 eV, (see Fig. 2.2b)), which is consistent with our physical intuition that the electron and hole wavefunctions must overlap in space to produce significant absorption intensity. Above 2.95 eV, we observe the emergence of bulk-to-bulk states that qualitatively resemble the wavefunctions one would predict based on the particle-in-a-sphere (PiS) model. This observation explains why the PiS model is so successful in explaining the absorption spectra of NCs even when most of the states are not PiS-like: as long as the bright states are PiS-like, changes in the absorption spectrum will be largely captured by ignoring all the non-PiS states. However, as should be clear from the discussion above, while the spectrum is largely controlled by bulk-to-bulk PiS states, the low energy transitions are dominated by surface states. Furthermore, the brightest excited state—the 143^{rd} excited state—is half way between a localized surface state and a delocalized PiS state.

Our NCs are smaller than the smallest CdSe NCs typically used in devices ($\sim$3 nm), so one might question the relevance of our findings to realistic NCs. We have therefore examined the size dependence of our results. For computational reasons, we cannot simulate NCs that are significantly larger than $Cd_{91}Se_{91}$ and so instead

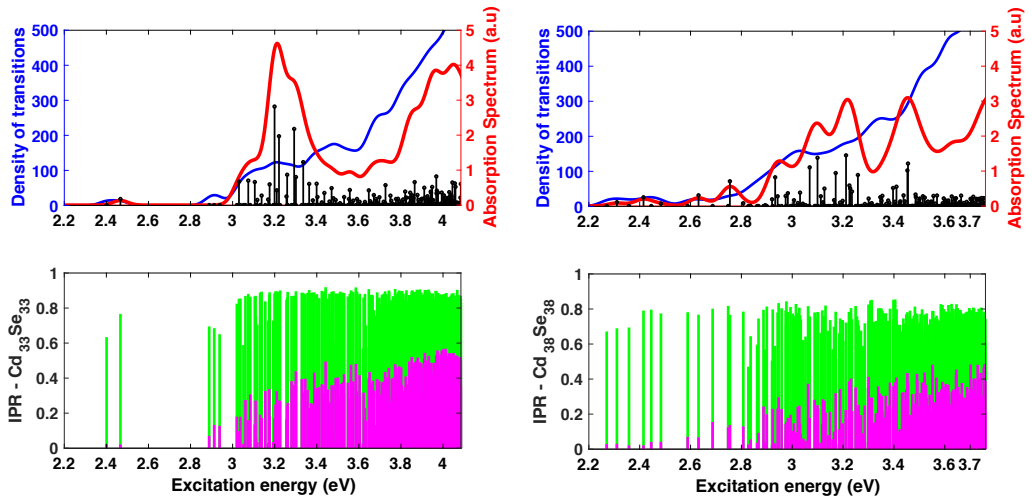

Figure 2.3: Effect of dot size on the spectrum and IPR. Top: Absorption spectrum in arbitrary units (red), density of transitions (blue), and individual excitations (black sticks) for $Cd_{33}Se_{33}$ (left) and $Cd_{38}Se_{38}$ (right) with methylamine ligands. Bottom: Inverse participation ratio (IPR) for $Cd_{33}Se_{33}$ (left) and $Cd_{38}Se_{38}$ (right) with methylamine ligands. In each case, the number of excited states is chosen to be equal to that of the 2 nm NC in Figure 2.2. The number of low energy, surface-associated transitions clearly increases with NC size.

we looked at smaller NCs to explore this trend. Figure 2.3 shows the absorption spectra for $Cd_{33}Se_{33}$ (1.3 nm diameter) and $Cd_{38}Se_{38}$ (1.4 nm diameter) NCs. In order to facilitate comparison with the $Cd_{91}Se_{91}$ NC from Figure 2.1, we chose the same number of excitations (260) in each case, meaning that progressively higher energy states are included for progressively smaller NCs. The first immediate observation is that the number of low energy surface-associated states below the first bright bulk state is clearly increasing with NC radius. For the smallest NC, below the first bright bulk state at ∼3.2 eV there are 21 surface holes (78% of the hole states in this regime) with IPR < 0.25; for the medium-sized NC there are 42 surface hole states (93%) below the first bright bulk excitation at ∼3.1 eV; for the largest NC, there are 142 (99%) surface hole states below the bright excitation at ∼2.95 eV, as well as a number of surface electron states that were not present in the smaller NCs. This trend also extends to the higher energy part of the spectrum; 16% of the excitations above the first bright excitation have holes on the surface in the smallest NC, 33% have holes

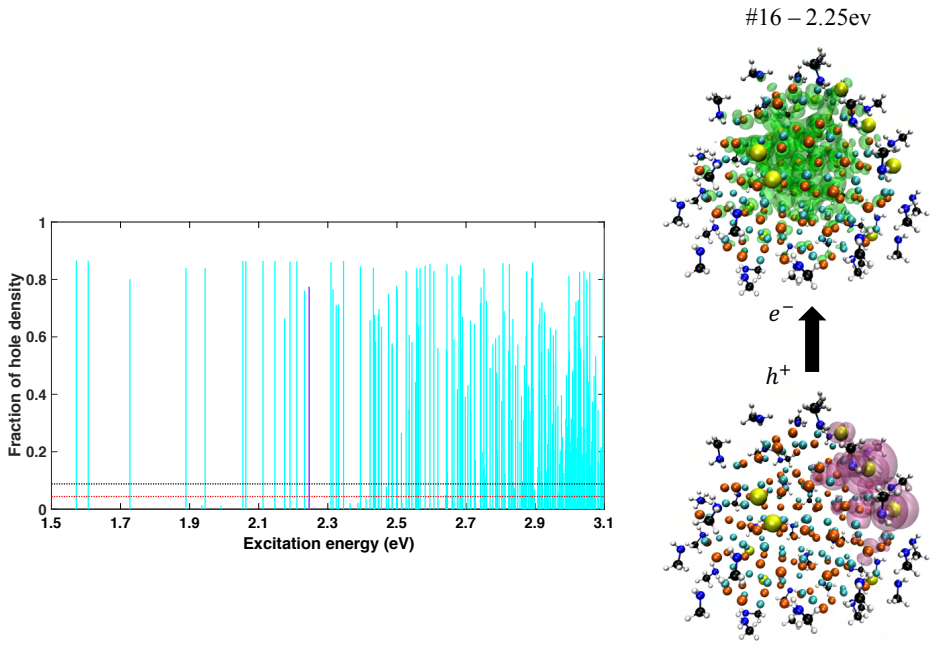

Figure 2.4: Effect of undercoordinated Se atoms on the excited states of $Cd_{91}Se_{91}$. Left: Fraction of hole charge density on the eight Se atoms that are two-coordinate in the $Cd_{91}Se_{91}$ NC with methylamine ligands. The red and black dotted lines illustrate the expected fraction based on the assumptions that the hole is distributed equally among all Se or all Cd and Se atoms, respectively. Clearly, most of the low energy states preferentially localize on the two-coordinate Se atoms. Right: Attach (green) and detach (magenta) densities of the 16^{th} excited state (marked with a magenta line in the left hand figure). The undercoordinated Se atoms are highlighted in yellow. Clearly the hole is specifically localized near a subset of these atoms.

on the surface for the medium sized NC, and 92% for the larger NC. This observation suggests that for compositionally perfect NCs in the experimental size range, localized surface-like states are likely to be even more prevalent than our results here would suggest.

We have been careful to create the most perfect core-only NC that could be experimentally realized—stoichiometric, uncharged, and fully passivated with Lewis base ligands—yet we still see surface states. In order to understand this fact, we analyzed the bonding pattern in our NCs. The one obvious defect in any NC is that some of the atoms at the surface will be undercoordinated; Cd and Se atoms will

all be four-coordinate in the bulk, but at the surface this necessarily cannot be the case. In particular, surface atoms with less than three neighbors have been shown to routinely create traps in the ground state band structure of NCs.[30,31,35,44,45,117] Our strategy of passivating all surface Cd atoms and relaxing the geometry (which has been shown to eliminate undercoordinated Se atoms) is aimed at eliminating these band structure defects. In agreement with previous findings,[32,35,124] we can confirm that this approach results in a band structure free of mid-gap states (see appendix A). However, for every NC we have studied there are two-coordinate Se atoms at the surface. They do not dominate the ground state band structure, but they do dominate the excited states. In Figure 2.4, we plot the fraction of the Löwdin charge on the two-coordinate Se atoms for all of the hole densities in the $Cd_{91}Se_{91}$ spectrum. We find that the low-energy surface states tend to have hole densities that are strongly localized on the undercoordinated Se atoms. This is illustrated qualitatively in the right panel of Figure 2.4, which shows the electron and hole densities for the 16th excitation; the hole density is clearly localized on the undercoordinated Se atoms, which are highlighted in yellow. Clearly, the majority of the low energy states in these NCs can be attributed to the presence of these two-coordinate Se atoms. Interestingly, we also find that there are some electron densities that localize on these undercoordinated Se atoms (reported in appendix A), and so they can also serve as electron traps (see Fig. 2.2a). But this effect is less dominant than the localization of the hole densities on the undercoordinated Se.

Now, given that no commonly used solubilizing ligand passivates the chalcogenide atoms in NCs, one would therefore assume that no ligand would be effective at removing these low-energy states. That is, one would assume that these dark states are not a feature of methylamine ligands in particular, but rather would be present for CdSe NCs with any organic passivating ligand on the Cd atoms. To test this, we repeated our simulations for NCs passivated with trimethyl phosphine oxide (Me_3PO), intended to mimic the commonly-used TOPO ligand, as well as completely unpassivated NCs. For computational expediency, we used the medium-sized $Cd_{38}Se_{38}$ NCs for this comparison, and the results are shown in Figure 2.5. Clearly both the Me_3PO-passivated

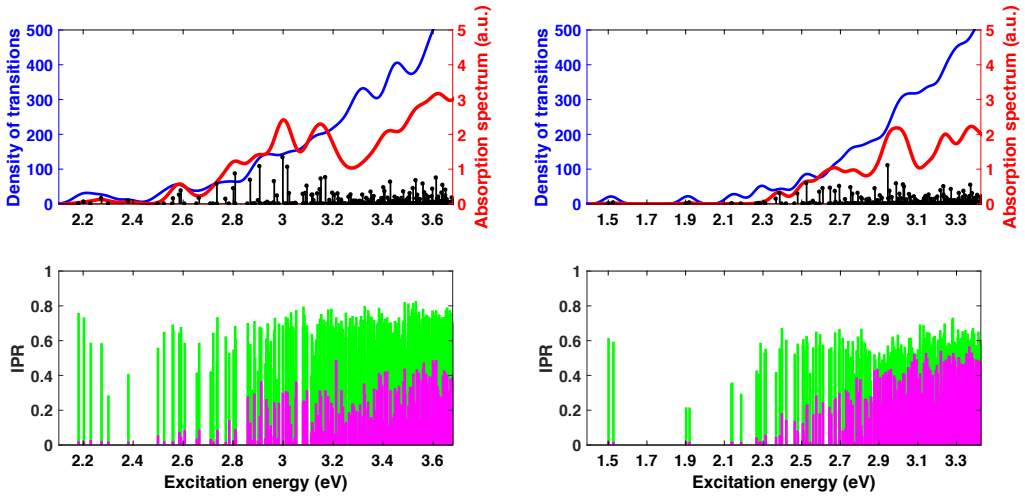

Figure 2.5: Effect of ligands on the spectrum and IPR. Top: Absorption spectrum in arbitrary units (red), density of transitions (blue), and individual excitations (black sticks) for $Cd_{38}Se_{38}$ with Me_3PO ligands (left) and $Cd_{38}Se_{38}$ with no ligands (right). Bottom: Inverse participation ratio (IPR) for $Cd_{38}Se_{38}$ with Me_3PO ligands (left) and $Cd_{38}Se_{38}$ with no ligands (right). In each case, the number of excited states is chosen to be equal to that of the 2 nm NC in Figure 2.2. The number of low energy, surface-associated transitions is similar to that of the $MeNH_2$ case shown in Fig. 2.3

NC and the bare NC qualitatively resemble the amine-passivated counterpart in Figure 2.3—there are a large number of dark transitions below the bright transition (39 surface holes for Me_3PO and 53 for the bare NC). Indeed, it is clear that methylamine is actually the best ligand (amongst those we have studied) for suppressing these dark states. This observation is consistent with the experimental observation that amine-passivated NCs have among the highest quantum yields for stoichiometric core-only structures.[61,125] Further, by looking at the IPRs of the electron and hole densities, we find that, as before, the dark states are all surface-associated in some fashion. We thus conclude that, for all practical purposes, stoichiometric core-only CdSe NCs are intrinsically defective—there is no Lewis base ligand that removes the surface states even when the passivation is complete.

2.3 Discussion

The existence of a dense manifold of dark states has the potential to dramatically change our understanding of processes like multiple exciton generation[3] (where the presumed lack of intermediate states is assumed to stabilize the biexciton state) and blinking[1,26,110] (where the dark state is typically assumed to be a single state rather than a quasi-continuum). At the same time, the fact that these states exist at the surface will have an outsized influence on photochemistry initiated by the NCs[126,127] as well as processes like upconversion,[24] energy transfer,[109] and electron transfer,[128,129] where proximity to the surface drives function.

The presence of such a large number of dark surface states is also consistent with a number of experimental observations. First, there is the relatively large (up to 0.1 eV) nonresonant Stokes shift observed in most as-synthesized pristine CdSe NCs that appears on the picosecond timescale.[130,131] It has been clearly argued that the energy difference between the absorbing and emitting states is due to the exciton fine structure.[17,130,132] However, in order to facilitate an ultrafast 0.1 eV relaxation in the absence of large atomic distortions, one would typically expect there to be various intermediate (I) electronic states between the absorbing (A) and emitting (E) states, so that the relaxation involves a series of small steps ($A \rightarrow I_1 \rightarrow I_2 \rightarrow ... \rightarrow E$), rather than a single large one. Such a series of states is not easily accommodated in the PiS or artificial atom picture of NCs, in which only a handful of well-separated electronic states exist and the states get further apart as one approaches the lowest excitation. However, in a picture of NCs that contains both bright bulk-to-bulk states and dark surface-associated states, the ubiquitous Stokes shift of colloidal nanocrystals is easily explained. There are many surface states of varying brightness below the strongly absorbing bulk-to-bulk transitions. These states can play the role of the intermediate states in the mechanism above. Thus, our findings provide an easy explanation for the observed Stokes shift dynamics.

Another important role of dark states is in explaining the relatively low quantum yield (QY) and blinking behavior of CdSe NCs. Again, in the PiS or artificial atom

models, these effects are hard to explain, as the lowest state is typically bright or at the very least well separated from any dark states it might transition to. Our findings suggest the spectrum of low-lying states in colloidal CdSe NCs is much more complex than the simple PiS model predicts—with even the most perfect NCs having a fairly dense manifold of low-lying states with very long emission lifetimes. Those long lifetimes give a larger window for non-radiative processes to interfere with emission. Relaxation to the ground state would reduce the QY, while photoreduction could turn the emission off. Thus the presence of dark surface states also provides a facile explanation of blinking and QY in CdSe NCs.

Among core-only NC structures, it has been shown experimentally that NCs with a Cd-rich surface provide the highest QY for CdS[113] and CdTe[37] NCs—probably because the additional Cd atoms passivate some 2-coordinate chalcogenide atoms.[35,124] Indeed, those results lead to a somewhat different picture of a perfect NC—one in which the entire surface is passivated with CdX_2 (X=Cl,I) ligands[35,124] in what amounts to a CdSe/CdX_2 core-shell structure. This is also consistent with our result that there are many dark surface states in what is traditionally considered a perfect quantum dot, which are caused by underpassivated Se atoms.

The presence of a large number of dark surface states is consistent with previous theoretical calculations on CdSe. Previous ground state studies had noted that, despite a clean-looking band gap, the HOMO was localized on the NC surface,[44] while for less perfect dots, it has been noted that the leading cause of mid-gap traps is the presence of two-coordinate Se atoms.[35,113] We will emphasize that in these studies, defects were intentionally introduced in such a way as to create deep traps in the band gap. In our case, surface defects have been avoided insofar as geometrically possible (to make a "perfect" NC) and the resulting band structure does not show the same trap states. Thus, while our NCs do have surface defects in the form of two-coordinate Se atoms, in the language of previous studies they are defect-free. That is, in agreement with previous studies, we find that trap states can be eliminated from the band structure of CdSe NCs. Looking at the small number of computational studies of the excited states of these NCs, TDDFT studies of $Cd_{33}Se_{33}$ with methylamine ligands

had also found a long tail in the absorption spectrum,[32,57] and studies using TDLDA for NCs with no ligands found an extremely broad and long tail,[62] though these works did not explore the nature of these states. Further, when one uses formate anions to passivate Cd and H^+ to passivate Se, the TDDFT spectrum becomes much cleaner than when methylamine alone is used.[57] While this geometry is likely not stable in practice, the reduction in dark states that comes from artificially passivating the Se sites is consistent with our observation that undercoordianted Se atoms contribute heavily to the optically dark states in these NCs.

Finally, our finding that the number of low-lying surface states increases with NC size runs counter to the experimental result, where smaller NCs are typically more defective than larger NCs.[115] This difference is easily understood when one remembers that our simulations are always dealing with perfect NCs—fully passivated, stoichiometric and non-defective structures. It is fairly well accepted that below a certain size, it is difficult to control the number of defects in CdSe NCs.[133] Thus, as the NCs get smaller, our simulated systems become less and less similar to the experimental system. These differences explain the divergence between the two results. Fortunately, we can extrapolate our results to the size range (3–20 nm) in which the experimental NCs are thought to be most nearly perfect. Doing this, we find that surface states are even more prevalent for those large NCs than the results here would suggest.

Taken together, our results suggest that the PiS/artificial atom model of colloidal NCs is incomplete. A qualitatively correct picture will need to accommodate both the bright bulk-to-bulk PiS-like states as well as a dense manifold of surface-associated states. At present there are no simple models that can accomplish this, although recent results using random matrix theory[134] are potentially one good first step.

In conclusion, we present computational evidence that even perfectly passivated CdSe NCs possess inherent surface defects. By simulating a large ($Cd_{91}Se_{91}$) NC fully passivated with amine ligands using hybrid TDDFT, we find that the overwhelming majority of the low-lying states are associated with the surface—the brightest transition is the 143$^{\text{rd}}$ excited state of the NC. By comparing to the results for smaller

($Cd_{33}Se_{33}$ and $Cd_{38}Se_{38}$) NCs we observe that, as long as all the NCs are similarly passivated, the number of low-lying surface states tends to increase with the size of the NC. Careful correlation with the chemical structure reveals that the majority of these defects are associated with hole densities localized on a handful of two-coordinate Se atoms. As no common ligand passivates the surface Se atoms, we conclude that the majority of these defects are therefore inherent to core-only CdSe NCs. We test this by performing calculations for phosphine oxide passivated NCs and bare NCs, and confirm qualitatively similar results in each case.

The implications of these results are wide-ranging. The surface availability of electrons and holes in photoexcited CdSe NCs is likely to be much higher than previously anticipated, as even a NC that ultimately emits from a bulk-like state has likely passed through numerous surface localized states to get there. The stability and coherence of bi- and tri-exciton states are likely to be much lower than expected as they couple to a much denser manifold of excitations. The quantum yield of core-only CdSe NCs is likely intrinsically limited by these optical traps. Future work aimed at elaborating and quantifying these effects will be highly influential.

Leading up to that aim, there are several aspects of the present study that can be expanded upon. First and foremost, though the $Cd_{91}Se_{91}$ NC is quite large by simulation standards, it still falls short of the experimentally-relevant size range. Thus, simulations on somewhat larger NCs would help shed more light on the way that these effects reveal themselves in real NCs. Second, here we have only explored equilibrium structures in an attempt to characterize the behavior for completely relaxed NCs. It would be interesting to examine the impact that structural distortions—including simple thermal fluctuations—have on the electronic states.

Finally, we have only looked at a handful of passivation schemes in this work and it would be instructive to explore others. In particular, it has been shown that core-shell CdSe quantum dots exhibit greatly enhanced QY and suppressed blinking, which has been attributed to the shell's ability to passivate both Cd and Se atoms.[14] Here we have shown that underpassivated Se atoms are responsible for the majority of the hole traps in the $Cd_{91}Se_{91}$ dot, but it would be interesting to explore whether

this is also true for other sizes and ligands. It would also be extremely valuable to perform analogous simulations for CdS/CdSe and ZnS/CdSe NCs to see what defects, if any, persist in pristine core-shell NCs. Another obvious extension would involve exploring other semiconducting NCs to see how universal this phenomenon is. Recent calculations on PbS, for example, suggest that low-lying surface states may be present in those NCs as well,[24,124] whereas it has been known for many years that hydrogen terminated Si NCs are defect free.[135] Similar calculations on CdS, GaAs, InAs and other compositions could help elucidate which properties of the material tend to lead to inherent defects. Does faceting help or hinder surface passivation? Are binary seminconductors inherently more defective? Is it simply necessary to passivate every single surface atom to remove defects?

These types of chemical and physical questions will then guide the design of simple models that are capable of incorporating the effects of surface states on the photophysics of semiconductor NCs. Such models will play a key role in understanding and designing new devices based on these fascinating materials.

2.4 Methods

2.4.1 Creating the NC structures

All NC starting structures, except for the $Cd_{33}Se_{33}$ NC, were carved from bulk CdSe with the wurtzite structure. The $Cd_{38}Se_{38}$ NC has a diameter of about 1.4 nm and the $Cd_{91}Se_{91}$ NC has a diameter of about 2 nm. For the passivated NCs, we passivate every surface cadmium with ligands, in accordance with other simulations and experimental results.[28] The $Cd_{33}Se_{33}$ NC starting structure was obtained from the supplementary information of Ref.[28], but ligands were replaced due to optimization convergence issues.

2.4.2 DFT methodology

All calculations are performed using the QChem software package.[136]

Geometry optimizations

Geometry optimizations were performed at both the PBE[137]/LANL2DZ[138–141] and PBE0[120]/LANL2DZ levels of theory. All NCs were optimized until converged by the default QChem geometry optimization thresholds.

TDDFT

All TDDFT calculations were performed with the PBE0 functional and the LANL2DZ basis set and effective core potential. PBE0 was chosen as it is a hybrid functional that incorporates exact exchange, which is important for effective treatment of the electron-hole interaction. Validation studies were conducted to ensure that this level of theory performed well for this problem (see appendix A). For the $Cd_{91}Se_{91}$ NC, some calculations used a reduced single excitation space (see appendix A) to overcome a memory limitation.

2.4.3 Density of Transitions and Absorption Spectra

To calculate the density of transitions, we apply Gaussian broadening to the calculated excitation energies (E_{ex}), and sum the Gaussian distributions:

$$\text{DOT} = \sum_{\text{ex}} \frac{1}{\sqrt{2\pi\sigma^2}} \exp\left(-\frac{(E - E_{\text{ex}})^2}{2\sigma^2}\right) \tag{2.2}$$

To calculate the absorption spectrum, we do the same, but weight the transitions by their oscillator strength (ω):

$$\text{Spectrum} = \sum_{\text{ex}} \frac{\omega}{\sqrt{2\pi\sigma^2}} \exp\left(-\frac{(E - E_{\text{ex}})^2}{2\sigma^2}\right) \tag{2.3}$$

For both calculations, we choose σ to be 35 meV, on the order of the experimental broadening.[28] For the associated stick spectra, the oscillator strengths have been multiplied by 15 so as to be visible on the same axes as the absorption spectra.

2.4.4 IPR

To calculate the IPR, we first conduct a Löwdin charge analysis on the attach and detach densities for all excited states, as implemented in QChem.[123] For each excitation, analysis of the attach density gives atomic charges related to the excited electron (q_A^{e} for atom A), and analysis of the detach density gives atomic charges related to the excited hole (q_A^{h} for atom A). For TDDFT, the sum of these charges is not guaranteed to equal 1, so we then normalize these charges:

$$q_{A,\mathrm{norm}}^{\mathrm{e}} = \frac{q_A^{\mathrm{e}}}{\sum_A q_A^{\mathrm{e}}} \qquad q_{A,\mathrm{norm}}^{\mathrm{h}} = \frac{q_A^{\mathrm{h}}}{\sum_A q_A^{\mathrm{h}}} \tag{2.4}$$

To calculate the IPR for the excited electron and hole for a given excitation, we then insert the normalized charges into the IPR equations:

$$\mathrm{IPR}^{\mathrm{e}} \equiv \frac{1}{N \sum_A (q_{A,\mathrm{norm}}^{\mathrm{e}})^2} \qquad \mathrm{IPR}^{\mathrm{h}} \equiv \frac{1}{N \sum_A (q_{A,\mathrm{norm}}^{\mathrm{h}})^2} \tag{2.5}$$

Chapter 3

The Effect of Self-Healing of Surface Defects on the Excited States of CdSe Nanocrystals

3.1 Introduction

It has long been known that undercoordinated surface atoms can create trap states in the ground state density of states for core-only CdSe quantum dots (QDs) or nanocrystals (NCs).[30,31,35,45,117] Many works have shown that these undercoordinated atoms lead to deep, mid-gap traps. There have been several works looking at the effect of annealing or "self-healing" in quantum dots, showing that surface reorganization leads the band gap of CdSe QDs to open, and eliminates some or all undercoordinated surface atoms and associated mid-gap traps.[44,45,54,142,143] It has been suggested that the mechanism for band-gap opening is primarily related to surface reorganization rather than passivation or elimination of undercoordinated atoms, because band gap opening occurs even in unpassivated structures and when the relaxed structure still has undercoordinated atoms that cause shallow traps at the valence band edge.[44] However, it has been shown experimentally,[51] and theoretically by us in chapter 2, that these shallow, valence band edge traps that are nearly invisible in the band

structure can be equally as problematic as mid-gap states for the optical spectrum. Given that surface reorganization and a clean band gap does not guarantee a trap-free spectrum, this raises the question, what is the effect of surface reorganization on the optical spectrum?

In this chapter, we use electronic structure simulations to study the self-healing process by which nanocrystals anneal away high-energy defects, with a particular focus on the effect on the excited state spectrum. We study this process in $Cd_{38}Se_{38}$ with several different passivation schemes. For all systems we find that, as the surface undergoes relaxation, the number of undercoordinated atoms reduces but does not go to zero. We find that reorganization causes the excited states to become significantly more delocalized, even in the presence of undercoordinated atoms. We also find that reorganization can introduce new defects, which prevent delocalization of the excited states. We find that $MeNH_2$ does the best job of removing surface states; we believe this is due to a compromise between allowing surface relaxation to occur, but preventing excessive relaxation that introduces new defects. Interestingly, for a given system, many of the structures with significantly different numbers of undercoordinated atoms and spectral properties are thermally accessible to one another. This suggests that in experimental conditions even a "perfect" quantum dot would have thermally accessible defects, but that, given the difference in energy and shape of the low-energy spectrum, the appearance of these defects would likely wash out in the ensemble spectrum.

3.2 Computational Methods

3.2.1 Geometry Optimization

All geometry optimizations were performed at the PBE0[120,137]/LANL-2DZ[138–141] and PBE[137]/LANL-2DZ levels of theory as described in chapter 2. Briefly, the starting geometries were cut from the bulk Wurtzite CdSe material, removing all singly coordinated atoms, and attaching ligands to all surface Cd atoms for systems with

ligands.

3.2.2 Structural analysis

For each structure, at several points along the optimization trajectory, we plot the cumulative distribution of bond lengths, and evaluate the number of undercoordinated atoms. We define an undercoordinated atom as any atom with less than 3 opposite-type nearest neighbor atoms. For Cd, this would include Se and ligand atoms, while for Se, this would include Cd only. We define a nearest neighbor as having a bond length of less than 3.1 Å.

3.2.3 TDDFT

All TDDFT calculations were performed at the PBE0/LANL-2DZ level of theory. Validation of this functional and basis set were conducted in appendix A.

The density of transitions (DOT) and spectrum are calculated from the TDDFT excitation energies by applying Gaussian broadening, with σ=35 meV:

$$\mathrm{DOT} = \sum_i \frac{1}{\sqrt{2\pi\sigma^2}} \exp\left(-\frac{(E-E_i)^2}{2\sigma^2}\right) \tag{3.1}$$

$$\mathrm{Spectrum} = \sum_i \frac{\omega_i}{\sqrt{2\pi\sigma^2}} \exp\left(-\frac{(E-E_i)^2}{2\sigma^2}\right) \tag{3.2}$$

Where E_i is the TDDFT excitation energy for excitation i, and ω_i is the oscillator strength.

We also calculate the ground state band structure from the orbital energies (E_{orb}):

$$\mathrm{DOS} = \sum_i \frac{1}{\sqrt{2\pi\sigma^2}} \exp\left(-\frac{(E-E_{\mathrm{orb}})^2}{2\sigma^2}\right) \tag{3.3}$$

With a broadening parameter of σ =150 meV.

3.2.4 Inverse Participation Ratio and Excited State Analysis

To connect the excitations to particular atomic features, we conduct a Löwdin charge analysis on the TDDFT excited states to obtain a set of charges on each atom for the electron and hole. For TDDFT, it is not guaranteed that these charges add to exactly 1, so we normalize them.

To measure the localization of the excitations, we calculate the inverse participation ratio (IPR) for each excitation:

$$\mathrm{IPR}^{\mathrm{e}} = \frac{1}{N\sum_A (q_A^{\mathrm{e}})^2} \qquad \mathrm{IPR}^{\mathrm{h}} = \frac{1}{N\sum_A (q_A^{\mathrm{h}})^2} \tag{3.4}$$

Where N is the number of atoms, q_A^{e} is the normalized excited state Löwdin charge for the electron on atom A, and q_A^{h} is the normalized excited state Löwdin charge for the hole on atom A. The IPR is defined such that, for a completely delocalized excitation, $q = \frac{1}{N}$ for all atoms, and the IPR = 1. However, for an excitation fully localized on one atom, $q = 1$ for that atom and 0 for all others, and the IPR will be equal to $\frac{1}{N}$. Thus, the IPR gives us one number for each excited electron and hole that can be used to distinguish localized (surface) states from delocalized (bulk) states. We define a localized (surface) state as any hole state with an IPR below 0.25, or any electron state with an IPR below 0.5. We use a different metric for electrons and holes because even for the delocalized hole states that we see, the density is almost exclusively confined to the Se atoms, whereas for the electron the density is delocalized onto both Cd and Se atoms. Therefore, this IPR cutoff identifies states that are delocalized over 50% of available atoms.

We also use these charges to calculate the fraction of the total charge for each excited hole and electron that is associated with undercoordinated Se (or Cd) atoms:

$$\sum_j q_j^{\mathrm{e}} \qquad \sum_j q_j^{\mathrm{h}} \tag{3.5}$$

Where j is the undercoordinated Se (or Cd) atoms. This allows us to examine the connection between the excited states and these undercoordinated atoms.

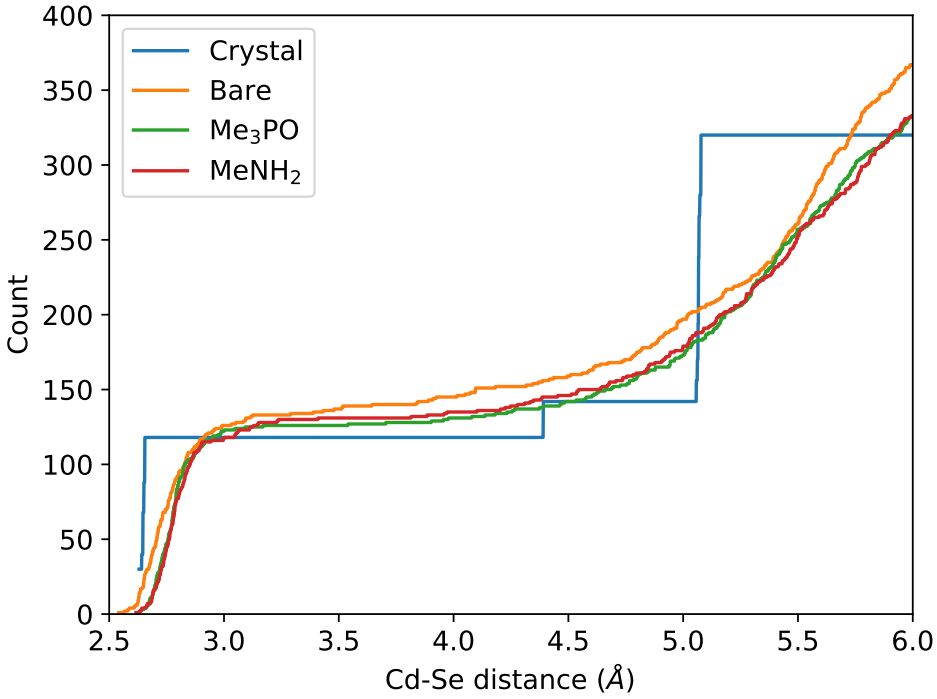

Figure 3.1: Cumulative distribution of bond lengths in $Cd_{38}Se_{38}$ for the unoptimized crystal (blue), the optimized QD with no ligands (orange), the optimized QD with Me_3PO ligands (green), and the optimized QD with $MeNH_2$ ligands (red).

3.3 Results and Discussion

3.3.1 Surface reorganization and self-healing

Over the course of the geometry optimization, the surface of the QD undergoes significant reorganization, often termed "self-healing." Fig. 3.1 shows the cumulative distribution of bond lengths for each system, compared to the crystal structure. In the optimized systems, there are significantly more bonds at each bond distance between 2.9 and 5 Å, which is evidence of this reorganization. One effect of this surface reorganization is a reduction in the number of undercoordinated surface atoms, which we see in every system, in agreement with previous reports on self healing.[44] However, in no system do we see a complete elimination of undercoordinated atoms. This is consistent with previous reports on self-healing in CdSe using DFT within the local

density approximation (LDA) or molecular dynamics.[44,45,142]

One interesting feature visible in Fig. 3.1 is the effect of different ligands on surface reorganization. The QD with no ligands undergoes the most drastic reorganization, followed by the $MeNH_2$, and the Me_3PO undergoes the least amount of reorganization. The finding that reorganization depends on ligand presence is consistent with previous reports using LDA on surface slabs.[144] We also observe the same trend when looking at the reduction in undercoordinated atoms; the QD with no ligands is reduced from 10 Cd and 10 Se in the crystal to 2 Cd and 3 Se in the optimized structure, the QD with $MeNH_2$ is reduced from 10 Se in the crystal to 4 in the optimized structure, and the QD with Me_3PO is only reduced from 10 Se in the crystal to 8 in the optimized structure. This is likely due to the steric bulk of these ligands. In the absence of ligands, the surface is able to relax completely unencumbered. A small ligand like $MeNH_2$ prevents reorganization to some degree, by placing constraints on the Cd atoms as well as creating steric pressure, but still is able to undergo a drastic reduction in the number of undercoordinated atoms. Meanwhile with the very bulky Me_3PO ligand, very little reorganization can take place.

While surface reorganization reduces the number of undercoordinated atoms in all systems, it can also introduce new defects. We have shown that the quantum dot with no ligands undergoes the most drastic surface reorganization, eliminating the largest number of undercoordinated atoms and having the largest distribution of bond lengths between 3 and 5 Å. However, in addition to reducing the number of undercoordinated atoms, this reorganization actually caused new defects to form, introducing a pair of Cd's that are very close together ($\sim$2.8 Å apart), and a pair of Se's that are very close together ($\sim$ 2.5 Å apart). We will refer to these features as clashing pairs. This suggests that having a large amount of surface reorganization may not necessarily be beneficial. Instead, defect management may be a balancing act—there must be some reorganization to remove undercoordinated atoms, but not so much that new defects are introduced.

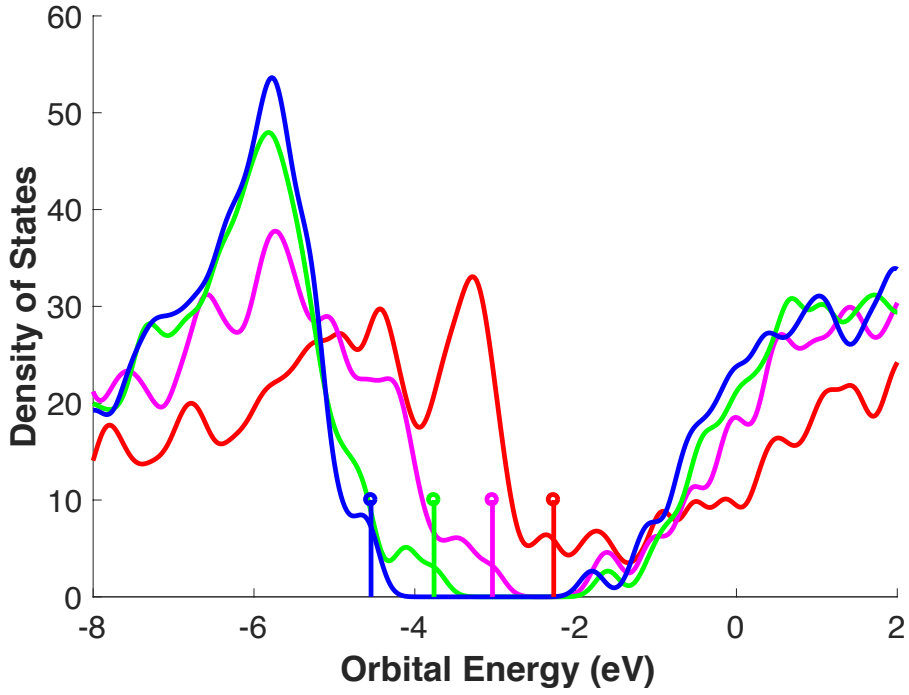

Figure 3.2: Band structure of $Cd_{38}Se_{38}$ with $MeNH_2$ ligands, at several points during the optimization. The red line is the band structure of the crystal structure before optimization, the pink line is early in the optimization (31 meV per atom from the optimized structure), the green line is mid-way through the optimization (5 meV per atom from the optimized structure), and the blue line is the optimized structure. The stems indicate the HOMO energy level for each structure.

3.3.2 Opening of the band gap

Fig. 3.2 shows the band structure of the $Cd_{38}Se_{38}$ dot with $MeNH_2$ ligands at several points in the optimization, including the crystal structure (375 meV per atom away from the optimized structure), a point early in the optimization (31 meV per atom from the optimized structure), a point midway through the optimization (5 meV per atom from the optimized structure), and the final optimized structure. We observe the same trend as has been previously reported,[44] that despite the continued presence of undercoordinated surface Se atoms, the band gap still opens due to surface reorganization. Interestingly, despite these undercoordinated Se atoms, none

of the structures show a true mid-gap state separated from either the conduction or valence bands. However, they all have a tail on the valence band, made up of orbitals localized on these atoms. The band structures for all other systems show the same trend, and are reported in appendix B. The one exception to this is the $Cd_{38}Se_{38}$ dot with no ligands, whose HOMO and HOMO-1 create a mid-gap state above the valence band, even in the optimized structure. The projected density of states for this system (reported in appendix B) reveals that the HOMO is localized on undercoordinated Se atoms, and the HOMO-1 is localized on the clashing Cd-Cd pair. It also reveals an unoccupied trap caused by the clashing Se-Se pair, although it is within the conduction band, and not a mid-gap state.

3.3.3 Evolution of the absorption spectrum

We see similar effects of surface reorganization on the absorption spectrum, shown in Fig. 3.3–3.5 for $Cd_{38}Se_{38}$ with $MeNH_2$ ligands, as well as in appendix B for the other systems. Fig. 3.3 shows the first structure that has an appreciable band gap, which is about 31 meV per atom away from the optimized structure. The top panel of Fig. 3.3 shows the TDDFT spectrum and density of transitions. The first excitations in this spectrum are low in energy, around 1 eV, which is not surprising given the small band gap. It is clear that all of the excitations are relatively dark (in comparison to the optimized structure in Fig. 3.5). While the three-peak shape of the optimized structure's spectrum can be seen in the high-energy part of this spectrum around 2.4–2.8 eV, these peaks are much lower in energy, not very bright, and are not distinguishable from the other, lower energy peaks. The middle panel of Fig. 3.3 shows the IPR for the excited electron and hole. For every excitation, both the electron and hole have very low IPR, meaning that they are very localized. In fact, only one excited hole state and two excited electron states qualify as "bulk" based on the IPR (0.25 for the hole and 0.5 for the electron), which represents 0.5% and 1% of hole and electron states, respectively. The bottom panel of Fig. 3.3 shows the fraction of the excited hole density on the undercoordinated Se atoms. Clearly, for almost every excitation, there is a disproportionate amount of density on these

atoms.

Fig. 3.4 shows the TDDFT results for a structure mid-way through the optimization, about 5 meV per atom from the optimized structure. The top panel of Fig. 3.4 shows the TDDFT absorption spectrum and density of transitions, and we can see that the excitation energies and the shape of the spectrum have begun to strongly resemble that of the optimized structure. The primary difference here is in the low-energy part of the spectrum; the first excitation is around 1.8 eV, whereas for the optimized structure, it is around 2.2 eV. This structure has a lower band gap than the optimized structure, and there are a higher number of undercoordinated Se atoms in this structure, explaining the large number of low energy excitations. The high-energy part of the spectrum is quite similar to that of the optimized structure, with 3 bright peaks between 3 and 3.6 eV. The middle panel of Fig. 3.4 shows the IPR for the excited electrons and holes. Visually, both the electrons and holes have much higher IPR's than those of the less optimized structure, indicating that they are far more delocalized. However, it is clear that there are still many localized hole states. Indeed, for this structure, about 91% of the electron states are classified as "bulk," whereas only 13% of holes are. 13% is much higher than the 0.5% for the less optimized structure, but the percentage of bulk holes is substantially lower than the percentage of bulk electrons. The bottom panel of Fig. 3.4 shows the fraction of hole density on the undercoordinated Se atoms. We can see that there are, in general, fewer excitations with a disproportionate amount of charge on these atoms, which corresponds with the increased delocalization of the hole densities. However, for surface excitations with low hole IPR, there is still a disproportionate amount of charge on the undercoordinated Se atoms, indicating that these atoms are responsible for the trap states.

Fig. 3.5 shows the results for the optimized structure. At this point, the expected spectrum has emerged—there are 3 bright peaks caused by bulk excitations, as would be expected from experiment and effective mass theory,[16] and they appear at an energy that is in reasonable agreement with experiment.[133] There are still a number of low-energy trap states, likely due to the fact that there are still 4 undercoordinated

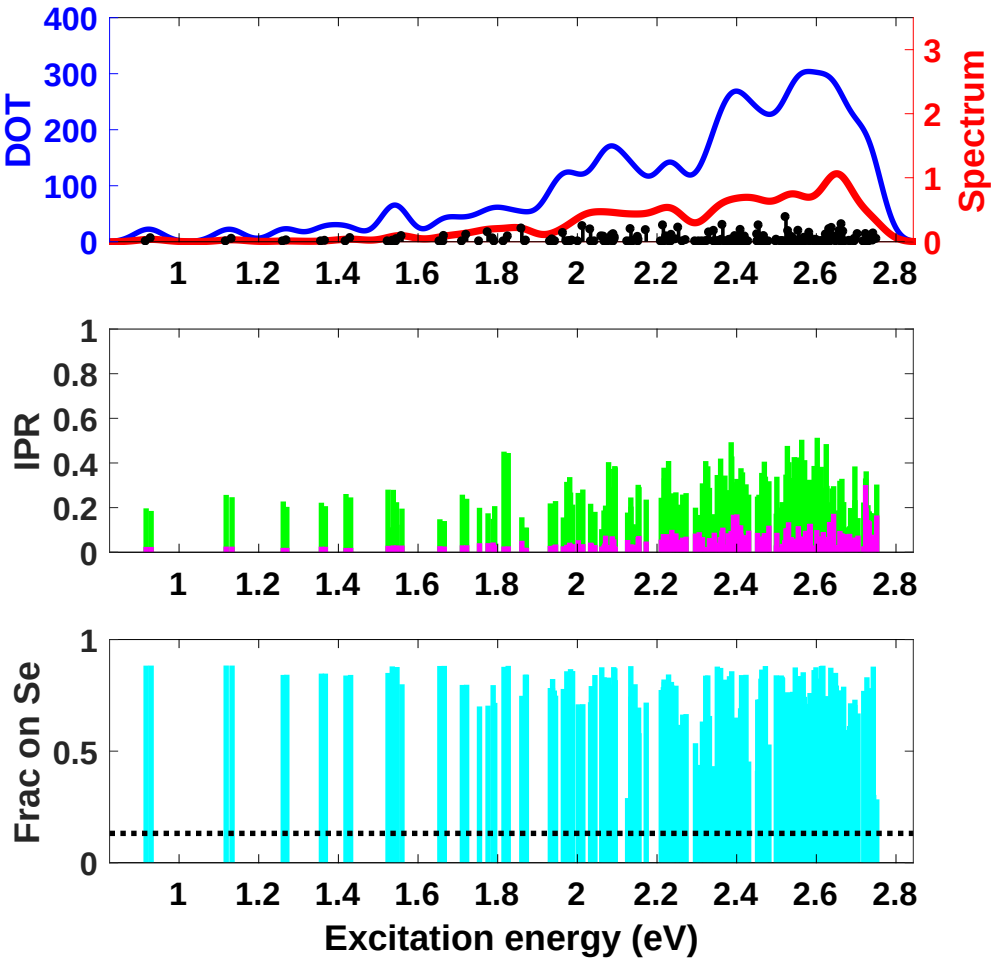

Figure 3.3: TDDFT spectrum, IPR, and charge analysis for the $Cd_{38}Se_{38}$ dot with $MeNH_2$ ligands, at a point early in the optimization (31 meV per atom from the optimized structure). The blue solid line in the TDDFT spectrum is the excited state density of transitions (DOT), the red solid line is the simulated spectrum, and the black stems are the individual TDDFT excitations (with oscillator strengths amplified 15x for easier visualization). The green bars in the IPR represent the electron, and the magenta bars represent the hole. The charge analysis shows the fraction of the hole density on undercoordinated Se atoms. The charge analysis shows the fraction of the hole density on undercoordinated Se atoms. The black dotted line indicates the fraction that would be expected on the 10 undercoordinated Se atoms if the excitation was fully delocalized over all 76 Cd and Se atoms.

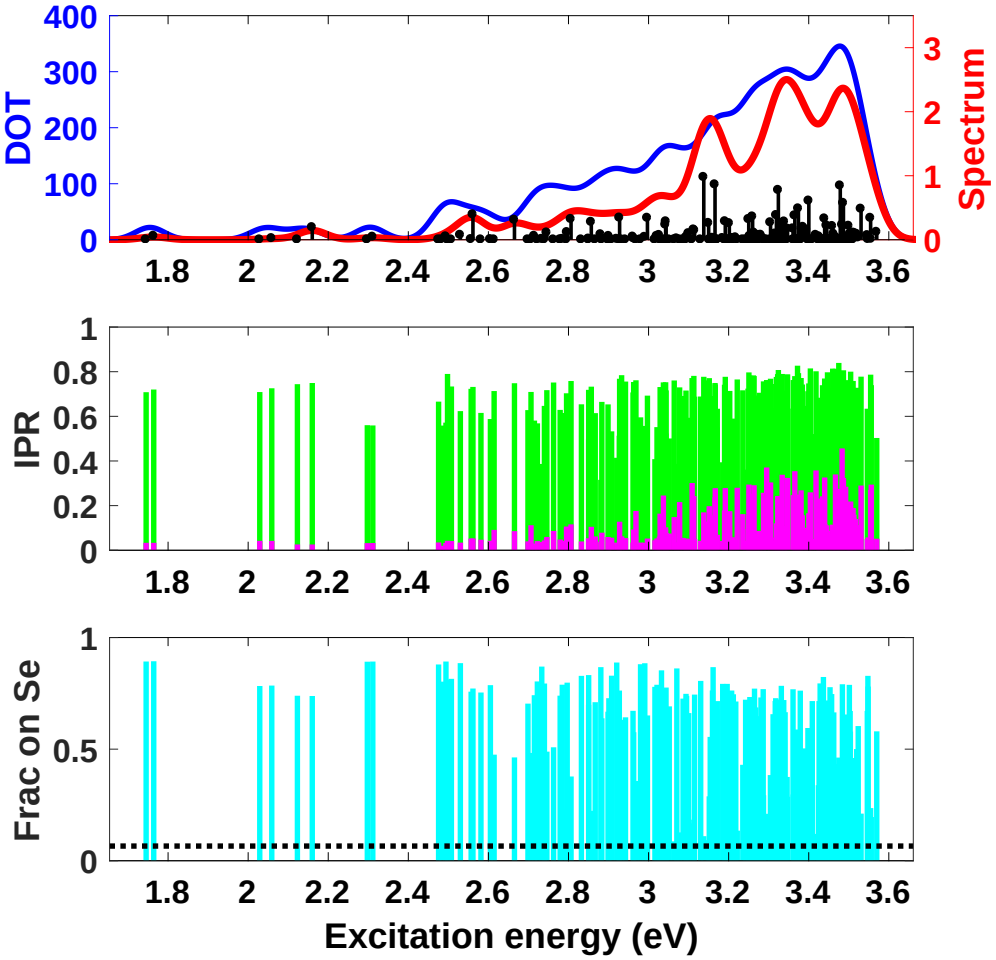

Figure 3.4: TDDFT spectrum (top), IPR (middle), and charge analysis (bottom) for the $Cd_{38}Se_{38}$ dot with $MeNH_2$ ligands, at a point mid-way through the optimization (5 meV per atom from the optimized structure). The blue solid line in the TDDFT spectrum is the excited state density of transitions (DOT), the red solid line is the simulated spectrum, and the black stems are the individual TDDFT excitations (with oscillator strengths amplified 15x for easier visualization). The green bars in the IPR represent the electron, and the magenta bars represent the hole. The charge analysis shows the fraction of the hole density on undercoordinated Se atoms. The charge analysis shows the fraction of the hole density on undercoordinated Se atoms. The black dotted line indicates the fraction that would be expected on the 5 undercoordinated Se atoms if the excitation was fully delocalized over all 76 Cd and Se atoms.

Se atoms on the surface, as discussed in chapter 2. However, from the IPR we can see that there are significantly fewer surface states than in Figs. 3.3 and 3.4—about 36% of holes are on the bulk, and 98% of electrons are on the bulk. This corresponds to both the higher degree of surface reorganization, as well as the smaller number of undercoordinated Se atoms. In the bottom panel of Fig. 3.5 we can see that, as was the case with the less optimized structures, there is a disproportionate amount of hole density localized on the undercoordinated Se atoms in the surface excitations; however, there are fewer excitations with density on these Se atoms, due to the smaller number of surface states.

This effect holds for all systems: as the surface reorganizes and the band gap increases, the excitation energies also increase, and the shape of the spectrum slowly evolves toward that of the final, optimized structure. The effect of surface reorganization on the electron and hole bulk states is summarized in Table 3.1 for $Cd_{38}Se_{38}$ with $MeNH_2$ ligands, Table 3.2 for $Cd_{38}Se_{38}$ with Me_3PO ligands, and Table 3.3 for $Cd_{38}Se_{38}$ with no ligands. For $Cd_{38}Se_{38}$ with both $MeNH_2$ and Me_3PO ligands, surface reorganization leads to an increasingly high percentage of bulk electron states. Since there are no undercoordinated Cd atoms in these systems, and the localized electrons are not disproportionately localized on the undercoordinated Se atoms (see appendix B), it seems likely that this is due to surface reorganization only. The Me_3PO surface reorganizes significantly less than the $MeNH_2$ surface, which is the likely explanation for the slightly lower percentage of bulk electrons in the optimized structure (87% vs 98% in $MeNH_2$). For $Cd_{38}Se_{38}$ with $MeNH_2$ and Me_3PO ligands, the percentage of bulk holes also increases as the surface reorganizes and the number of undercoordinated Se atoms decreases. It is difficult to disentangle the effect of surface reorganization from the reduction in undercoordinated Se atoms—in some sense, they are intimately connected, as the reduction in undercoordinated Se atoms is due to surface reorganization. Therefore, it is difficult to say whether there are more surface hole states in the Me_3PO system due to the larger number of undercoordinated Se atoms (8, vs 4 in the $MeNH_2$ system), the greater decrease in energy in the $MeNH_2$ system, or both. In any case, for both systems, there is significant surface reorganiza-

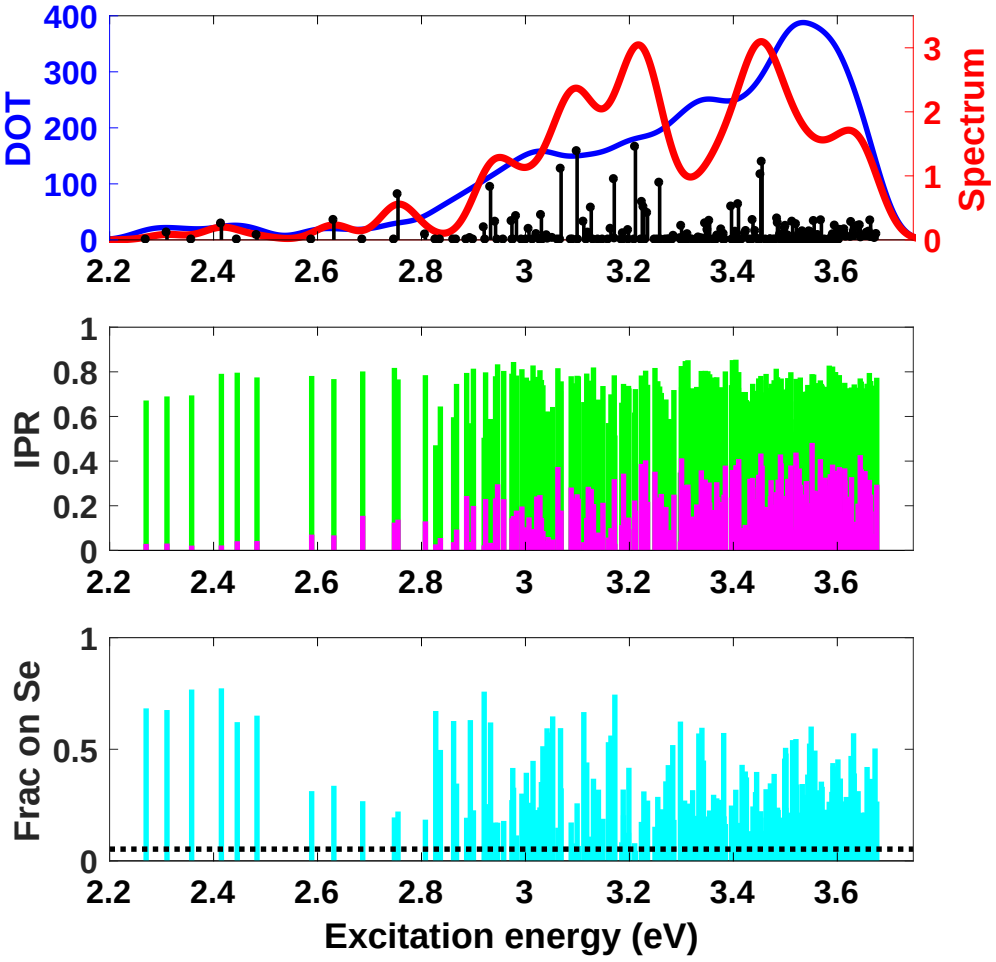

Figure 3.5: TDDFT spectrum (top), IPR (middle), and charge analysis (bottom) for the $Cd_{38}Se_{38}$ dot with $MeNH_2$ ligands, at the final optimized structure. The blue solid line in the TDDFT spectrum is the excited state density of transitions (DOT), the red solid line is the simulated spectrum, and the black stems are the individual TDDFT excitations (with oscillator strengths amplified 15x for easier visualization). The green bars in the IPR represent the electron, and the magenta bars represent the hole. The charge analysis shows the fraction of the hole density on undercoordinated Se atoms. The black dotted line indicates the fraction that would be expected on the 4 undercoordinated Se atoms if the excitation was fully delocalized over all 76 Cd and Se atoms.

Cycle	UC Cd	UC Se	ΔE (eV)	ΔE/atom (meV)	Bulk holes	Bulk electrons
0	0	10	91.40	374.6	N/A	N/A
40	0	10	11.39	46.7	0.0%	0.0%
50	0	10	7.43	30.5	0.5%	1.0%
100	0	7	2.68	11.0	5.1%	78.6%
234	0	5	1.15	4.7	13.3%	91.3%
433	0	4	0.11	0.4	31.6%	96.9%
497	0	4	0.00	0.0	35.7%	98.5%

Table 3.1: Data for the $Cd_{38}Se_{38}$ dot with $MeNH_2$. Cycle indicates the optimization cycle (with 0 being the crystal), UC Cd indicates the number of undercoordinated Cd atoms, UC Se indicates the number of undercoordinated Se atoms, ΔE indicates the total energy difference from the optimized structure, ΔE/atom indicates the energy difference per atom from the optimized structure, bulk holes indicates the percentage of hole states with IPR >0.25, bulk electrons indicates the percentage of electron states with IPR >0.5.

tion accompanied by delocalization of the electron and hole densities, although both systems contain undercoordinated Se atoms at the end of the optimization, which localize hole charge and cause surface states. This is in qualitative agreement with a previous tight-binding study,[54] which observed that bright peaks emerged in the QD spectrum after structural optimization.

The $Cd_{38}Se_{38}$ dot with no ligands tells a slightly more complicated story, with the percentage of bulk electrons remaining low even after reorganization. Here, in addition to undercoordinated Se atoms, we also observe the presence of undercoordinated Cd atoms, due to the lack of ligands. These atoms have been previously connected to electron traps in the ground state band structure.[32,117] Usually these undercoordinated Cd atoms would explain why the percentage of electron states on the bulk is so low in this system, while it quickly reached near 100% in the systems with ligands. However, the Löwdin charge breakdown in Fig. 3.6 for the optimized structure indicates that only a few electron states have disproportionate charge on undercoordinated Cd atoms, nowhere near the number necessary to explain the 63% of localized electron states, suggesting another mechanism for electron trapping is also at play.

As the surface reorganizes, not only do the number of undercoordinated Cd and Se atoms decrease, but the reorganization introduces new trap states, namely a clashing

Cycle	UC Cd	UC Se	ΔE (eV)	ΔE/atom (meV)	Bulk holes	Bulk electrons
0	0	10	43.35	105.2	N/A	N/A
30	0	10	15.02	36.5	0.5%	0.0%
40	0	10	8.95	21.7	1.0%	1.0%
50	0	10	5.19	12.6	3.6%	12.2%
100	0	8	1.25	3.0	17.9%	26.0%
140	0	8	0.30	0.7	18.4%	65.8%
200	0	9	0.48	1.2	21.4%	85.2%
273	0	7	0.00	0.0	24.0%	87.2%

Table 3.2: Data for the $Cd_{38}Se_{38}$ dot with Me_3PO. Cycle indicates the optimization cycle (with 0 being the crystal), UC Cd indicates the number of undercoordinated Cd atoms, UC Se indicates the number of undercoordinated Se atoms, ΔE indicates the total energy difference from the optimized structure, ΔE/atom indicates the energy difference per atom from the optimized structure, bulk holes indicates the percentage of hole states with IPR >0.25, bulk electrons indicates the percentage of electron states with IPR >0.5.

Cycle	UC Cd	UC Se	ΔE (eV)	ΔE/atom (meV)	Bulk holes	Bulk electrons
0	10	10	23.22	305.5	N/A	N/A
30	10	10	8.40	110.5	1.0%	0.0%
40	10	10	7.05	92.7	0.5%	3.1%
50	10	9	6.35	83.6	0.5%	18.4%
75	7	7	5.09	67.0	15.3%	21.4%
100	4	4	3.67	48.4	37.8%	25.5%
150	3	4	0.80	10.5	34.2%	39.8%
200	3	4	0.57	7.5	37.2%	37.8%
273	2	3	0.00	0.0	49.5%	36.7%

Table 3.3: Data for the $Cd_{38}Se_{38}$ dot with no ligands. Cycle indicates the optimization cycle (with 0 being the crystal), UC Cd indicates the number of undercoordinated Cd atoms, UC Se indicates the number of undercoordinated Se atoms, ΔE indicates the total energy difference from the optimized structure, ΔE/atom indicates the energy difference per atom from the optimized structure, bulk holes indicates the percentage of hole states with IPR >0.25, bulk electrons indicates the percentage of electron states with IPR >0.5.

Cd-Cd pair and a clashing Se-Se pair. In chapter 2 we observed the counterintuitive result that undercoordinated Se atoms can act as an electron trap, and we observe this result again here, in addition to the result that Cd atoms can act as hole traps. Careful analysis shows that this behavior is due to the clashing atoms—the Se-Se clash acts as an electron trap, and the Cd-Cd clash acts as a hole trap—as shown in Fig. 3.6. We have classified these clashing atoms as undercoordinated in Table 3.3, as they are not coordinated to 3 or more opposite-type atoms. However, given their effect, it makes sense to separate the two types of traps—in this system, we really have 1 undercoordinated Se atom, 2 clashing Se atoms forming an electron trap, and 2 clashing Cd atoms forming a hole trap. It is not obvious why, given that there are more hole traps in this system than electron traps, the percentage of holes on the bulk would be greater than the percentage of electrons on the bulk. However, it appears that the clashing Se-Se trap has a much stronger effect on electron localization than the clashing Cd-Cd has on hole localization; there are nearly twice as many electron states localized on the Se-Se pair as hole states localized on the Cd-Cd pair. It would seem that the Se-Se trap is simply more effective than the Cd-Cd trap and the undercoordinated Se atom, leading to less delocalization of the electron than the hole.

These clashing features are quite remarkable, and have been largely underappreciated in the literature. As far as we are aware, there have been no reports of clashing Cd atoms causing a hole trap. In fact, previously the Cd-Cd bond motif was suggested as a possible reason why electron traps on Cd atoms are rare, as this motif introduces a way to reduce the number of undercoordinated Cd atoms on the surface.[113] In CdS quantum dots, the S-S disulfide bond has been suggested to act as a surface trap, though it is assumed to be a hole trap.[145] The only mention of Se-Se clashing or bonded atoms forming an electron trap is in a recently published computational work by Baturin et al.[146] using structural enumeration to identify surface defects that were present in very small CdSe clusters ($\leq$ 30 atoms total) with no ligands. They found one such trap in 225 clusters that they explored, and concluded it was very rare. However, we see it in 2 of 4 of our optimized structures, suggesting

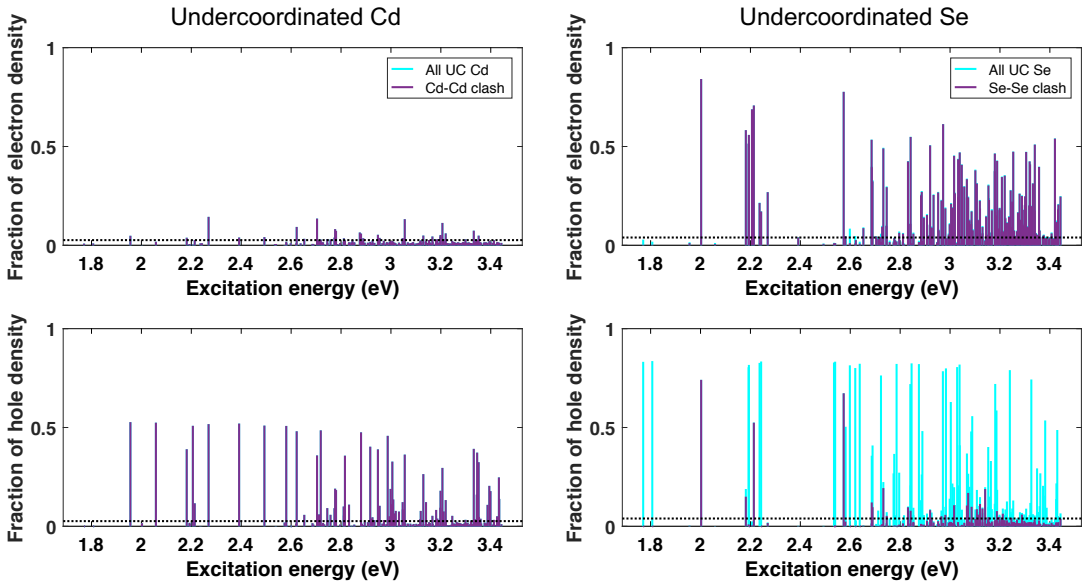

Figure 3.6: Lowdin charge analysis for the $Cd_{38}Se_{38}$ dot with no ligands. Top left: fraction of Lowdin charge for the electron state on the 2 undercoordinated Cd atoms, which are clashing (purple). Bottom left: fraction of Lowdin charge for the hole state on the 2 undercoordinated and clashing Cd atoms (purple). Top right: fraction of Lowdin charge for the electron state on all 3 undercoordinated Se atoms (blue) and on just the 2 clashing Se atoms (purple). Bottom right: fraction of Lowdin charge for the hole state on all 3 undercoordinated Se atoms (blue) and on just the 2 clashing Se atoms (purple). For all panels, the dotted line indicates the fraction of Lowdin charge expected for an excitation delocalized over all atoms (equal to $N_{\text{undercoordinated}}/N_{\text{atoms}}$).

that these clashing atom traps could be relatively common, underappreciated sources of surface traps.

3.4 Conclusion

Here, we have explored the effects of surface reorganization on the presence of surface defects in CdSe quantum dots, and the effect on the excited state spectrum. We have found that surface reorganization, and the accompanying decrease in the number of undercoordinated surface atoms, acts to delocalize the excited states of CdSe, in a similar way that it opens the band gap for the ground state. We find that this delocalization cannot be solely tied to the reduction in undercoordinated atoms, as it occurs even for the excited electrons in systems with no undercoordinated Cd atoms, or other electron traps. We have also found that, while surface reorganization can reduce the number of defects on a quantum dot surface, it can also cause new defects, such as clashing Cd-Cd or Se-Se pairs. This can introduce new trap states, and limit the amount of delocalization that is possible for the excited states.

One interesting result we have found is that, for a given composition, many of the structures reported above are thermally accessible to each other. This means that for a QD at room temperature, it could easily sample configurations with different numbers of traps and different spectral properties. Future work will explore thermal effects on these systems, using molecular dynamics to efficiently generate thermally accessible structures and investigating the ensemble behavior of the absorption spectrum. This will have important implications for understanding how these trap states appear in an experimental spectrum. It would also be instructive to study the structural reorganization of core-shell quantum dots, where many trap states are attributed to the interface, since the core atoms are fully passivated by the shell.

Chapter 4

Electronic structure and surface defects of CdSe/CdS core/shell quantum dots

4.1 Introduction

Core/shell quantum dots (QDs) like CdSe/CdS have become a popular alternative to core-only quantum dots, as they show significantly improved optical properties compared to their core-only counterparts, such as high PLQY and reduced blinking.[14] Core/shell QDs are comprised of a core of one type of material (such as CdSe), coated with an inorganic shell of another material (such as CdS), typically with organic ligands passivating the surface of the shell. The inorganic shell is able to passivate both the anions (Se) and cations (Cd) in the core, leading to a reduced number of trap states and enhanced performance. This has led to adoption of core/shell quantum dots for many applications, such as displays and imaging.[14]

Depending on the alignment of the conduction band (CB) and valence band (VB) of the core and the shell, the electron and hole could be confined to the core, confined to the shell, or delocalized over both.[15,21] In a type I core/shell QD, the VB of the shell is lower energy than the VB of the core, so the hole is confined to the core, and

the CB of the shell is higher energy than the CB of the core, so the electron is also confined to the core. In a type II core/shell QD, the VB of the shell is lower energy than the VB of the core, so the hole is located on the core, and the CB of the shell is lower energy than the CB of the core, so the electron is located on the shell (or vice versa, with the hole located on the shell and electron on the core). There is also an intermediate case, termed quasi-type II, where the VB of the shell is lower than the VB of the core, leading to a hole confined to the core, but the CB of the core and shell are quasi-degenerate, leading to the electron delocalizing over the whole quantum dot (or vice versa, with the hole delocalized and the electron confined). CdSe/CdS typically behaves as a quasi-type II structure, although in some cases such as a large core, it can be type I.[64,65]

The improvement in optical properties for core/shell quantum dots is believed to originate from the presence of the inorganic shell.[14] In core-only CdSe, we showed in chapter 2 that surface traps are largely hole traps originating from undercoordinated Se atoms that cannot be passivated by an organic ligand, as well as surface reorganization that leads to clashing Cd-Cd and Se-Se pairs as shown in chapter 3. In a type I or quasi-type II core/shell QD, the hole is confined to the core of the quantum dot, so the inorganic shell passivates all of the Se atoms on the surface of the core, and the rigid structure of the shell prevents reorganization that could lead to geometric defects in the core, such as clashing atom pairs. This leads to a reduction of surface defect states on the core, and because Cd atoms on the surface of the shell are typically passivated with an organic ligand, should result in nearly no surface states.

Despite their improved optical properties, core/shell quantum dots can still show undesirable features such as blinking that could be caused by traps.[20,66–68] In many cases, these defects are attributed to the interface between the core and the shell, where the core and shell materials can have large lattice mismatches, for example 13% in CdSe/ZnS.[21] However, in CdSe/CdS, the two materials have the same Wurtzite crystal structure and the lattice mismatch is small (4%), and so defects have been attributed to the surface of the shell.[20]

Previous theoretical work on core/shell quantum dots has been limited due to the

large size of the systems. Most work has used tight binding methods[18–20] to investigate these systems for computational efficiency. Three studies investigated CdSe/CdS passivated with pseudohydrogens with DFT using the local density approximation (LDA), two reported that the structures are quasi-type II, with the LUMO delocalized over the core and shell but the HOMO confined to the core,[69,70] and another found that zinc blende CdSe/CdS is type I, with the HOMO and LUMO confined to the core.[71] While some other work with a higher level of DFT has been conducted on other types of core/shell quantum dots,[147–149] we are not aware of any other DFT studies on CdSe/CdS.

In this chapter, we investigate the electronic structure of CdSe/CdS quantum dots with density functional theory, paying particular attention to the source of traps and defects, as well as the band alignment and location of the conduction and valence bands. We find that surface hole traps are prevalent on all of the structures studied, indicating that simply passivating the core Se atoms is not sufficient to eliminate hole traps in CdSe/CdS. In addition, we find that the QDs studied here are "double" quasi-type II heterostructures, indicating that both the valence and conduction bands are deloclized over the core and the shell. However, both the valence and conduction bands are located on half of the QD, usually next to a S and Cd facet, respectively.

4.2 Methods

4.2.1 Initial structures

For all quantum dots, the initial structure was carved from the bulk wurtzite CdSe crystal. Given a total radius for the core/shell QD, we carve a spherical CdSe quantum dot with this radius out of the bulk CdSe, with the center of the dot at the center of the Cd_6Se_6 hexagonal cage. We then trim any singly-coordinated atoms from the surface, and replace any Se atoms in the area between the core radius and the total radius with S, to create a CdSe/CdS core/shell structure.

Using this procedure, we obtain a series of CdSe/CdS QDs with varying core

and shell sizes. We study one series of CdSe/CdS with increasing core size and the minimum amount of shell to fully passivate the surface of the core: $Cd_{33}Se_{33}/Cd_{57}S_{57}$, $Cd_{48}Se_{48}/Cd_{90}S_{90}$, and $Cd_{63}Se_{63}/Cd_{101}S_{101}$. In the unoptimized crystal structure, this corresponds to approximately 1.3 nm diameter core with 1.5 Å thick shell, 1.5 nm diameter core with 1.7 Å thick shell, and 1.7 nm diameter core with 1.2 Å thick shell. We also study one series of CdSe/CdS with constant core size and increasing shell size: $Cd_{33}Se_{33}/Cd_{57}S_{57}$, $Cd_{33}Se_{33}/Cd_{87}S_{87}$, and $Cd_{33}Se_{33}/Cd_{105}S_{105}$. In the unoptimized crystal structure, this corresponds to 1.3 nm diameter core, with shell thickness of 1.5 Å, 2.3 Å, and 2.7 Å. For both of these series, we explore the role of surface ligands by studying each QD with and without $MeNH_2$ ligands. We also explore the effect of passivating the surface Cd and S by studying HCl and HF ligands on the smallest QD, $Cd_{33}Se_{33}/Cd_{57}S_{57}$. For the HF and HCl ligands, H is bound to S and F or Cl is bound to Cd.

4.2.2 Geometry optimization

The geometries of all quantum dots were optimized in CP2K,[150] using the PBE functional[137] with norm-conserving Goedecker–Teter–Hutter (GTH) pseudopotentials.[151] CP2K uses combined Gaussian and plane wave basis sets; Cd, Se, and S atoms used the basis DZVP-MOLOPT-SR-GTH, while ligand atoms used DZVP-MOLOPT-GTH.[152] We used a plane wave cutoff of 400 Ry and a relative cutoff of 60 Ry. We used a cubic simulation box with length 30 Å in all directions for structures with no ligands and length 50 Å in all directions for structures with ligands. We did not use periodic boundary conditions.

4.2.3 Ground state DFT calculations

All ground state electronic structure calculations were performed with DFT using the PBE0 functional[120] and LANL2DZ basis set[138–141] in the QChem software package.[136]

The band structure, or density of states (DOS), can be calculated from the orbital

energies (E_{orb}):

$$\text{DOS} = \sum_i \frac{1}{\sqrt{2\pi\sigma^2}} \exp\left(-\frac{(E - E_{\text{orb},i})^2}{2\sigma^2}\right) \tag{4.1}$$

With a broadening parameter of σ =100 meV. The density of states can be broken down to show the contribution of each atom to each orbital, which is called the projected density of states (PDOS). First, the molecular orbitals are symmetrically orthonormalized, using the expression:

$$C_{\text{norm}} = S^{-\frac{1}{2}} C \tag{4.2}$$

Where C is the unnormalized MO coefficient matrix, and S is the overlap matrix. Then, each molecular orbital ψ can be expanded in the atomic orbital basis using the following expression:

$$\psi_k = \sum_{i \in \text{core}} \alpha_{ik} \chi_i + \sum_{j \in \text{shell}} \beta_{jk} \chi_j \tag{4.3}$$

Where χ_i is an atomic orbital associated with the core, χ_j is an atomic orbital associated with the shell, α_{ik} is the contribution of MO k due to core atomic orbital χ_i, and β_{jk} is the contribution of MO k due to shell atomic orbital χ_j.

The total fraction of MO k on the core atoms is then given by

$$\alpha_k = \sum_{i \in \text{core}} \alpha_{ik}^2 \tag{4.4}$$

and the fraction on the shell is given by

$$\beta_k = \sum_{j \in \text{shell}} \beta_{jk}^2 \tag{4.5}$$

Then, the PDOS is calculated by weighing the DOS by α or β:

$$\text{PDOS}_{\text{core}} = \sum_k \frac{\alpha_k}{\sqrt{2\pi\sigma^2}} \exp\left(-\frac{(E - E_{\text{orb},k})^2}{2\sigma^2}\right) \tag{4.6}$$

$$\mathrm{PDOS}_{\mathrm{shell}} = \sum_k \frac{\beta_k}{\sqrt{2\pi\sigma^2}} \exp\left(-\frac{(E - E_{\mathrm{orb},k})^2}{2\sigma^2}\right) \tag{4.7}$$

While equations 4.3–4.7 are written in terms of core and shell atoms, they can be generalized to a breakdown across any number of different ways of partitioning the atoms.

4.2.4 Inverse Participation Ratio

We use the inverse participation ratio (IPR) to measure the delocalization of the orbitals in the density of states. First, we conduct a Löwdin charge analysis for each orbital to obtain a set of charges on each atom for that orbital. The Löwdin charge of an orbital will add to 2, because each orbital contains (or, for virtual orbitals, could contain) 2 electrons. We normalize the Löwdin charge so that it adds to 1 for each orbital.

We then use these charges to calculate the IPR for each orbital:

$$\mathrm{IPR} = \frac{1}{N \sum_A (q_A)^2} \tag{4.8}$$

Where N is the number of atoms and q_A is the normalized Löwdin charge on atom A for the orbital in question. The IPR is defined such that, for a completely delocalized orbital, $q = \frac{1}{N}$ for all atoms, and the IPR = 1. However, for an orbital fully localized on one atom, $q = 1$ for that atom and 0 for all others, and the IPR will be equal to $\frac{1}{N}$. Thus, the IPR gives us one number for each orbital that can be used to distinguish localized (surface) states from delocalized (bulk) states. Because delocalization in core/shell dots can be complicated—for example, you could have an orbital delocalized over all of the core atoms, all of the shell atoms, or the whole QD, each of which would give a different IPR—we do not choose a particular cutoff to define a surface vs. bulk state. Instead, we use the IPR in conjunction with the PDOS and orbital visualization to determine the character of the orbitals.

4.3 Results and discussion

4.3.1 Surface structure

Tables 4.1–4.3 show the number of different types of defects for each structure studied here. Cd defect refers to a Cd atom that is undercoordinated, clashing, or both, and S defect refers to an S atom that is undercoordinated, clashing, or both. To determine undercoordinated atoms we used a bond length cutoff of 3.1 Å and to determine clashing atoms we used a bond length cutoff of 3.0 Å, both chosen based on histograms of interatomic distances as described in appendix A. In general, we see the same behavior as in chapter 2, that putting ligands on Cd and relaxing the structure is not sufficient to eliminate undercoordinated S atoms. In addition, we see a similar trend to that in chapter 3, where the presence of ligands in the optimization leads to less reorganization, evidenced by the increased number of undercoordinated S atoms for the structures with methylamine ligands. Notably, the structures with HCl and HF ligands show none of the defects identified in chapters 2 and 3.

It is important to note that for the structures with methylamine, nearly every structure had ligands detach from surface Cd atoms that are bound to 3 S atoms over the course of the optimization, leaving behind a 3-coordinate Cd. We find that these detached ligands do not contribute trap states and that their orbitals are buried deep within the valence and conduction bands, and thus we simply ignore them in this analysis. For the two methylamine structures where there is one undercoordinated Cd atom, this is due to the atom detaching from an S rather than a ligand falling off.

4.3.2 Surface traps

Fig. 4.1 shows the projected density of states and orbital IPR for the QD series with increasing shell size ($Cd_{33}Se_{33}/Cd_{57}S_{57}$, $Cd_{33}Se_{33}/Cd_{87}S_{87}$, and $Cd_{33}Se_{33}/Cd_{105}S_{105}$) and Fig. 4.2 shows the same for the series with increasing core size ($Cd_{48}Se_{48}/Cd_{90}S_{90}$ and $Cd_{63}Se_{63}/Cd_{101}S_{101}$) with no ligands. The PDOS is broken down across several different types of atoms—core atoms, shell atoms that aren't associated with surface

Structure	Cd UC	S UC	Cd clash	S clash	Cd defect	S defect
$Cd_{33}Se_{33}/Cd_{57}S_{57}$	18	18	12	12	18	18
$Cd_{33}Se_{33}/Cd_{87}S_{87}$	8	9	6	6	8	9
$Cd_{33}Se_{33}/Cd_{105}S_{105}$	3	3	0	0	3	3
$Cd_{48}Se_{48}/Cd_{90}S_{90}$	3	3	0	0	3	3
$Cd_{63}Se_{63}/Cd_{101}S_{101}$	8	5	0	0	8	5

Table 4.1: Number and type of defects in core/shell QDs with no ligands. Cd (S) UC refers to the number of undercoordinated Cd (S) atoms, Cd (S) clash refers to the number of clashing Cd (S) atoms, and Cd (S) defect refer to the total number of Cd (S) atoms that are undercoordinated and/or clashing. For these structures, all the clashing atoms are also undercoordinated, so the number of defects is just equal to the number of undercoordinated atoms.

Structure	Cd UC	S UC	Cd clash	S clash	Cd defect	S defect
$Cd_{33}Se_{33}/Cd_{57}S_{57}$	1	17	12	12	12	17
$Cd_{33}Se_{33}/Cd_{87}S_{87}$	1	11	8	8	8	11
$Cd_{33}Se_{33}/Cd_{105}S_{105}$	0	5	0	0	0	5
$Cd_{48}Se_{48}/Cd_{90}S_{90}$	0	8	0	0	0	8
$Cd_{63}Se_{63}/Cd_{101}S_{101}$	0	11	0	0	0	11

Table 4.2: Number and type of defects in core/shell QDs with methylamine ligands. Cd (S) UC refers to the number of undercoordinated Cd (S) atoms, Cd (S) clash refers to the number of clashing Cd (S) atoms, and Cd (S) defect refer to the total number of Cd (S) atoms that are undercoordinated and/or clashing. For these structures, all of the undercoordinated Cd are also clashing, so the number of Cd defects is equal to the number of clashing Cd atoms. In addition, all of the clashing S atoms are also undercoordinated, so the number of S defects is equal to the number of undercoordinated S atoms.

defects, Cd defects, and S defects. In general, we see that all of these structures' density of states are dominated by traps at the valence band edge, but do not show mid-gap traps separated from the valence band. We see that defects associated with S atoms cause a number of peaks at the valence band edge, in addition to a few peaks deep in the conduction band; further breakdown by type of trap indicates that, consistent with our previous reports, undercoordinated S atoms cause the traps in the valence band, while clashing S-S pairs cause the traps deep in the conduction band. In addition, we see that defects associated with Cd atoms cause a number of peaks in both the valence band and conduction band. Further breakdown based on type of trap reveals that the peaks in the valence band are due to clashing Cd-Cd pairs, while both undercoordinated and clashing Cd atoms contribute to the peaks in the

Ligand	Cd UC	S UC	Cd clash	S clash	Cd defect	S defect
HCl	0	0	0	0	0	0
HF	0	0	0	0	0	0

Table 4.3: Number and type of defects in $Cd_{33}Se_{33}/Cd_{57}S_{57}$ with HF and HCl ligands. Cd (S) UC refers to the number of undercoordinated Cd (S) atoms, Cd (S) clash refers to the number of clashing Cd (S) atoms, and Cd (S) defect refer to the total number of Cd (S) atoms that are undercoordinated and/or clashing.

conduction band. Inspection of the IPR reveals that none of the conduction band edge orbitals are strongly localized, and visual inspection confirms that these orbitals are quite delocalized, suggesting this contribution from Cd defects is not indicative of the presence of trap orbitals at the conduction band edge. The nature of the conduction band orbitals will be discussed further in the next section, but the absence of electron traps despite the presence of 2-coordinate Cd atoms has been reported before.[35]

Figs. 4.3–4.4 show the PDOS for the same QDs but with methylamine ligands on the surface Cd atoms. Ligands tend to increase the HOMO–LUMO gap, although not always, notably for the smallest $Cd_{33}Se_{33}/Cd_{57}S_{57}$ dot the ligands slightly decrease the value of the HOMO–LUMO gap. It would appear that the ligands lower the energy of S-related hole traps, but raise the energy of Cd-related hole traps. The Cd-related hole traps are all due to clashing Cd-Cd pairs, and it would make sense that adding a ligand to these clashing Cd atoms would increase the energy of that trap due to steric repulsion. The mechanism of lowering the S-related trap energy is unclear, although it has been reported that ligands can shield the surface from the vacuum and stabilize the energy of surface atoms.[32] This could be at play here. However, while ligands decrease the energy of most of the hole traps, they do not eliminate them, likely because they are not bound to the S atoms that cause the majority of hole traps.

Interestingly, while some of these traps are caused by previously-identified surface features like undercoordinated and clashing atoms, the IPR reveals that there are a number of localized trap states at the valence band edge whose source is not accounted for. Visual inspection of the QD orbitals reveals the presence of highly

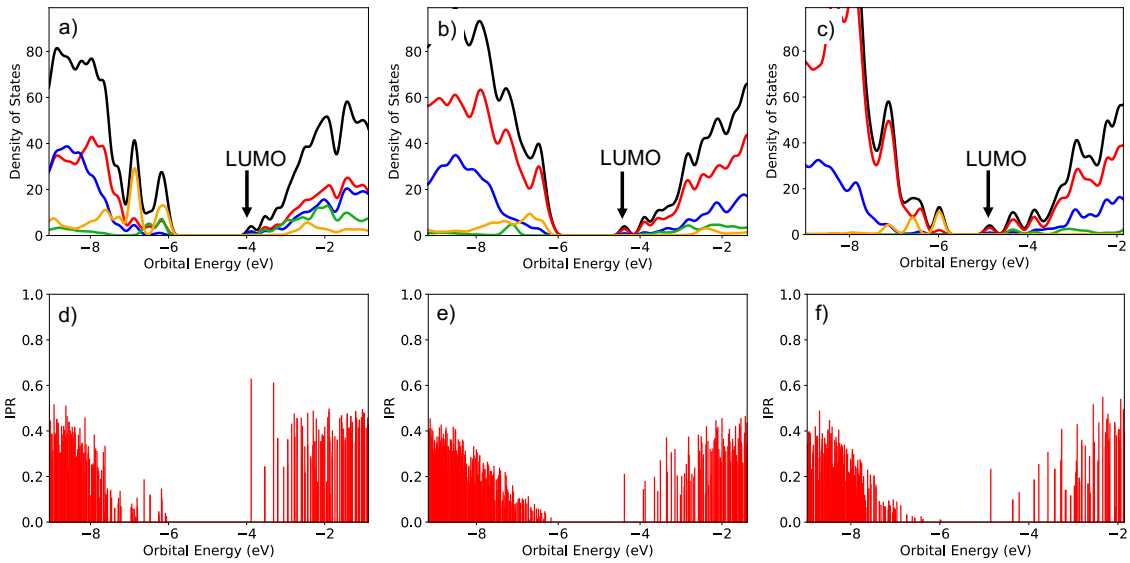

Figure 4.1: Projected density of states (PDOS) and orbital inverse participation ratio (IPR) for the series with constant core and increasing shell size, with no ligands. PDOS is broken down over core atoms (blue), shell atoms that are not associated with defects (red), Cd defects (green), S defects (orange), and all atoms (black). a) PDOS for $Cd_{33}Se_{33}/Cd_{57}S_{57}$ b) PDOS for $Cd_{33}Se_{33}/Cd_{87}S_{87}$ c) PDOS for $Cd_{33}Se_{33}/Cd_{105}S_{105}$ d) IPR for $Cd_{33}Se_{33}/Cd_{57}S_{57}$ e) IPR for $Cd_{33}Se_{33}/Cd_{87}S_{87}$ f) IPR for $Cd_{33}Se_{33}/Cd_{105}S_{105}$.

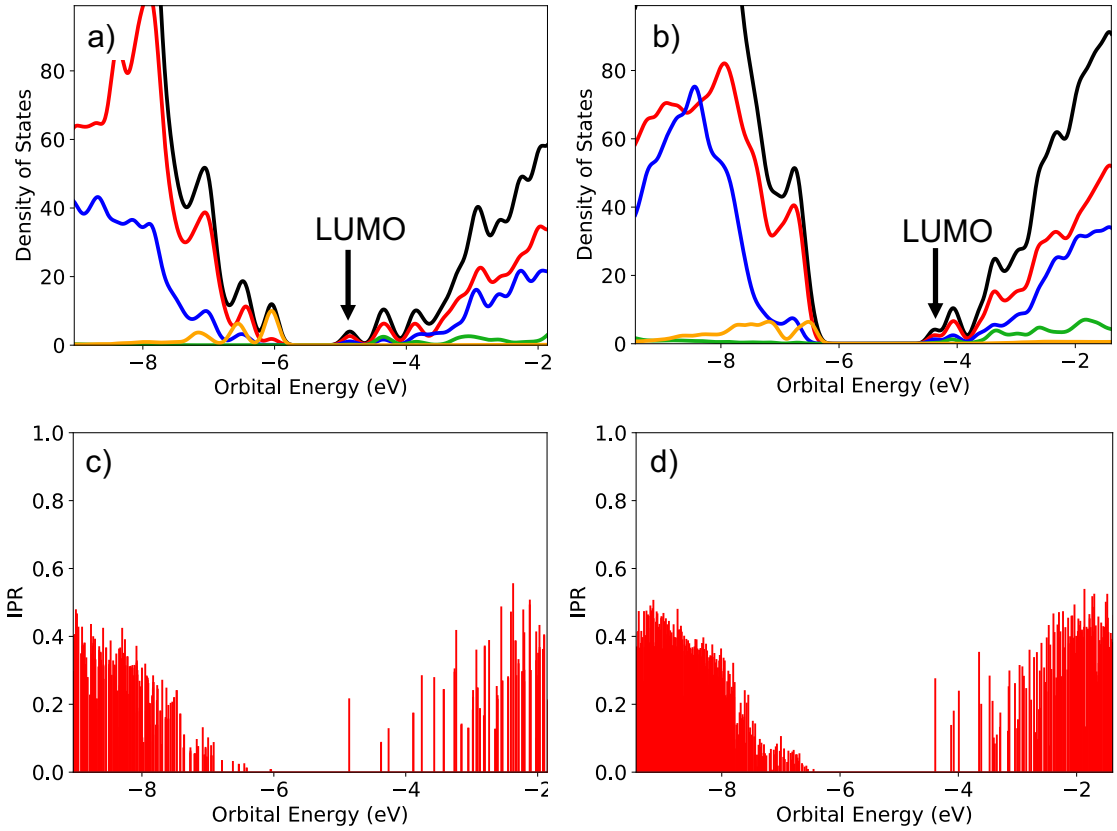

Figure 4.2: Projected density of states (PDOS) and orbital inverse participation ratio (IPR) for the series with increasing core size and approximately constant shell thickness, with no ligands. PDOS is broken down over core atoms (blue), shell atoms that are not associated with defects (red), Cd defects (green), S defects (orange), and all atoms (black). a) PDOS for $Cd_{48}Se_{48}/Cd_{90}S_{90}$ b) PDOS for $Cd_{63}Se_{63}/Cd_{101}S_{101}$ c) IPR for $Cd_{48}Se_{48}/Cd_{90}S_{90}$ d) IPR for $Cd_{63}Se_{63}/Cd_{101}S_{101}$. Compare to the smallest core size, $Cd_{33}Se_{33}/Cd_{57}S_{57}$, in Fig. 4.1a and d.

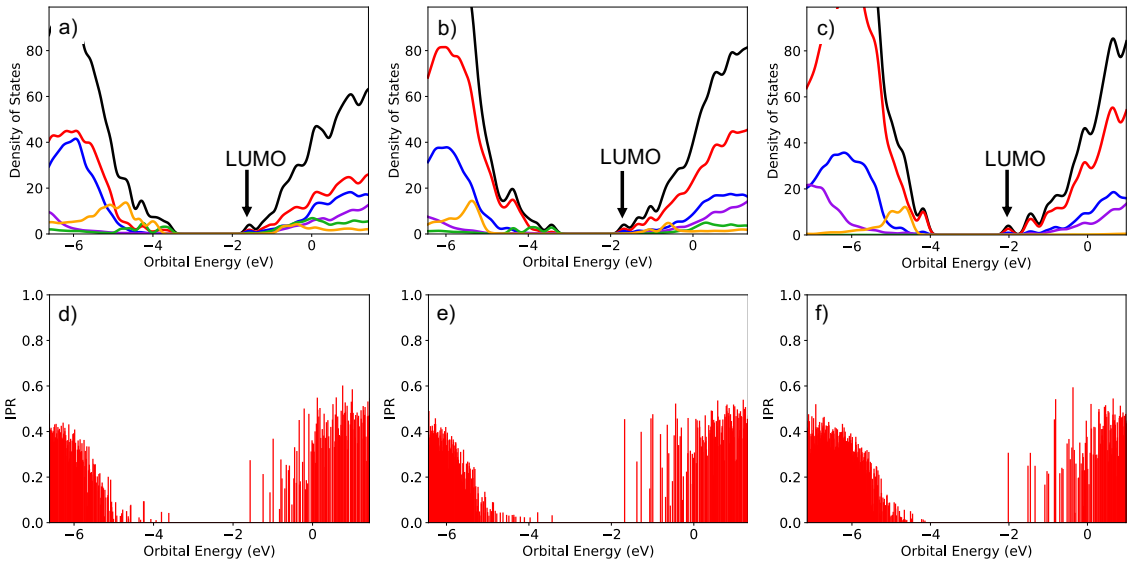

Figure 4.3: Projected density of states (PDOS) and orbital inverse participation ratio (IPR) for the series with constant core and increasing shell size, with $MeNH_2$ ligands. PDOS is broken down over core atoms (blue), shell atoms that are not associated with defects (red), Cd defects (green), S defects (orange), ligands (purple), and all atoms (black). a) PDOS for $Cd_{33}Se_{33}/Cd_{57}S_{57}$ b) PDOS for $Cd_{33}Se_{33}/Cd_{87}S_{87}$ c) PDOS for $Cd_{33}Se_{33}/Cd_{105}S_{105}$ d) IPR for $Cd_{33}Se_{33}/Cd_{57}S_{57}$ e) IPR for $Cd_{33}Se_{33}/Cd_{87}S_{87}$ f) IPR for $Cd_{33}Se_{33}/Cd_{105}S_{105}$.

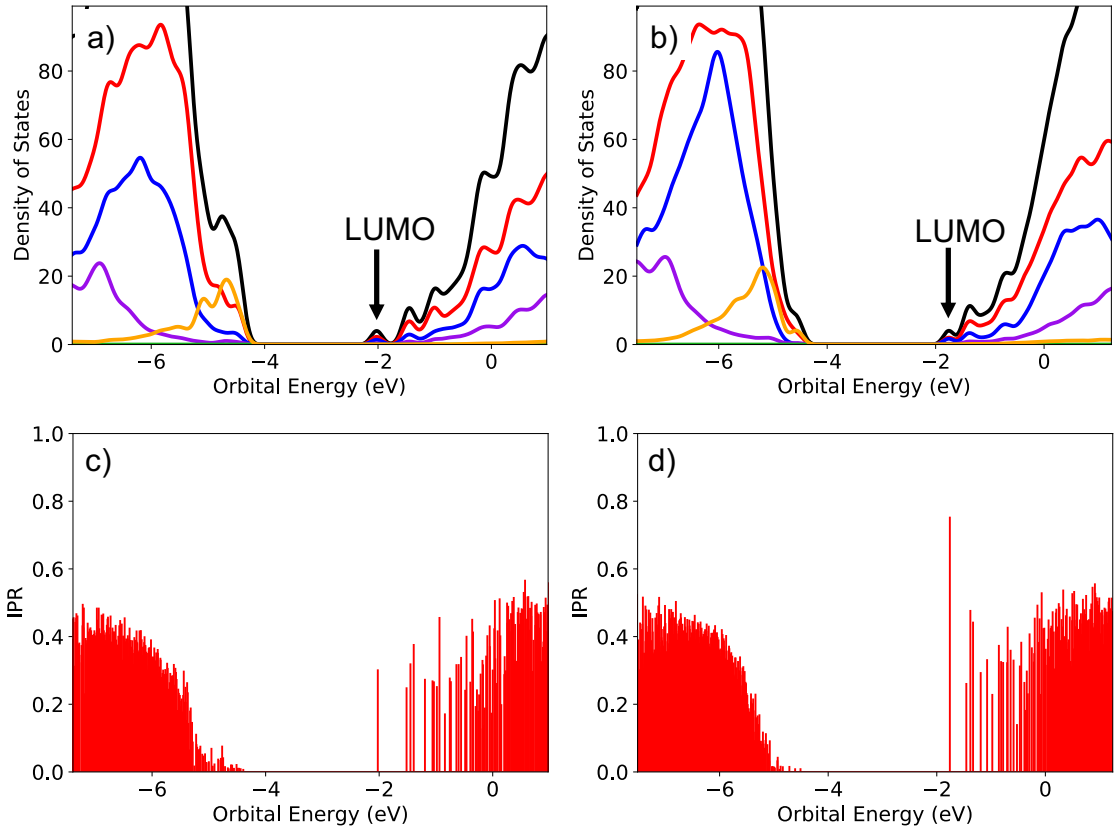

Figure 4.4: Projected density of states (PDOS) and orbital inverse participation ratio (IPR) for the series with increasing core size and approximately constant shell thickness, with $MeNH_2$ ligands. PDOS is broken down over core atoms (blue), shell atoms that are not associated with defects (red), Cd defects (green), S defects (orange), ligands (purple), and all atoms (black). a) PDOS for $Cd_{48}Se_{48}/Cd_{90}S_{90}$ b) PDOS for $Cd_{63}Se_{63}/Cd_{101}S_{101}$ c) IPR for $Cd_{48}Se_{48}/Cd_{90}S_{90}$ d) IPR for $Cd_{63}Se_{63}/Cd_{101}S_{101}$. Compare to the smallest core size, $Cd_{33}Se_{33}/Cd_{57}S_{57}$, in Fig. 4.3a and d.

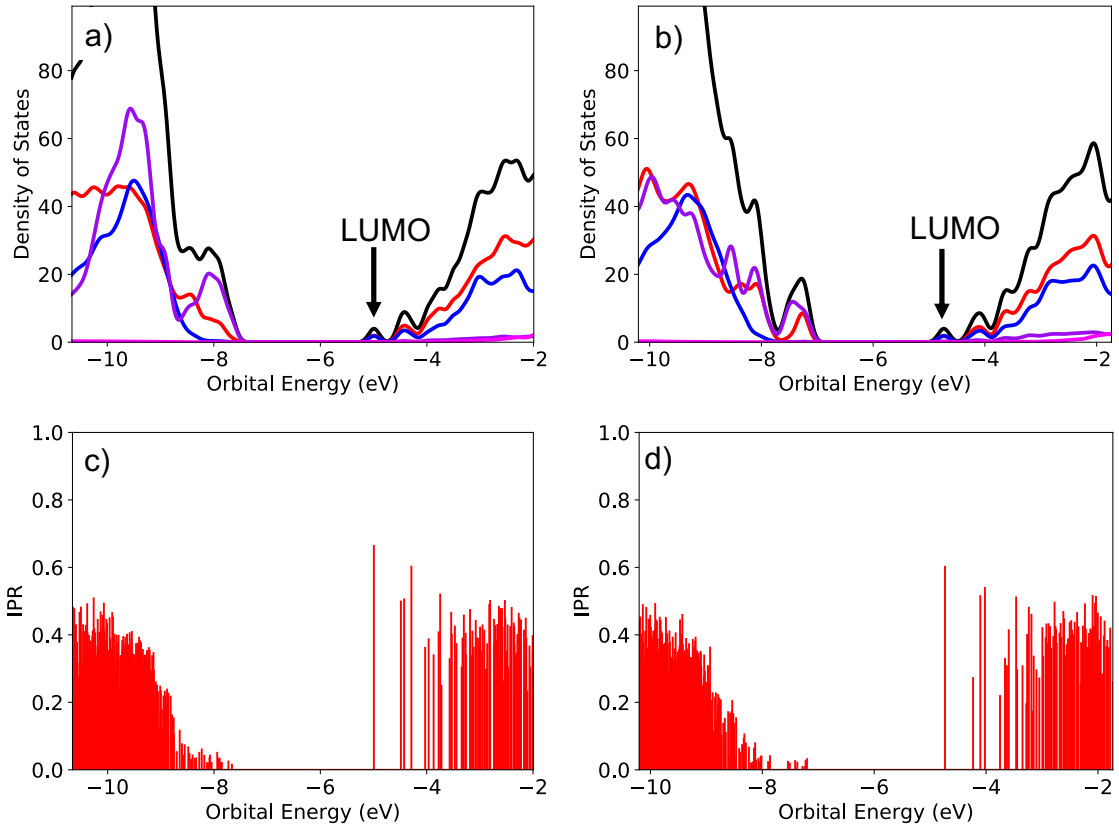

Figure 4.5: Projected density of states (PDOS) and orbital inverse participation ratio (IPR) for $Cd_{33}Se_{33}/Cd_{57}S_{57}$ with HX ligands. PDOS is broken down over core atoms (blue), shell atoms (red), chalcogenide ligands (purple), H ligands (magenta), and all atoms (black). There are no defect atoms in these structures. a) PDOS for $Cd_{33}Se_{33}/Cd_{57}S_{57}$ with HF b) PDOS for $Cd_{33}Se_{33}/Cd_{57}S_{57}$ with HCl c) IPR for $Cd_{33}Se_{33}/Cd_{57}S_{57}$ with HF d) IPR for $Cd_{33}Se_{33}/Cd_{57}S_{57}$ with HCl. Compare to $Cd_{33}Se_{33}/Cd_{57}S_{57}$ with no ligands in Fig. 4.1a and d, and $Cd_{33}Se_{33}/Cd_{57}S_{57}$ with $MeNH_2$ ligands in $Cd_{33}Se_{33}/Cd_{57}S_{57}$ in Fig. 4.3a and d.

localized traps on some 3-coordinate surface S atoms in every structure except for $Cd_{33}Se_{33}/Cd_{57}S_{57}$, which can be seen for $Cd_{33}Se_{33}/Cd_{87}S_{87}$ with methylamine ligands in Fig. 4.7a. We also see relatively delocalized trap states located on the S-rich facets of our QDs, which can be seen for $Cd_{33}Se_{33}/Cd_{87}S_{87}$ with methylamine ligands in Fig. 4.7b. These traps are similar to those hypothesized by Lei et al. for their S-rich CdSe/CdS dot-in-nanoplatlet heterostructures.[145] Cui et al. reported for CdSe core-only dots that while undercoordinated atoms were a good predictor of hole trap location, the real mechanism behind formation of hole traps is high nucleophilicity of surface atoms.[60] They found that undercoordination is correlated with nucleophilicity, but not equivalent. It could be that these S atoms, while not 2-coordinate, are highly nucleophilic for some reason; this would be a fruitful line of inquiry for a future work.

For CdSe core-only dots, it has been shown that using carboxylic acid ligands, with the proton on Se and the carboxylate group on Cd, removed the presence of surface hole traps from the TDDFT spectrum.[57] We explored this route, but for computational efficiency we used HCl and HF ligands, as Cl ions have also been shown to be effective ligands for CdSe.[35,37] These results are shown in Fig. 4.5. However, here we see new traps introduced by the highly electronegative Cl and F ions, suggesting that the organic nature of the carboxylate group was important to those findings. The presence of hole traps on Cl and F in HCl and HF passivated core-only CdSe has been reported before, and attributed to the fact that these atoms are more nucleophilic than Se, causing the hole to localize on these atoms *instead* of Se.[60] This is consistent with our observations here, that the nucleophilic Cl and F ions replace the S atoms as the primary source of hole traps, as we notice that the band structure is generally much cleaner than the bare and $MeNH_2$ passivated structures. In the HCl and HF passivated structures we do not see the presence of any S defect atoms, and the especially clean band structure for HF passivated CdSe/CdS suggests the absence of the delocalized hole traps on 3-coordinate S atoms for this system.

The prevalence of these surface traps is somewhat surprising, as core/shell quantum dots have been reported to have significantly improved optical properties com-

pared to core-only quantum dots.[36] However, despite this improvement, core/shell CdSe/CdS still shows blinking and other behaviors that are often caused by trap states, and surface states have been hypothesized to be the culprit, given the relatively small lattice offset between CdSe and CdS.[20] Sowers et al. found that CdSe/CdS core/shell QDs with S-rich surfaces produced mid-gap and valence band edge hole traps using density functional tight binding theory, in agreement with their experiments on S-rich CdSe/CdS.[20] Lei et al. suggested based on experimental evidence that CdSe/CdS dot/platlet nanostructures also showed a continuum of delocalized trap states on S-rich facets of the shell.[145] Our findings here support these hypotheses, and suggest that CdSe/CdS core/shell quantum dots are affected by the same pervasive and difficult to remove surface states that plague CdSe core-only dots.

4.3.3 Bulk states

The blue and red lines in Figs. 4.1–4.5 represent the contribution to the DOS from the core and non-defect shell atoms, respectively. CdSe/CdS is believed to be a quasi-type II heterostructure, with the hole (valence band) located on the CdSe core and the electron (conduction band) delocalized over the core and shell.[15,65] We see that the LUMO, as well as most of the conduction band, is delocalized over both the core and shell, as would be expected. However, in every structure, we see that the shell PDOS dominates the valence band (or, in the case of the HX ligands, contributes equally), instead of the core dominating as would be predicted based on experiments and effective mass theory.

In order to better determine the character of the bulk QD states, we visualized the orbitals for each structure. From the PDOS, the character of the conduction band was clear—delocalized over the core and the shell. Upon visualization we can confirm that for every structure, the LUMO through LUMO+3 are delocalized over the core and the shell, and the LUMO displays the classic S-like envelope function while the LUMO+1 and LUMO+2 (and usually the LUMO+3, although not always) display the classic P-like envelope function. We therefore conclude that for every system, the LUMO is the conduction band minimum (CBM). However, surprisingly, we find that

for almost every case these unoccupied orbitals are located on half of the QD, rather than symmetrically delocalized over the whole structure. For every structure except $Cd_{33}Se_{33}/Cd_{57}S_{57}$ with and without ligands and $Cd_{63}Se_{63}/Cd_{101}S_{101}$ with ligands, the LUMO through LUMO+3 are located on the half of the QD closest to a large Cd-rich facet.

In $Cd_{63}Se_{63}/Cd_{101}S_{101}$ with ligands, the LUMO through LUMO+3 are symmetrically delocalized over the whole QD. $Cd_{63}Se_{63}/Cd_{101}S_{101}$ has only very small Cd- and S-rich facets consisting of a few atoms, whereas the other structures have large Cd- and S-rich facets. This suggests that the near-absence of these facets in combination with ligand passivation facilitates delocalization of the conduction band over the whole QD structure. For $Cd_{33}Se_{33}/Cd_{57}S_{57}$ with and without ligands, we do see the half-dot nature of the conduction band orbitals, however they are located on a formally S-rich facet. For these structures, the edge of the S-rich facet features nearly all of the Cd defect atoms, suggesting that the unoccupied orbitals in this system localized on the side of the dot with Cd defects, rather than the side with a clean Cd-rich facet. We see a similar effect in $Cd_{63}Se_{63}/Cd_{101}S_{101}$ without ligands, where the majority of the electron density in the LUMO through LUMO+4 is evenly delocalized on a Cd-rich facet, but there is significant electron density on the Cd defect atoms that distorts the shape of the envelope functions. These observations explain the strong contribution of Cd defect atoms in the conduction band of $Cd_{33}Se_{33}/Cd_{57}S_{57}$ with and without ligands and $Cd_{63}Se_{63}/Cd_{101}S_{101}$ without ligands; the conduction band is a delocalized bulk state, as evidenced both by the IPR and visualization, however it is delocalized on the part of the QD where the Cd defects are, so they contribute disproportionately to the CB despite not creating a trap state. For the other structures, Cd defect contribution to the CB seems to arise from a similar situation, that the CB is delocalized over Cd defects near to the Cd-facet, indicating simply that these atoms are contributing to a delocalized bulk state rather than localizing a trap.

Turning to the valence band, based on the PDOS we would conclude that the VBM is located on the shell. As mentioned in the previous section on surface traps,

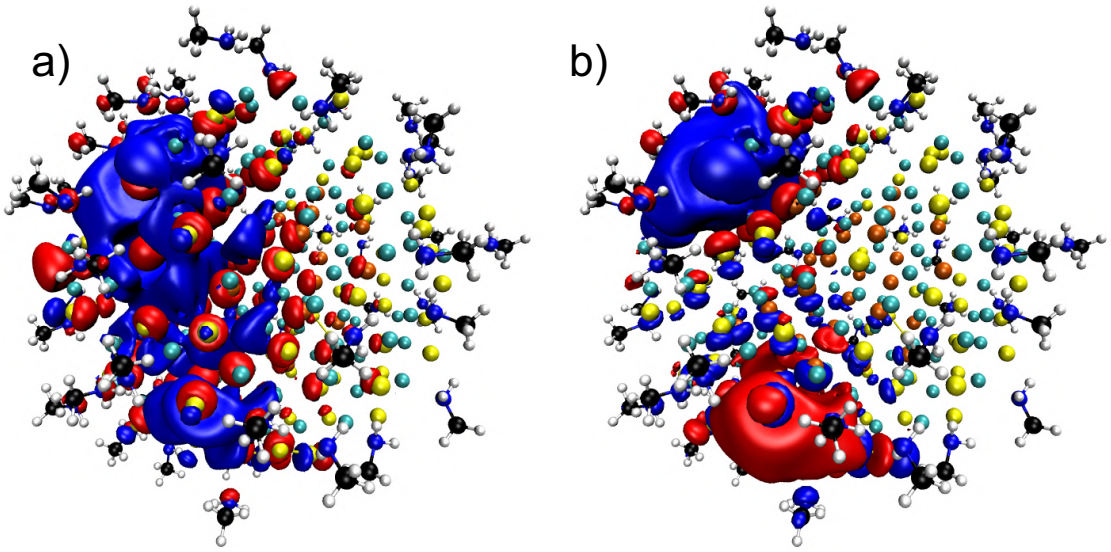

Figure 4.6: Selection of representative unoccupied orbitals for $Cd_{33}Se_{33}/Cd_{87}S_{87}$ with methylamine ligands. a) LUMO (S-like) b) LUMO+1 (P-like). The atom colors are: Cd=cyan, Se=orange, S=yellow, C=black, N=blue, H=white.

there are a large number of surface trap states at the valence band edge in all systems. Many of these localized surface traps are associated with 3-coordinate S atoms that we have classified here as part of the shell, rather than as a defect. In addition, many trap states associated with S defects are also delocalized onto nearby shell atoms. Both of these effects would cause an apparent contribution of shell atoms to the PDOS near the valence band edge, despite these orbitals actually being traps and not indicative of the character of the bulk state. The IPR can tell us if a state is localized or delocalized, but cannot reveal any information about where the orbital is located, making it of limited use for distinguishing delocalized trap states from a "bulk" orbital on the core or half of the QD. It is thus very difficult to identify the valence band maximum (VBM) from the PDOS or IPR due to the continuum of both localized and delocalized trap states at the valence band edge. It is also difficult to visually identify the VBM, as it not clear what the nature of the valence band maximum should be—traditionally it is believed to be delocalized over the core atoms only, however from the PDOS it would appear that there is likely at least some delocalization onto the shell, or that the valence band maximum could be in the shell

only. Further, the half-dot nature of the conduction band would suggest that the valence band maximum could also be half-dot, located perhaps near the S-rich facet. Therefore, we rely on a combination of visual identification, IPR, and the band gap to identify the valence band maximum.

In Fig. 4.7, we show a selection of representative occupied orbitals for $Cd_{33}Se_{33}/Cd_{87}S_{87}$ with $MeNH_2$ ligands, and use these as a case study, because these types of orbitals are common to all the structures studied here. We do not see any orbitals located solely on the core, all of the occupied orbitals are either all in the shell or delocalized over the core and the shell. Fig. 4.7a shows a clear localized trap orbital on 3-coordinate S atoms, with a very low IPR of 0.02, nearly no electron density in the core, and giving a band gap of 2.29 eV. Fig. 4.7b shows an orbital that is lower in energy, which is located on the same area as the trap orbital and is nearly all in the shell but is significantly more delocalized in nature, giving a band gap of 2.69 eV. Fig. 4.7c shows the first "half-dot" orbital; it is located on the S-rich facet of the QD, but is the first orbital with an IPR > 0.1 and has about 30% of electron density in the core (for comparison, about 28% of QD atoms are in the core for this system), and gives a band gap of 3.34 eV. Fig. 4.7d shows the first mostly delocalized orbital, which is relatively symmetrically delocalized over the core and the shell (27% of density on the core), although the majority of the density is located on the side with the S-rich facet, giving a band gap of 3.59 eV. Fig. 4.7e shows the first fully delocalized orbital, which is the first orbital with an IPR > 0.3, and is clearly symmetrically delocalized over the entire QD, with 30% of electron density in the core and giving a band gap of 3.89 eV. This gradual transition from trap orbital to fully delocalized orbital makes it difficult to assign the valence band maximum, as choosing any one of these would reflect prior bias—if we believe the orbital should be delocalized over the core and shell symmetrically, we would pick orbital 4.7e, if we think the orbital should be half-dot like the LUMO, we would pick 4.7c, if we think it would be only in the shell, we would pick 4.7b.

One more promising way to identify the VBM would be using the band gap. Our previous calculations yield a band gap of 3.5 eV for $Cd_{33}Se_{33}$ with methylamine

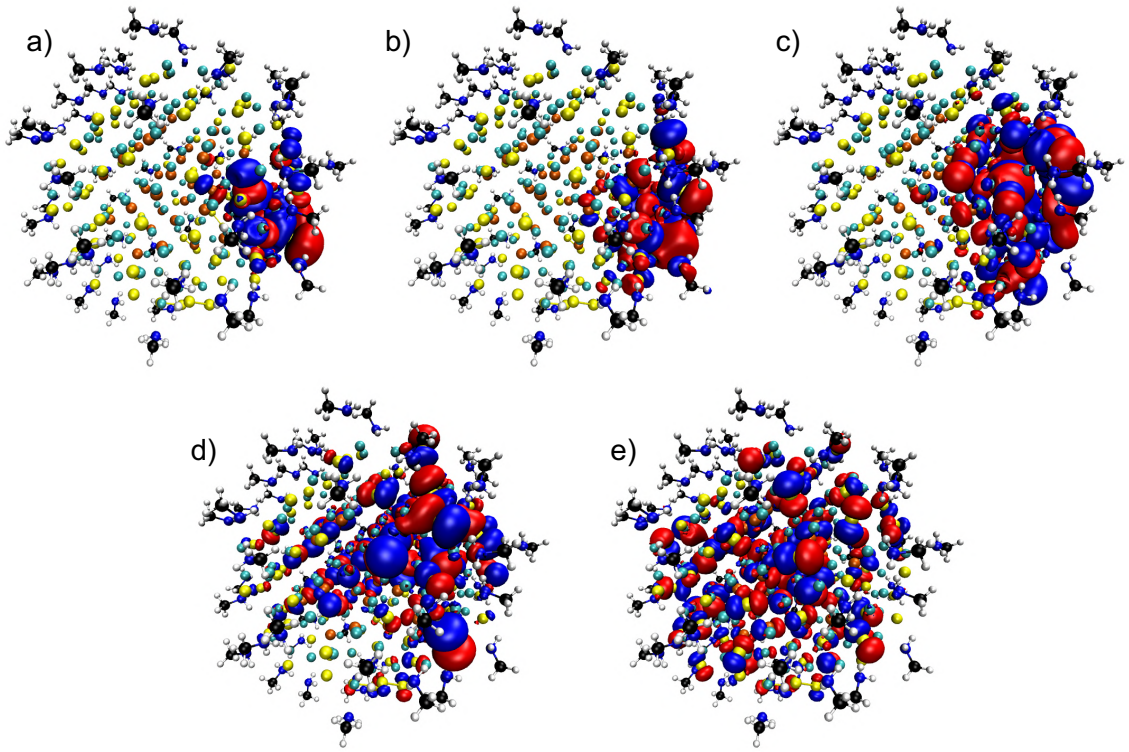

Figure 4.7: Selection of representative occupied orbitals for $Cd_{33}Se_{33}/Cd_{87}S_{87}$ with methylamine ligands. a) HOMO-3 b) HOMO-8 c) HOMO-22 d) HOMO-36 e) HOMO-67. The structures are in the same spatial orientation as Fig. 4.6.

ligands. CdSe/CdS core/shell quantum dots have been shown to undergo redshift of the band gap in the presence of a shell and with increasing shell size.[15] However, the magnitude of this redshift varies, with some reports of similarly sized CdSe/CdS quantum dots undergoing a red shift of about 0.1 eV with 0.6 monolayers of CdS shell (about 1.95 Å) and up to 0.3 eV with 2 monolayers (about 6.5 Å),[153] while another report showed a red shift of only 0.02 eV with a 4.1 Å shell, and a red shift of 0.17 eV with a shell of 12.9 Å.[154] Our $Cd_{33}Se_{33}/Cd_{87}S_{87}$ structure has a similarly sized core to these structures and a shell thickness of about 2.3 Å. Given these experimental reports, and our previous finding of a band gap of 3.5 eV for $Cd_{33}Se_{33}$, we can conclude that we would expect the band gap of $Cd_{33}Se_{33}/Cd_{87}S_{87}$ to be around 3.5 eV–3.2 eV. This means that our shell-only orbitals yield too small a band gap to be the VBM, and would suggest that Fig. 4.7c represents the VBM in this system. When the orbitals form a near-continuum, choosing one to be the VBM is fraught, but nearly all of the orbitals close in energy to this one are very similar shape and character, so it is reasonable to conclude that if this orbital is not the VBM, the VBM is similar to this one. These results suggest that the valence band maximum is delocalized over the core and the shell; overall, 28 % of atoms are in the core, and based on the PDOS analysis, this orbital has 30% of electron density in the core. However, the VBM is located only on half of the QD, and orbitals deeper in the VB are either half-dot or delocalized over the whole dot. Notably, the VBM is on the side of the dot *opposite* to the CBM; this is true for every dot studied here.

There are a few potential explanations for this finding that the valence band maximum is delocalized over the core and shell. The first is that these QDs are smaller than would typically be used in experiment, which can affect the band alignment. For example, CdSe/CdS QDs with small cores have been found to be quasi-type II heterostructures, but those with larger cores have been found to be type I.[15,64,65] These findings are for dots larger than those studied here, and it is possible that for these very small QDs, the valence band of the core and shell become close enough in energy to support a delocalized hole state. Another potential explanation is that the large number of trap states associated with the surface of the shell hybridize with the

bulk orbitals, bringing the energy of shell orbitals closer to the valence band edge and allowing them to contribute to the bulk state. Sowers et al.[20] also make this argument to support their finding that the HOMO in their CdSe/CdS system is located on a S-rich facet instead of in the core. Given the transition from trap orbital in Fig. 4.7a to potential valence band maximum in Fig. 4.7c, as well as the much lower valence band onset in the HF passivated QD where the F atoms cause traps instead of S, it seems that this could be a likely possibility.

The finding that the CBM and VBM are located on half the dot has been reported before in the computational literature, with Sowers et al.[20] finding the HOMO and LUMO in their CdSe/CdS system to be located on opposite sides of the QD surface, and Kilina et al.[147] reporting that their LUMO was delocalized but only on one side of a CdSe/ZnS dot. The finding that the CBM and VBM are always on opposite sides of the QD is interesting. The VB orbitals typically arise due to anion (Se or S) orbitals and the CB orbitals arise due to cation (Cd) orbitals,[14] so it is not so surprising that if they are localizing on half the dot, the CB would localize on the Cd-rich side and the VB would localize on the S-rich side. However, the mechanism driving the CB to localize on half the dot is not clear, except for in $Cd_{33}Se_{33}/Cd_{57}S_{57}$ where the CB is located near Cd defects. In any case, the majority of the argument for the quasi-type II band alignment in CdSe/CdS comes from two pieces of evidence: the band gap red shifts upon shell growth, and the carrier overlap decreases with increasing shell growth.[15,64,65,155] Both of these properties would be retained in our scenario, where the electron and hole are located on opposite halves of the dot; the band gap should still red shift with increasing shell size since the carriers are delocalized into the shell, and their overlap should decrease with increasing shell size because they are located on opposite sides of the QD. That would make this model a compelling alternative to the effective mass model of core/shell QDs. On the other hand, one experimental study has shown directly that the hole is in fact confined to the core by adding hole and electron quenching ligands to the surface, and finding no change in the spectroscopic properties in the presence of hole quenching ligands, but significant decrease in quantum yield and emission in the presence of electron quenching ligands;

this indicates that the hole does not have access to the surface of the QD.[156] However, given the variability in band alignment between type I and quasi-type II, it is not infeasible that in some cases the hole is in fact confined to the core, while in others it is on half the dot.

4.4 Conclusion

In this chapter we have investigated the electronic structure of CdSe/CdS quantum dots using DFT. We found that, for all QDs studied here, the valence band edge is dominated by localized trap states, some of which are associated with previously identified defects but some of which are localized on seemingly ordinary atoms. We found that these trap states seem to hybridize with the bulk states, leading to the valence band being delocalized over the core and the shell but located on half of the dot, instead of a symmetric orbital located on the core as would be expected for a quasi-type II structure. We also find that the conduction band minimum is delocalized over the core and the shell on half of the dot, and that the CBM and VBM are located on opposite sides of the QD. We studied the effects of increasing the core keeping the shell thickness approximately constant, increasing the shell keeping the core constant, and the effect of ligands. We found that for each of these scenarios, the above conclusions hold, with the exception of $Cd_{63}Se_{63}/Cd_{101}S_{101}$ with $MeNH_2$ ligands, where the CB is delocalized symmetrically over the whole QD.

These findings have a number of important implications. The prevalence of traps in every structure suggests that understanding and controlling the surface chemistry of CdSe/CdS is important for producing QDs with good optical properties; this is in agreement with experimental work suggesting that often a very thick shell is required to separate the hole from the surface.[38] It also suggests that the presence or absence of traps could change the location of the VBM, which is important to understand when choosing CdSe/CdS for applications where it is important for the hole to be confined within the core. The finding that the presence of surface traps can influence the location of the VBM (and potentially CBM) also highlights the importance of

atomistic simulations for these systems, as these properties could not arise out of a simple effective mass model. Overall, this work advances our understanding of the importance of surface chemistry to CdSe/CdS core/shell dots.

Future work will focus on studying a system that has no traps, such as CdSe/CdS capped with CdX_2 ligands, which has shown to produce trap-free structures for core-only CdSe QDs,[35] or a CdSe/CdS structure with a very thick shell.[38] This will help us elucidate the location of the valence band in these systems, without the added complication of surface traps. We will also investigate other systems such as CdSe/ZnS, which is a type I heterostructure, to see if the conclusions here transfer to other systems.

Chapter 5

Investigation of External Quantum Efficiency Roll-Off in OLEDs Using the Mean Field Steady State Kinetic Model

The basis of this chapter is published as:

Alexandra R. McIsaac, Valerie Vaissier Welborn, Markus Einzinger, Nadav Geva, Hayley Weir, Marc A. Baldo, and Troy Van Voorhis. Investigation of External Quantum Efficiency Roll-Off in OLEDs Using the Mean-Field Steady-State Kinetic Model. *J. Phys. Chem. C*, 124(27):14424–14431, July 2020.

5.1 Introduction

Organic light-emitting diodes (OLEDs) have been widely adopted for display purposes, and are promising candidates for applications in organic lasing[73–79] and solid-state lighting.[80–86] However, these applications require devices that operate at higher brightness and current density than is needed for displays. This represents a technological challenge because this operating regime in OLEDs is limited by efficiency "roll-off" or "droop," a phenomenon where the external quantum efficiency decreases

with increasing current density.[72] Identifying a device's roll-off mechanism would help overcome this challenge and facilitate rational design for performance improvement. Much work has been done in this context, both experimental and theoretical. Experimental studies deduce the mechanism by fitting phenomenological kinetic models to time-resolved photoluminescent data. Kinetic Monte Carlo is the typical theoretical tool for modeling this type of problem, as it allows for molecular-scale simulations of OLED devices.[93–95] Of the many causes of efficiency roll-off that have been proposed, the two most prominent mechanisms are exciton-exciton annihilation (EEA) and exciton-charge annihilation (ECA), the relative importance of which is highly debated.[72] This debate stems from finding different dominant mechanisms, both theoretically[96–99] and experimentally,[87–92] for different types of OLEDs, suggesting that it could be device-dependent.

Theoretical approaches have the undeniable advantage of allowing the decoupling of the various mechanisms suspected to govern OLED performance. Although kinetic Monte Carlo models incorporate the microscopic details that are required to understand the physics of efficiency roll-off,[93,98,158] their applicability is limited by their high computational cost. Therefore, a microscopic model that is fast enough to study the large number of different OLEDs and ways they can be modified would be a powerful tool.

In this chapter we investigate device roll-off using a simple, fast model of OLED photophysics, which can simulate an experimental roll-off curve in a matter of seconds. We show that, in a pair of carefully designed devices, the mechanism of roll-off can be tuned by modifying only the host material. Our model includes the key microscopic rates that govern OLED performance (charge injection, recombination, light emission, quenching) and includes nanoscale heterogeneity by using the mean field steady-state (MFSS) formalism, which has been shown to give results comparable to kinetic Monte Carlo at a fraction of the computational cost.[100] Applying this model to simulate two devices based on thermally activated delayed fluorescence (TADF) that differ only in their emitting layer, we find that a single set of model rate constants is able to reproduce both the external quantum efficiency roll-off curve and

the photoluminescence quantum yield roll-off curve for a given device. Because of the external heavy-atom effect, one of the devices has enhanced TADF, and the model shows that this change in rate is sufficient to change the dominant roll-off process from exciton-exciton annihilation to exciton-charge annihilation. This approach has great promise for the future, both in terms of extracting microscopic rates from mesoscopic OLED measurements and in terms of speeding up the rational design of OLEDs with reduced roll-off.

5.2 Methods

5.2.1 Mean Field Steady State Picture

We model the emitting layer of an OLED as a two-dimensional lattice, where each site is chosen to be about the size of the host molecule (**Figure 5.1**). Because the emitting layer is really three-dimensional, each site represents an average over the depth of the layer. Due to disorder in the emitting layer (for example, due to being on a host vs guest site or due to the orientation of molecules in the layer), a given process will happen at a different rate at each molecular site, which we account for by giving each site a different rate constant (indicated by the different colors in the right panel of Figure 5.1). Each site is assigned a rate constant from a log-normal distribution characterized by mean $\overline{\ln(k)}$ and width σ:

$$P\left(\ln(k)\right) = \frac{1}{\sqrt{2\pi\sigma^2}}\exp\left(-\frac{(\ln(k)-\overline{\ln(k)})^2}{2\sigma^2}\right) \tag{5.1}$$

The log-normal distribution of rate constants was chosen as it corresponds to a Gaussian distribution of energies at each site.

5.2.2 Kinetic Scheme

Each lattice site has a certain population of excitons (ϵ), charges (c), and vacancies (ϕ). A vacancy means that the site is empty. Assuming perfect charge balance

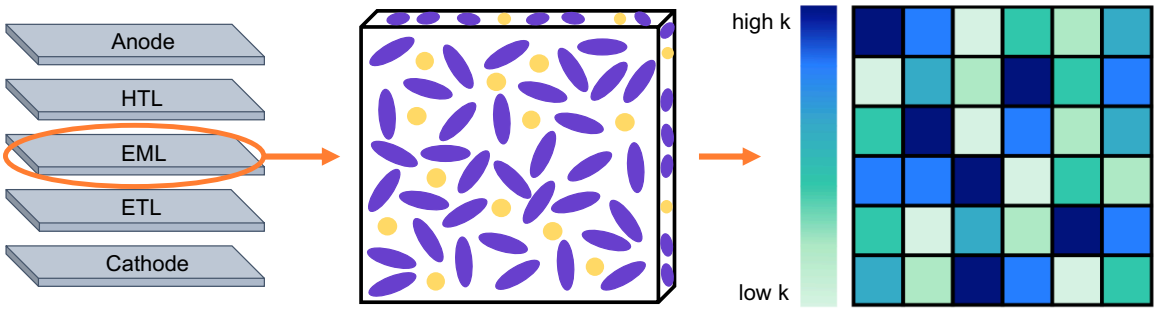

Figure 5.1: Translating an OLED into a lattice model. Left: Diagram of an OLED, with a hole transport layer (HTL), emitting layer (EML), electron transport layer (ETL), as well as a cathode and anode. Center: Cartoon depiction of the emitting layer of the OLED, with purple ovals and yellow circles depicting the host/guest system. Right: A lattice model of the emitting layer. The colors on the lattice indicate the rate constant, k, at each site.

(concentration of electrons and holes are equal), we consider a generic "charge," which could be an electron or a hole. Finally, excitons can be singlets or triplets. However, since singlets radiate on a much faster time scale than triplets, this assumption is equivalent to assuming there are only triplet excitons in the simulation. While it would be preferable to distinguish between singlet and triplet excitons, this would add extra parameters to our model, and cause complications due to the different radiative timescales. Singlets do not generally participate in the annihilation steps that cause roll-off,[72] so neglecting them should not significantly change our conclusions. **Figure 5.2** shows the processes that we consider, occurring in the emitting layer during an electroluminescence experiment. All bimolecular processes occur between species on neighboring sites.

Here we present an overview of our model. For a full derivation, see appendix C. The steady-state rate equations for the populations of excitons, charges, and vacancies at a given lattice site, call it site i, are:

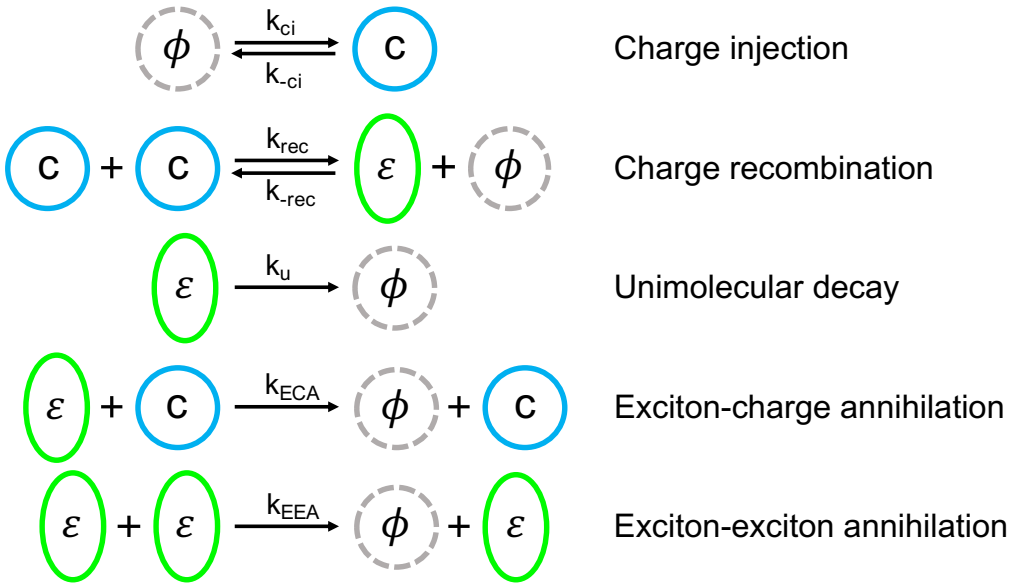

Figure 5.2: Processes considered in the lattice model. ϕ indicates a vacancy (empty site), c indicates a charge (electron or hole), and ϵ indicates an exciton. Note that the bimolecular processes can occur only when the two species are on neighboring sites.

$$\frac{\mathrm{d}\epsilon_i}{\mathrm{d}t} = -k_{\mathrm{u}}\epsilon_i + \sum_{nn}(k_{\mathrm{rec}}c_i c_{nn} - k_{-\mathrm{rec}}\epsilon_i\phi_{nn} - k_{\mathrm{EEA},i}\epsilon_i\epsilon_{nn} - k_{\mathrm{ECA},i}\epsilon_i c_{nn}) \tag{5.2}$$

$$\frac{\mathrm{d}c_i}{\mathrm{d}t} = k_{\mathrm{ci}}\phi_i - k_{-\mathrm{ci}}c_i + \sum_{nn}(-2k_{\mathrm{rec}}c_i c_{nn} + k_{-\mathrm{rec}}\epsilon_i\phi_{nn} + k_{-\mathrm{rec}}\phi_i\epsilon_{nn}) \tag{5.3}$$

$$\begin{aligned}\frac{\mathrm{d}\phi_i}{\mathrm{d}t} = &-k_{\mathrm{ci}}\phi_i + k_{-\mathrm{ci}}c_i + k_{\mathrm{u}}\epsilon_i + \sum_{nn}(k_{\mathrm{rec}}c_i c_{nn} - k_{-\mathrm{rec}}\phi_i\epsilon_{nn} \\ &+ k_{\mathrm{EEA},i}\epsilon_i\epsilon_{nn} + k_{\mathrm{ECA},i}\epsilon_i c_{nn}),\end{aligned} \tag{5.4}$$

Where the rate constants are defined in Figure 5.2. ϵ_i, c_i and ϕ_i denote the fraction of the site i that is occupied by excitons, charges, and vacancies (e.g. $\epsilon_i = \frac{[\epsilon]_i}{[\epsilon]_i+[c]_i+[\phi]_i}$); ϵ_{nn}, c_{nn} and ϕ_{nn} denote the fraction of a nearest neighbor site occupied by excitons, charges, and vacancies, and $\sum_{nn}$ indicates a sum over the sites that neighbor site i. While we do not place limits on these site fractions except requiring that they add to 1, in practice they are always above 0.

In principle, any or all of the rate constants could be drawn from a log-normal

distribution. However, drawing every rate constant from a distribution would require every rate constant to have a different disorder parameter, leading to a large number of unconstrained parameters and risking overfitting the model. In kinetic Monte Carlo, typically disorder is incorporated in one rate, specifically the transport or diffusion rate.[96] However, we found that diffusion did not play a significant role in this model, and we ultimately left it out of the model presented here. We instead follow the same approach of kinetic Monte Carlo, including disorder in one rate at a time, but only in the rates that we find most strongly affect the roll-off portion of the curve: k_{EEA} and k_{ECA}. All other processes are characterized by a single rate constant for all sites. We did also investigate disorder in k_{u}, but found that it primarily affected the turn-on regime and never led to the best fit. We did not look at disorder in the charge injection or charge leakage rates, as this would complicate the calculation of the charge density. We also did not consider disorder in the recombination rate, as this was consistently the fastest process and thus should not be rate-determining.

We then make the mean field approximation, replacing the sum over nearest neighbors with an ensemble average, and assume steady state:

$$\frac{\mathrm{d}\epsilon_i}{\mathrm{d}t} = 0 = -k_{\mathrm{u}}\epsilon_i + N(k_{\mathrm{rec}}c_i\bar{c} - k_{-\mathrm{rec}}\epsilon_i\bar{\phi} - k_{\mathrm{EEA},i}\epsilon_i\bar{\epsilon} - k_{\mathrm{ECA},i}\epsilon_i\bar{c}) \tag{5.5}$$

$$\frac{\mathrm{d}c_i}{\mathrm{d}t} = 0 = k_{\mathrm{ci}}\phi_i - k_{-\mathrm{ci}}c_i + N(-2k_{\mathrm{rec}}c_i\bar{c} + k_{-\mathrm{rec}}\epsilon_i\bar{\phi} + k_{-\mathrm{rec}}\phi_i\bar{\epsilon}) \tag{5.6}$$

$$\begin{aligned}\frac{\mathrm{d}\phi_i}{\mathrm{d}t} = 0 = &-k_{\mathrm{ci}}\phi_i + k_{-\mathrm{ci}}c_i + k_{\mathrm{u}}\epsilon_i + N(k_{\mathrm{rec}}c_i\bar{c} - k_{-\mathrm{rec}}\phi_i\bar{\epsilon} \\ &+ k_{\mathrm{EEA},i}\epsilon_i\bar{\epsilon} + k_{\mathrm{ECA},i}\epsilon_i\bar{c})\end{aligned} \tag{5.7}$$

Where N is the number of nearest neighbors (here, $N = 4$). $\bar{\epsilon}$, $\bar{c}$, and $\bar{\phi}$ indicate the ensemble average population of excitons, charges, and vacancies over the lattice. We can solve equations 5.5–5.7 to obtain ϵ_i, c_i, and ϕ_i.

Notice that ϵ_i, c_i, and ϕ_i are functions of $\bar{\epsilon}$, $\bar{c}$, and $\bar{\phi}$. These averages are defined as:

$$\bar{\epsilon} = \frac{1}{M}\sum_{i=1}^{M} \epsilon_i \tag{5.8}$$

$$\bar{c} = \frac{1}{M}\sum_{i=1}^{M} c_i \tag{5.9}$$

$$\bar{\phi} = \frac{1}{M}\sum_{i=1}^{M} \phi_i \tag{5.10}$$

Where M is the total number of sites on the lattice. Because ϵ_i, c_i, and ϕ_i and $\bar{\epsilon}$, $\bar{c}$, and $\bar{\phi}$ are functions of each other, equations 5.5–5.7 and 5.8–5.10 must be solved self-consistently. The process is as follows (illustrated in **Figure 5.3**):

1. Guess a value for the ensemble averages $\bar{\epsilon}$, $\bar{c}$, and $\bar{\phi}$.

2. Using these averages, solve equations 5.5–5.7 for each site on the lattice.

3. Calculate $\bar{\epsilon}_{\text{new}}$, $\bar{c}_{\text{new}}$, and $\bar{\phi}_{\text{new}}$ using equations 5.8–5.10 and the site populations from step 2.

4. If $\bar{\epsilon}_{\text{new}} = \bar{\epsilon}$ (and the same for c and ϕ), the process is complete. If not, return to step 2, using $\bar{\epsilon}_{\text{new}}$, $\bar{c}_{\text{new}}$, and $\bar{\phi}_{\text{new}}$ as the averages.

We have described the method using a lattice as this is the most intuitive way to understand it, however, in our simulations we solve the averages in equations 5.8–5.10 in an equivalent manner by integrating over the probability distribution, e.g.:

$$\bar{\epsilon} = \int \epsilon(k)P(k)dk \tag{5.11}$$

And similarly for $\bar{c}$ and $\bar{\phi}$. Here, $\epsilon(k)$ is equivalent to ϵ_i with $k = k_i$. Solving the equations this way removes reference to the original lattice, and thus it could refer to any lattice geometry that has 4 nearest neighbors.

We are ultimately interested in modeling the average behavior of the OLED, and thus only need $\bar{\epsilon}$, $\bar{c}$, and $\bar{\phi}$. We find that in our simulations, $\bar{\phi}$ is typically between 0.98 and 1.0, $\bar{c}$ is between 1×10^{-7} and 0.003, and $\bar{\epsilon}$ is between 1×10^{-9} and 0.02. Once we

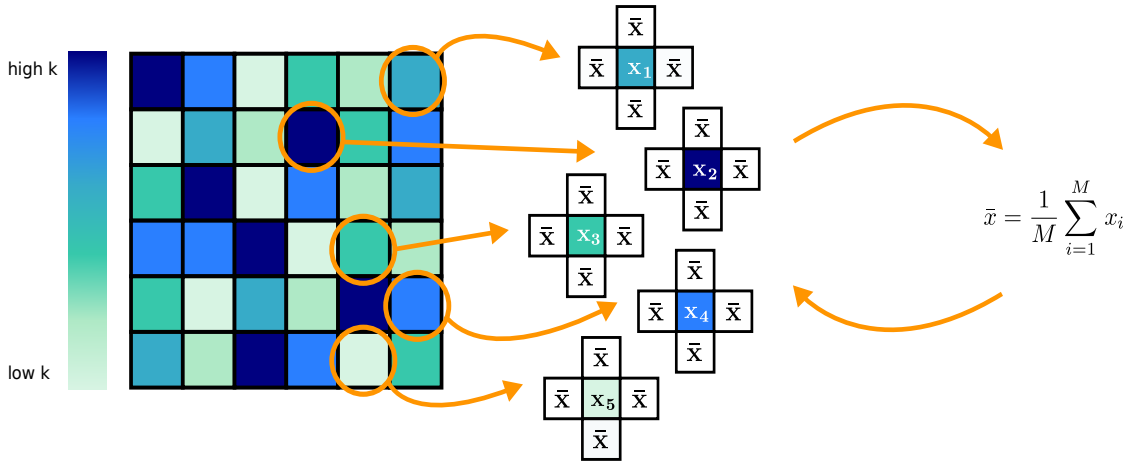

Figure 5.3: Illustration of the self-consistent field procedure. We start with a lattice (left), with an initial guess for the average population over the lattice, $\bar{x}$. We then calculate the population of x at each site (x_i), using the guess of $\bar{x}$ (center). Using the populations we calculate at each site, we compute the new average, $\bar{x}$ (right). This process is repeated until $\bar{x}$ does not change.

have obtained these quantities, we can use them to calculate the external quantum efficiency (EQE) and current density (j) of a device using the following equations:

$$\text{EQE} = \frac{\#\text{ photons emitted}}{\#\text{ charges injected}} = \frac{\#\text{ photons emitted/s}}{\#\text{ charges injected/s}} = \frac{\eta k_{\text{u}} \bar{\epsilon}}{k_{\text{ci}} \bar{\phi}} \tag{5.12}$$

$$j = \frac{\#\text{ charges injected/s}}{A} = \frac{k_{\text{ci}} \bar{\phi}}{A} \tag{5.13}$$

Where A refers to the area of a single lattice site. We have introduced η, the unimolecular quantum yield, which describes the fraction of unimolecular decay that is radiative, and also accounts for the outcoupling of the device. In order to simulate the EQE roll-off curve, we calculate the EQE for a range of current densities. We vary the current density by varying the charge injection rate constant, k_{ci}, between ~ 0.007 s^{-1} and 40,000 s^{-1}.

By replacing the charge injection step in Figure 5.2 with exciton injection (and $k_{\text{ci}}/k_{-\text{ci}}$ with $k_{\text{ei}}/k_{-\text{ei}}$), we can modify the above model to simulate photoluminsecence experiments instead of electroluminescence experiments. In this situation, exciton in-

jection arises from incident photon flux, and the rate of injection will be proportional to the light intensity. If we follow the steps presented above, we can calculate $\bar{\epsilon}$, $\bar{c}$, and $\bar{\phi}$ for a photoluminescence experiment, and use them to calculate the photoluminescence quantum yield (PLQY) and exciton density (ρ):

$$\text{PLQY} = \frac{\#\text{ photons emitted}}{\#\text{ photons absorbed}} = \frac{\#\text{ photons emitted/s}}{\#\text{ photons absorbed/s}} = \frac{\eta k_{\text{u}} \bar{\epsilon}}{k_{\text{ei}} \bar{\phi}} \tag{5.14}$$

$$\rho = \frac{\#\text{ photons absorbed/s}}{V} = \frac{k_{\text{ei}} \bar{\phi}}{V} \tag{5.15}$$

Where V refers to the volume of a single lattice site.

The relative PLQY (rel. PLQY) is then calculated by normalizing the PLQY:

$$\text{rel. PLQY}(\rho_i) = \frac{\text{PLQY}(\rho_i)}{\text{PLQY}(\rho_0)} \tag{5.16}$$

Where ρ_0 indicates the reference exciton density (typically calculated at the lowest value of k_{ei}), and ρ_i indicates the exciton density at the point under consideration. The graphs of relative PLQY vs exciton density can then be generated by calculating PLQY while varying the exciton injection rate constant, k_{ei}, between ~ 0.4 s^{-1} and 1,100 s^{-1}.

We can also calculate the average EEA and ECA fluxes:

$$F_{\text{EEA}} = k_{\text{EEA}}\ \bar{\epsilon}\ \bar{\epsilon} \tag{5.17}$$

$$F_{\text{ECA}} = k_{\text{ECA}}\ \bar{\epsilon}\ \bar{c} \tag{5.18}$$

Note that when there is disorder in one of these rate constants, the k value used corresponds to $\exp(\overline{\ln(k)})$. These expressions will prove useful in making quantitative arguments about the significance of these two processes in a given device.

5.3 Experimental Details

As illustrative examples of OLED roll-off, we fabricated two types of luminescent doped films. We choose the extensively studied thermally activated delayed fluorescence (TADF) emitter 2,4,5,6-tetra(9H-carbazol-9-yl)isophthalonitrile (4CzIPN).[159–161] We employ 4,4'-di(9H-carbazol-9-yl)-1,1'-biphenyl (CBP) and its brominated version, 4,4'-bis(3-bromo-9H-carbazol-9-yl)-1,1'-biphenyl (Br_2CBP) as host materials. The emitter molecule is doped into the two different host materials at 20 wt%. As we have previously shown, employing the brominated host Br_2CBP facilitates a selective enhancement of intersystem crossing (ISC) and reverse intersystem crossing (RISC) via the external heavy-atom effect, leading to shorter exciton lifetimes without significantly altering other properties of the films.[162] Therefore, these systems form an excellent single-variable control experiment: comparing the two devices involves changing only a single characteristic that is likely to significantly impact the mechanism of roll-off. Employing the model will help determine whether the change is large enough to influence the overall mechanism. In a purely photoluminescent experiment we measured the PLQY roll-off in response to increasing exciton density in the film. Moreover, we fabricated OLEDs using these two doped films as emissive layers. We measured the external quantum efficiency as function of current density.

5.4 Computational Details

In order to reproduce the experimental results, we need to determine the appropriate rate constants to use as parameters for our model. To do this, we employed a Nelder-Mead optimization, minimizing the difference between our model and the experimental EQE for all values of the current density (j):

$$\int |\mathrm{EQE}_{\mathrm{MFSS}}(j) - \mathrm{EQE}_{\mathrm{expt}}(j)| dj \tag{5.19}$$

The parameters we optimized were $k_{-\mathrm{ci}}$, k_{rec}, k_{u}, η, k_{EEA}, k_{ECA}, and σ^2 (the disorder in the heterogeneous rate constant). We fixed the backward charge recombination

rate constant, $k_{-\mathrm{rec}}$, to be 400 s^{-1} (several orders of magnitude lower than the other rate constants), as we expect this reaction to be much slower than the others due to the large binding energy of excitons in organic materials. We also fixed the box length, l, to be 1.0 nm for the CBP device and 1.65 nm for the Br_2CBP device, which has larger molecules in its emitting layer than the CBP device.

We optimized each device three times, once with disorder in the EEA rate, once with disorder in the ECA rate, and once with no disorder. The results of all of these fits, as well as the fit with disorder in k_{u}, are included in appendix C. We then chose the set of rate constants that gave the best overall fit. Once we had obtained the appropriate rate constants for the EQE curve, we validated our approach by using these parameters to predict the relative PLQY curve. For the same device, the rate constants for all processes except charge/exciton injection and leakage should remain the same between the two models. After successfully predicting the PLQY curve, we conducted an uncertainty analysis to estimate a margin of error for the parameters (see appendix C for details).

5.5 Results and Discussion

5.5.1 CBP Device

In Figure 5.4, we show the results of our model using the parameters given in **Table 5.1**, along with the experimental data for both EQE and PLQY roll-off of the CBP device. We found the best fit was obtained when considering disorder in the EEA rate. We emphasize that we were able to use the parameters obtained from fitting the EQE curve to predict the PLQY curve, suggesting these parameters are physically meaningful, given that the measurements are independent.

Overall, because our model is coarse-grained, it is difficult to compare the obtained rate constants to experiment; we do not expect exact agreement with the device parameters, but rather hope to be in the correct order of magnitude range of measured rates. We can convert our normalized EEA and ECA rate constants to the

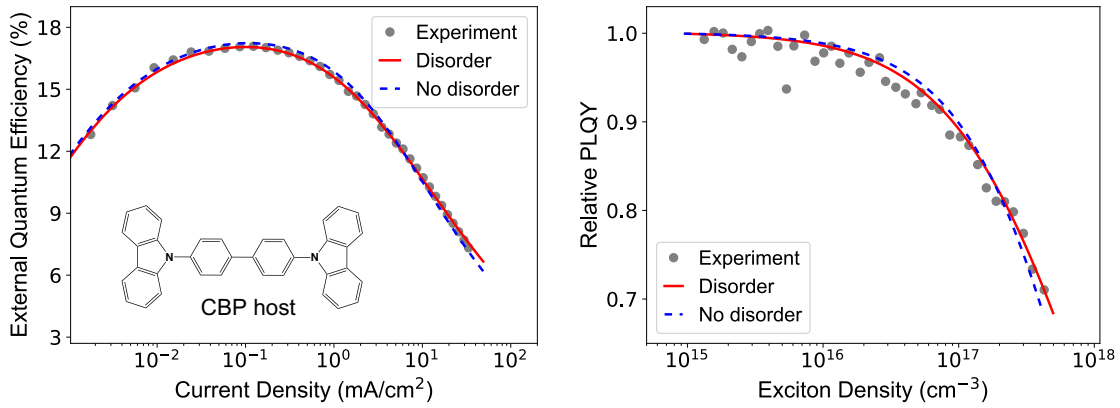

Figure 5.4: Results for the CBP device. Gray dots indicate experimental data, the red line is the MFSS model with disorder in the EEA rate constant, and the blue dashed line is the MFSS model with no disorder. Left: External quantum efficiency vs current density roll-off curve. Right: Relative photoluminescence quantum yield vs exciton density roll-off curve. Inset: the CBP host molecule.

Parameter	Disorder in EEA	No disorder
$k_{-\mathrm{ci}}$	$8.5426(9) \times 10^3$	$8.543(1) \times 10^3$
k_{rec}	$6.543(2) \times 10^8$	$6.733(2) \times 10^8$
k_{u}	$3.9(1) \times 10^5$	$3.89(9) \times 10^5$
k_{EEA}	$7.3(4) \times 10^7$	$1.05(5) \times 10^8$
k_{ECA}	$8.5(3) \times 10^7$	$8.0(2) \times 10^7$
σ^2_{EEA}	846	0
η	0.3714	0.3740

Table 5.1: Parameters used to model the CBP device. All rate constants are in units of s^{-1}, σ^2 is in units of meV^2, and η is unitless. Parentheses indicate the uncertainty in the last digit.

experimental units of cm^3/s by multiplying the values in Table 5.1 by the lattice site volume; both rate constants are then on the order of 10^{-14} cm^3/s, which is consistent with previously reported values of $10^{-12} - 10^{-16}$ cm^3/s for EEA[87,88,90,94,163,164] and $10^{-11} - 10^{-13}$ cm^3/s for ECA.[88,91,92] The unimolecular rate constant has contributions from radiative and non-radiative decay, as well as intersystem crossing and reverse intersystem crossing. Because it is an amalgamation of different rates, it should not be interpreted as a precise proxy for exciton lifetime. Typically the non-radiative decay is the slowest unimolecular process, on the order of 10^5 s^{-1}[90] (compared to $10^6 - 10^7$ s^{-1} for the other processes[90,162]), which is the same order of magnitude

that we find for our unimolecular decay. It is difficult to compare our unimolecular quantum yield, η, to an experimental value, as experimental quantum yields measure the fraction of all decay that is radiative, rather than the fraction of unimolecular decay.

When considering the MFSS model without disorder, most of the parameters change only slightly compared to the optimal fit. The largest change is in the EEA rate constant, which can be explained by considering that the original parameter was an average. Because of the disorder, many sites had a higher rate constant, and the increase in k_{EEA} could indicate that these high-rate constant sites play a more important role. Figure 5.4 shows that, while including disorder slightly improves the agreement with experiment, we are still able to get good agreement without considering disorder. In appendix C we report the fit with disorder in the ECA rate, which we again find to be not quite as good as the optimal fit, but still in good agreement with experiment. This is perhaps to be expected, since our model treats each lattice site as an average over the depth of the emitting layer, effectively smoothing out much of the single-emitter heterogeneity. Since the model gives good results when considering disorder in EEA, ECA, as well as when neglecting disorder, this suggests that including disorder is not essential to reproducing the experimental result in this case.

Using the optimal parameters (i.e., including the effect of disorder), we calculate the ratio between the EEA and ECA fluxes (**Figure 5.5**). The exciton-exciton annihilation flux is about 1.5-2 times as large as the exciton-charge annihilation flux at the higher current densities relevant to roll-off (e.g. 10 mA/cm^2), and thus appears to be the dominant mechanism in this device.

5.5.2 Br_2CBP Device

In Figure 5.6, we show the results of our model for the Br_2CBP device using the parameters given in **Table 5.2**, along with the experimental data for both EQE and PLQY roll-off. Here, we find that the best fit is obtained when considering disorder in the ECA rate. All parameters are on the same order of magnitude as those for

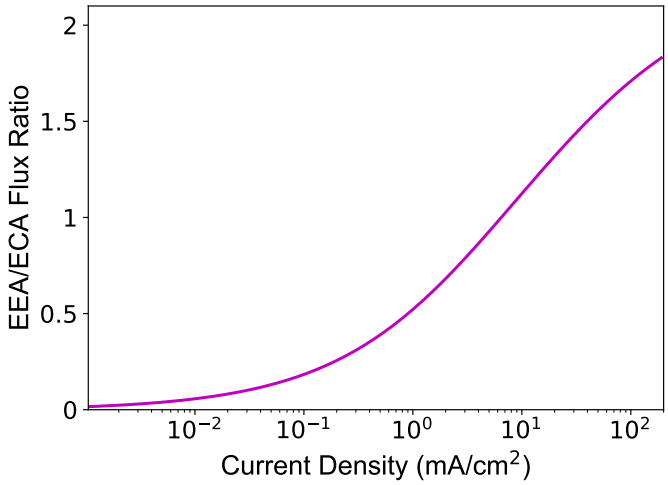

Figure 5.5: Ratio of the exciton-exciton annihilation flux to exciton-charge annihilation flux in the CBP device, with disorder in the EEA rate. The ratio exceeds 1 in the high current-density regime where roll-off occurs, indicating that the EEA flux is larger than the ECA flux in this regime. This suggests that EEA is the dominant mechanism in this device.

the CBP device, as we would expect. Notably, the EEA rate constant has decreased. It is not necessarily intuitive that this rate constant should change between the two devices. However, the increased spin-orbit coupling in the Br_2CBP device will affect the spin of the excitons in our system. Because EEA is a spin-dependent process, we expect that this will subsequently cause a change in the EEA rate constant.

Parameter	Disorder in ECA	No disorder
$k_{-\mathrm{ci}}$	$4.6752(1) \times 10^3$	$4.00046(8) \times 10^3$
k_{rec}	$4.6115(2) \times 10^8$	$4.4413(2) \times 10^8$
k_{u}	$3.64(1) \times 10^5$	$4.01(1) \times 10^5$
k_{EEA}	$1.136(8) \times 10^7$	$1.187(8) \times 10^7$
k_{ECA}	$6.72(2) \times 10^7$	$7.62(2) \times 10^7$
σ^2_{ECA}	641	0
η	0.3860	0.3719

Table 5.2: Parameters used for the Br_2CBP device. All rate constants are in units of s^{-1}, σ^2 is in units of meV^2, and η is unitless. Parentheses indicate the uncertainty in the last digit.

We note that the model and experiment diverge for high current densities. There are several reports in the literature of an apparent dependence of the exciton-exciton

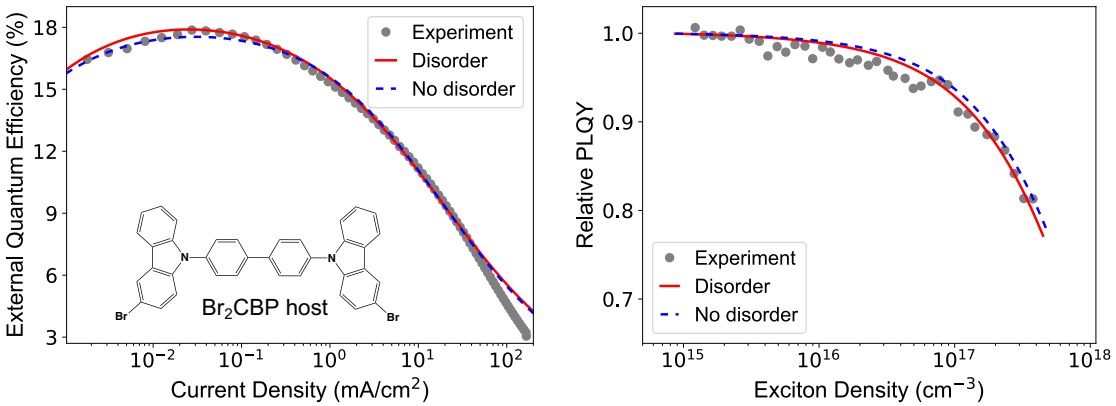

Figure 5.6: Results for the Br_2CBP device. Gray dots indicate experimental data, the red line is the MFSS model with disorder in the ECA rate constant, and the blue dashed line is the MFSS model with no disorder. Left: External quantum efficiency vs current density roll-off curve. Right: Relative photoluminescence quantum yield vs exciton density roll-off curve. Inset: the Br_2CBP host molecule.

annihilation and exciton-charge annihilation rate constants on exciton and charge density, respectively, which is typically attributed to a more complicated mechanism than the simple nearest-neighbor mechanism presented above.[96,158,165] Our disagreement at high current density may indicate that the nearest-neighbor mechanism is insufficient to fully describe the roll-off in this regime, although it could also be due to other causes, such as Joule heating or electric field effects.[72] There is also disagreement between the model and experiment at low current densities, which we attribute to charge carrier imbalance. While we assume perfect charge balance, in reality, OLEDs often suffer from charge imbalance at low current densities, which is believed to cause the initial increase in EQE.[72,164] In our model, we find that charge leakage ($k_{-\mathrm{ci}}$) is responsible for this initial increase, but this could be effectively accounting for some of the effects of charge imbalance that we neglect. We expect that a more elaborate kinetic model that treats electrons and holes as separate species would correct this disagreement.

Looking at Figure 5.6, we again find that, while including disorder improves the agreement between the simulated roll-off curve and the experimental curve (especially for the PLQY curve), we are still able to get good agreement without including the

effects of disorder. In addition, we are able to get good agreement when considering disorder in the EEA rate constant (reported in the appendix C). This further suggests that heterogeneity in the EEA and ECA rates is not essential to describing roll-off in this case.

Using the optimal parameters with disorder, we calculate the ratio between the EEA and ECA fluxes (**Figure 5.7**). In contrast to the CBP device, ECA appears to be the dominant mechanism here, as its flux is about 1.5-2 times as large as the EEA flux in the roll-off regime. This is perhaps not surprising, as the Br_2CBP device has been shown experimentally to have a shorter exciton lifetime than the CBP device,[162] which would make exciton-exciton annihilation less likely. In addition, while the two devices have similar EQE roll-off behavior, the Br_2CBP device has a less pronounced PLQY roll-off, which is consistent with ECA dominating over EEA, as excitons are much more prevalent than charges in that measurement.

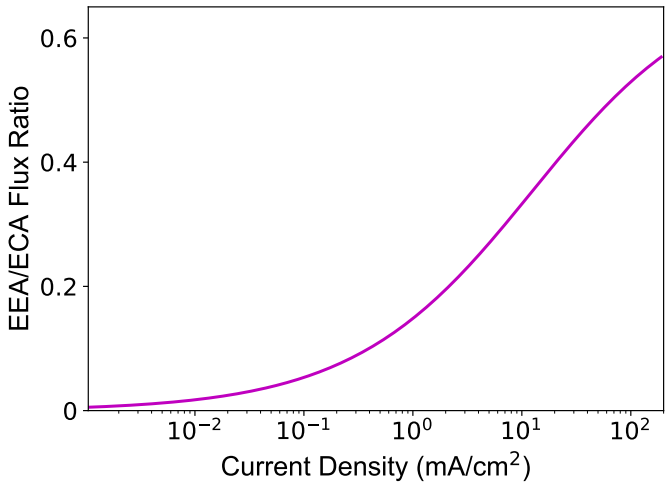

Figure 5.7: Ratio of the exciton-exciton annihilation flux to exciton-charge annihilation flux in the Br_2CBP device, with disorder in the ECA rate. The ratio remains below 1, indicating that the ECA flux is larger than the EEA flux even at high current densities. This suggests that ECA is the dominant mechanism in this device.

5.6 Conclusions

We have built a simple, physically-motivated model of OLED roll-off, which is able to directly translate macroscopic EL and PL measurements into microscopic rates and mechanisms. The model is able to account for all the key molecular processes as well as variation in the rates of these processes from one emitter to the next. By applying this model to two similar devices, differing only in the host material for the emitting layer, we find that in the first device, a 20% 4CzIPN:CBP OLED, exciton-exciton annihilation is the dominant roll-off mechanism, while in the second device, a 20% 4CzIPN:Br_2CBP OLED, exciton-charge annihilation is the dominant mechanism. We are able to directly tie this difference to the external heavy-atom effect in the latter device and its ability to accelerate emission. Our results suggest that OLED roll-off mechanisms are device dependent, and that tuning the emitting layer of an OLED can affect the roll-off mechanism.

A simple, fast model like ours has enormous potential to guide rational design of OLED emitting layers and devices. It can make quantitative predictions about roll-off mechanisms in a fraction of the time of kinetic Monte Carlo, using only the commonly measured EQE and PLQY roll-off curves, and without requiring any further material-specific parameters. This will allow the model to be applied broadly to many devices, which is essential when considering the multitude of different types of OLEDs that have been developed.

Future work will focus on modeling more devices, with the goal of identifying roll-off mechanisms in order to guide rational design and improve device performance. We are also interested in building degradation into our model, to investigate OLED stability.

Appendix A

Supplementary Information for Chapter 2

A.1 Structural Analysis

To perform the structural analysis and identify undercoordinated atoms, we first plotted a histogram of Cd-Se and Cd-ligand distances. We used this histogram to identify a cutoff for which atoms should be considered "bonded," which varies slightly based on the system in question (3.0 Å for the $Cd_{33}Se_{33}$ and $Cd_{38}Se_{38}$ systems, and 3.3 Å for the $Cd_{91}Se_{91}$ system). Once an appropriate cutoff has been selected, we count the number of atoms that each Cd and Se atom is bonded to. For Se, we consider only Cd's to be "bonded," while Cd can be bonded to either an Se or the attaching atom of the ligand (e.g. N for $MeNH_2$). Any atom that is bonded to 2 or fewer other atoms is considered "undercoordinated."

After identifying any undercoordinated atoms, we used the excited state Löwdin charges to determine if these undercoordinated atoms played a role in creating surface traps. We sum the fraction of charge on the undercoordinated atoms for each excitation, and compare this charge to the amount of charge we would expect to be on each atom if the electron and hole were uniformly distributed over all of the atoms. We then plot the charge fraction of the electron and the hole on undercoordinated atoms, for each excitation.

In Supplementary Figure A.1, we show the histogram of Cd-Se and Cd-ligand distances for the $Cd_{91}Se_{91}$ NC with methylamine ligands. For this system, we chose a cutoff of 3.3 Å, and we find that there are 8 undercoordinated Se atoms and no undercoordinated Cd atoms.

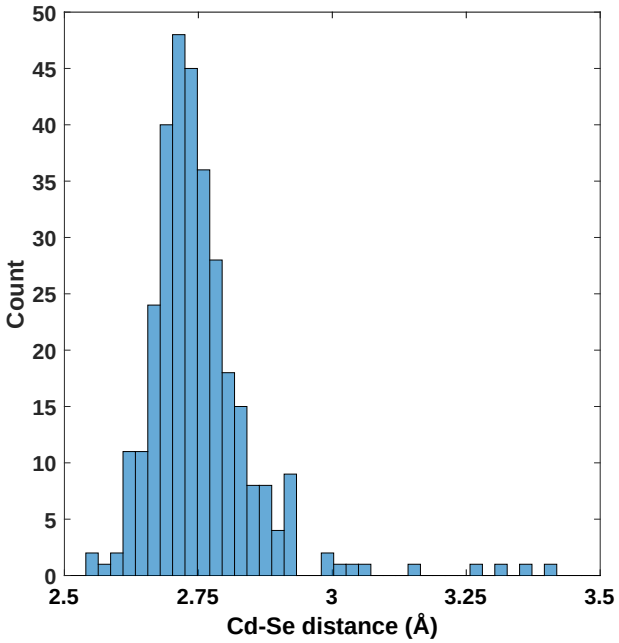

Figure A.1: Histogram of Cd-Se distances in the $Cd_{91}Se_{91}$ NC with $MeNH_2$ ligands.

We plot the charge analysis of the hole/electron on the undercoordinated Se atoms in Fig. 4 of the main text and Supplementary Figure A.2, respectively. For the hole charge analysis, we find that the low-energy excitations $E_{\text{ex}} < 2.95$ eV have up to 86% of the charge from the excited hole on the undercoordinated Se atoms, with 45% of these states having $60-86\%$ of the hole charge located on the undercoordinated Se atoms. Even for higher energy excitations $E_{\text{ex}} > 2.95$ eV, these undercoordinated atoms have a disproportionate amount of charge. 21% of these states have $60-86\%$ of the charge on the undercoordinated Se, and 15% of the states have $40-60\%$ of the charge on them. This is much higher charge than would be expected from a uniform distribution of charge.

For the electron charge analysis, we find that the low-energy excitations $E_{ex} < 2.95$

eV have up to 83% of the charge from the excited electron on the undercoordinated Se atoms. Unlike the hole charge, the excited electron has only 13% of states with $60-83\%$ of the electron charge located on the undercoordinated Se atoms. For higher energy excitations $E_{ex} > 2.95$ eV, these undercoordinated Se atoms have 3% of states with $60-83\%$ of charge on them. The percentage of states with high electron charge on the undercoordinated Se is generally low, but we wouldn't expect the electron to localize on undercoordinated Se atoms at all.

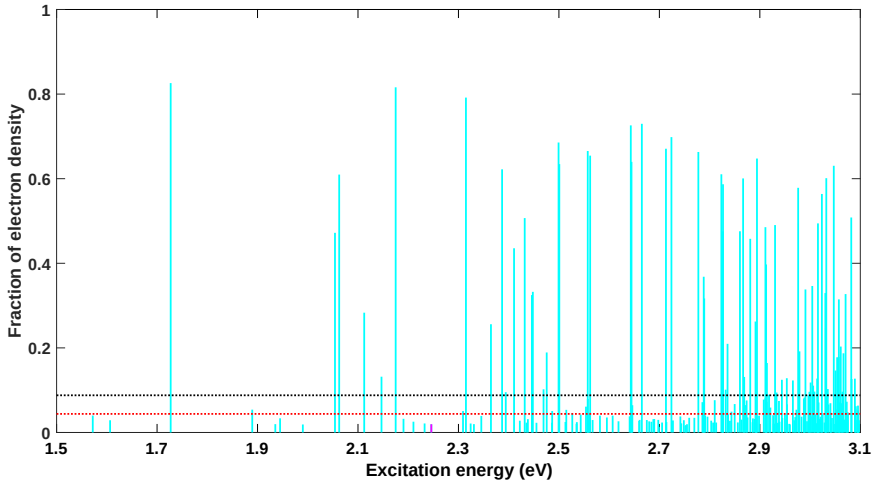

Figure A.2: Fraction of electron density on 2-coordinate Se atoms in $Cd_{91}Se_{91}$ with methylamine ligands. The magenta peak corresponds to excitation #16 (see main text Fig. 4). The red dashed line indicates the expected fraction on the 2-coordinate Se atoms if the density were evenly distributed across all Cd and Se atoms, and the black dashed line indicates the expected fraction on the 2-coordinate Se atoms if the density were evenly distributed across all Se atoms.

When decreasing the cutoff to 3.1 Å which roughly corresponds to the first peak of Cd-Se distances, there is 1 undercoordinated Cd atoms, and the number of Se atoms remains the same. There is no appreciable electron charge located on the undercoordinated Cd atom. For the hole charge there is some charge localized on this undercoordinated Cd atom but its magnitude is small and thus its effect is not pronounced.

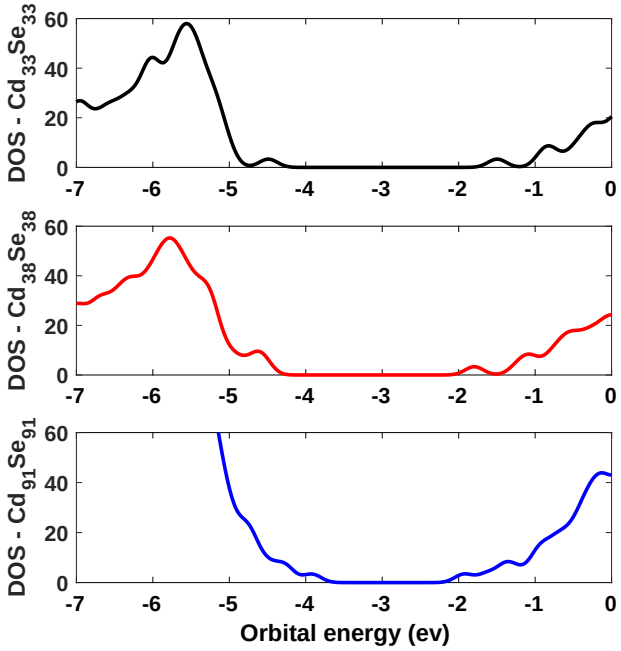

Figure A.3: Orbital density of states for $Cd_{33}Se_{33}$ (top), $Cd_{38}Se_{38}$ (middle), $Cd_{91}Se_{91}$ (bottom) with methylamine ligands, using the standard LANL2DZ basis set

A.2 Band structure

We calculated the orbital density of states (DOS) for $Cd_{33}Se_{33}$, $Cd_{38}Se_{38}$, and $Cd_{91}Se_{91}$ with methylamine ligands. The band structures were calculated from the orbital energies, applying Gaussian broadening of $\sigma = 0.12$ eV. The plots are presented in Supplementary Figure A.3. One can see that as the NC size increases the HOMO-LUMO gap decreases, as expected from the particle in a sphere model. For the smallest NC ($Cd_{33}Se_{33}$) the HOMO and LUMO orbitals are separated from the more denser DOS of the occupied and virtual orbitals; as the size increases there are more orbitals close to the HOMO and LUMO orbitals, and the separation of the HOMO and LUMO from the denser part of the DOS is less clear.

We also calculated the DOS for the $Cd_{38}Se_{38}$ NC with Me_3PO ligands and no ligands, which are compared with $Cd_{38}Se_{38}$ with methylamine ligands in Supplementary Figure A.4.

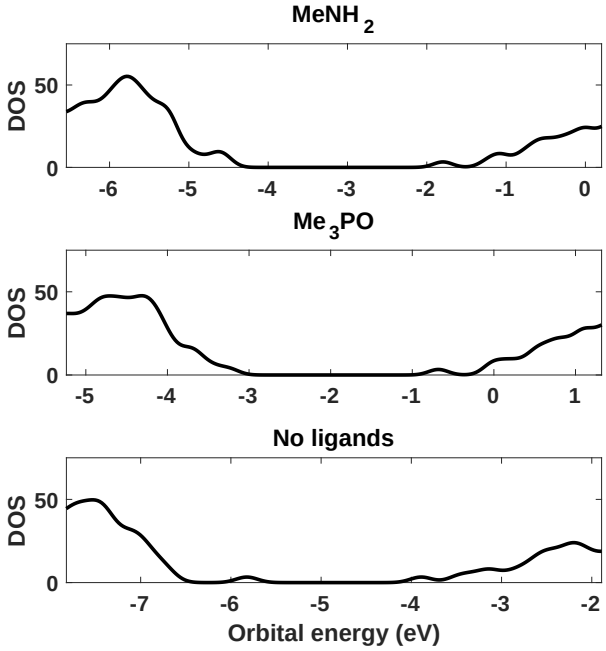

Figure A.4: Orbital density of states for $Cd_{38}Se_{38}$ with methylamine ligands (top), Me_3PO ligands (middle), and no ligands (bottom).

A.3 Basis set comparison

In order to ensure that our results were not an artifact of the basis set used, we also conducted TDDFT calculations on the $Cd_{38}Se_{38}$ NC using a larger basis set on the ligands. In Supplementary Figure A.5, we show the orbital density of states with the standard LANL2DZ basis set used in the main text, as well as with LANL2DZ on the Cd and Se and 6-31G* on the ligands. The two are nearly indistinguishable, with a slight shift down in energy upon enlarging the basis set, on average 0.068 eV for the occupied orbitals. The HOMO-LUMO gaps are also in good agreement, with the larger basis set having a gap of just 0.054 eV smaller than the LANL2DZ basis. In Supplementary Figure A.6, we show the absorption spectrum and density of transitions with the two basis sets. Due to computational limitations, we were only able to calculate 150 excitations using the larger basis set. The two spectra and densities of transitions are nearly identical, with a small redshift in the 6-31G* results, consistent with the smaller HOMO-LUMO gap.

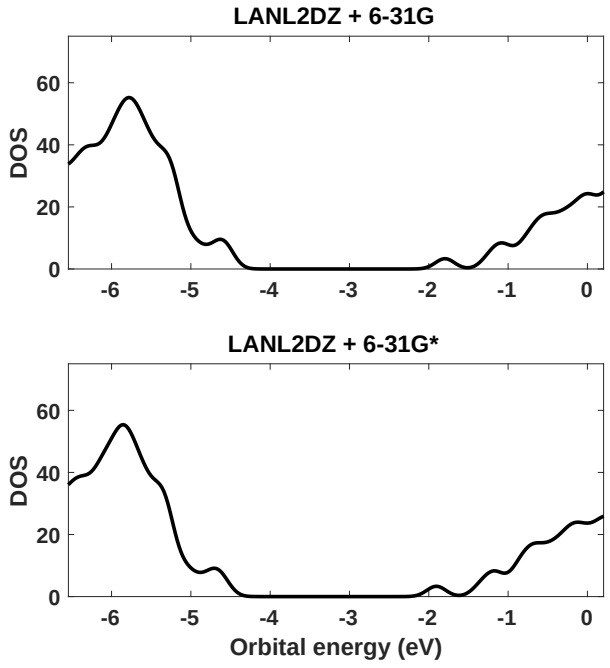

Figure A.5: Orbital density of states for $Cd_{38}Se_{38}$ with methylamine ligands, using the standard LANL2DZ (top), and LANL2DZ on the Cd and Se with 6-31G* on the ligands (bottom).

In Supplementary Figure A.7, we show the IPR for the LANL2DZ and 6-31G* results. We find that they again are nearly identical, indicating that the character of the excitations (surface vs bulk) is not changed by the basis set. In Supplementary Figure A.8-A.9, we show the attach and detach densities for representative surface-to-bulk and bulk-to-bulk excitations with the two basis sets. We find that not only is the surface vs bulk character of the excitation unaffected, but visually the excitations look identical across the two basis sets.

We therefore conclude that the results in the LANL2DZ basis are sufficient, and since the 6-31G* basis is significantly more computationally expensive (and too expensive to use on the $Cd_{91}Se_{91}$ NC), we use the LANL2DZ basis for the analysis in the main text.

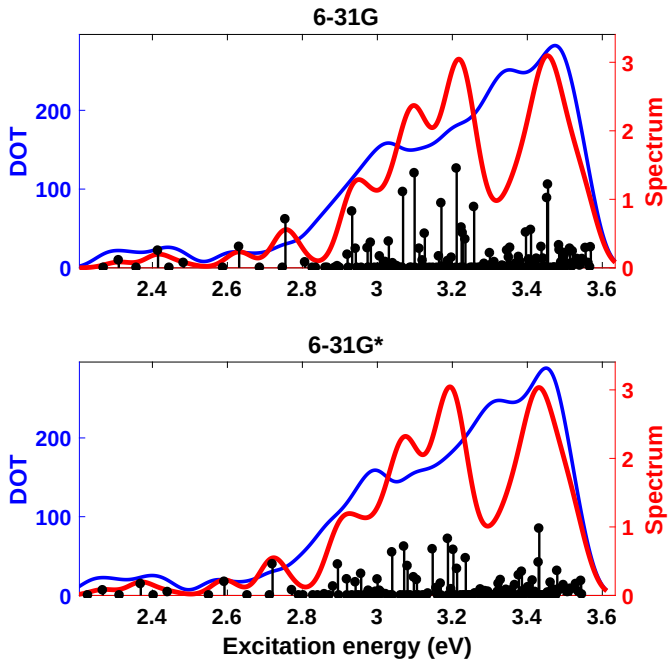

Figure A.6: (Top) Spectrum (red) and density of transitions (blue) for the first 75 singlet excitations and first 75 triplet excitations of $Cd_{38}Se_{38}$ with methylamine ligands, using the standard LANL2DZ basis set. (Bottom) Spectrum (red) and density of transitions (blue) for the first 75 singlet excitations and first 75 triplet excitations of $Cd_{38}Se_{38}$ with methylamine ligands, using the LANL2DZ ECP for the Cd and Se atoms, but the 6-31G* basis set for the ligands.

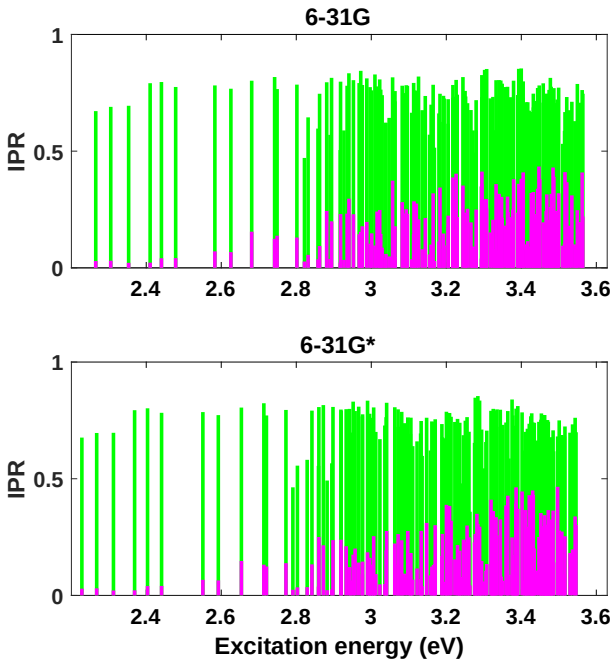

Figure A.7: (Top) IPR for the electron (green) and hole (magenta) for the first 75 singlet excitations and first 75 triplet excitations of $Cd_{38}Se_{38}$ with methylamine ligands, using the standard LANL2DZ basis set. (Bottom) IPR for the electron (green) and hole (magenta) for for the first 75 singlet excitations and first 75 triplet excitations of $Cd_{38}Se_{38}$ with methylamine ligands, using the LANL2DZ ECP for the Cd and Se atoms, but the 6-31G* basis set for the ligands.

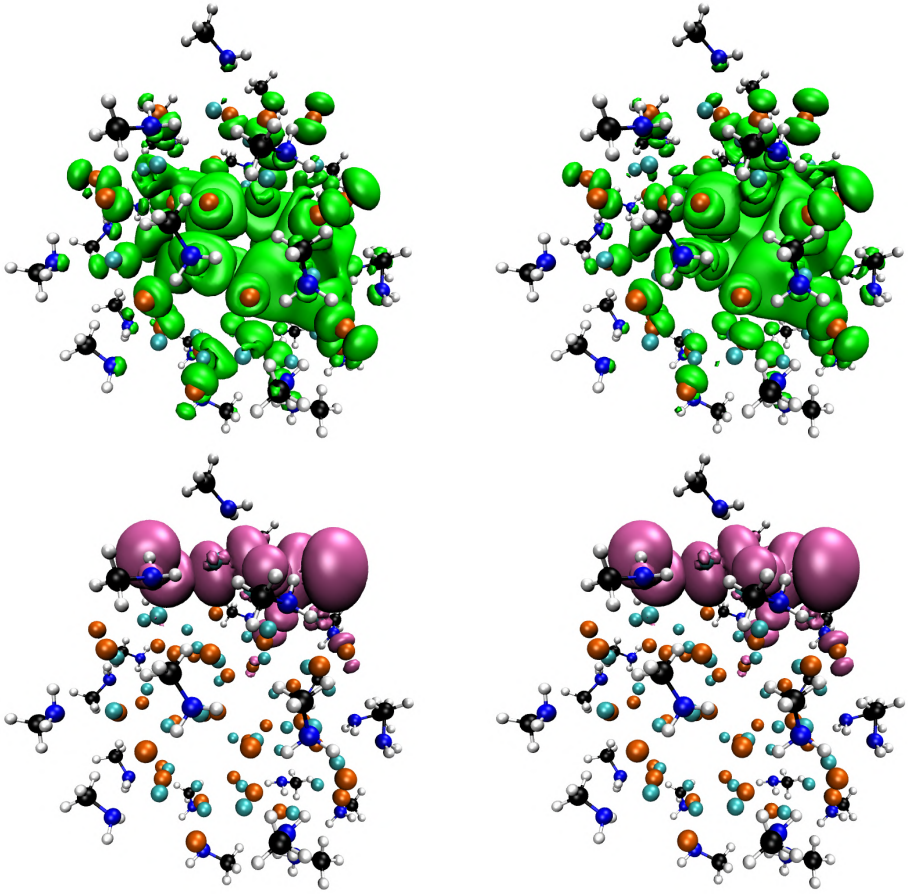

Figure A.8: Attach (top) and detach (bottom) densities of the first singlet excitation for $Cd_{38}Se_{38}$ with methylamine ligands with standard LANL2DZ (left) and LANL2DZ ECP for the Cd and Se atoms, but the 6-31G* basis set for the ligands (right).

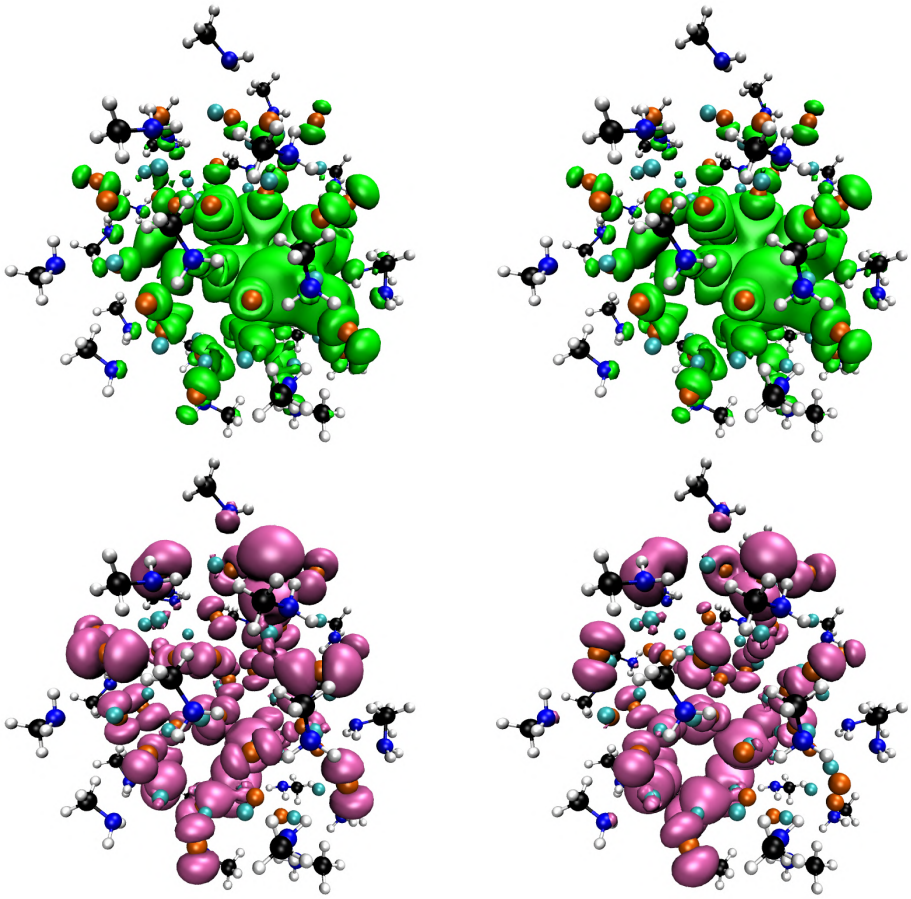

Figure A.9: Attach (top) and detach (bottom) densities of the brightest excitation in the main peak for $Cd_{38}Se_{38}$ with methylamine ligands with standard LANL2DZ (left) and LANL2DZ ECP for the Cd and Se atoms, but the 6-31G* basis set for the ligands (right).

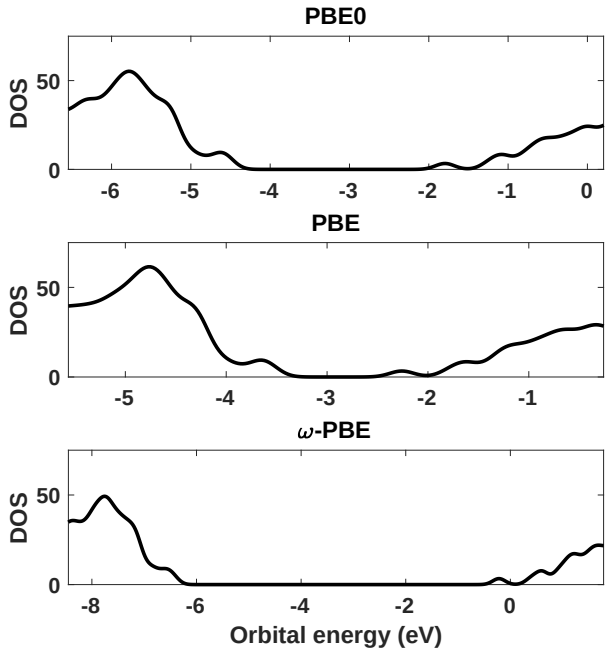

Figure A.10: Orbital density of states for $Cd_{38}Se_{38}$ with methylamine ligands, using the PBE0 functional (top), PBE functional (center), and ω-PBE functional (bottom).

A.4 Functional comparison

We selected the PBE0 functional as it is a hybrid functional which incorporates a fraction of exact exchange, which has been shown to be important for correctly treating the electron-hole interaction in excitonic systems. In order to ensure that our results are not an artifact of the functional chosen, we also conducted TDDFT calculations on the $Cd_{38}Se_{38}$ NC using PBE and ω-PBE. Due to computational limitations, we could only calculate 150 excitations.

In Supplementary Figure A.10 we compare the orbital density of states using PBE, PBE0, and ω-PBE. We find that, as expected, PBE has the smallest band gap, PBE0 has a larger band gap, and ω-PBE has the largest band gap. Other than the size of the band gap, qualitatively, all three functionals produce nearly identical orbital density of states.

In Supplementary Figure A.11 we compare the density of transitions and absorp-

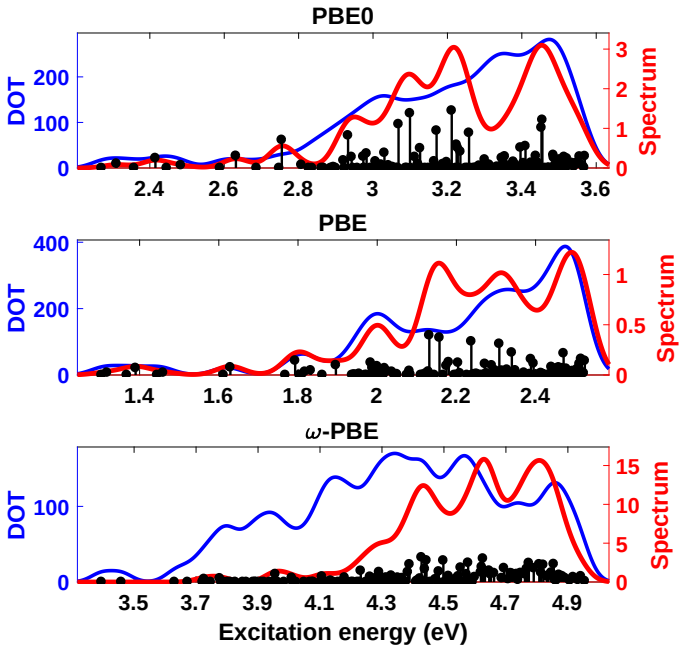

Figure A.11: Spectrum (red) and density of transitions (blue) for the first 75 singlet excitations and first 75 triplet excitations of $Cd_{38}Se_{38}$ with methylamine ligands, using the PBE0 functional (top), PBE functional (center), and ω-PBE functional (bottom).

tion spectrum using PBE, PBE0, and ω-PBE. As we would expect from the shifted band gaps, the excitation energies are quite different between the three functionals. We find that all three functionals produce qualitatively similar absorption spectra, with a long tail of dark states, followed by a small side peak, then 3 main bright peaks. PBE and PBE0 show qualitatively similar densities of transitions, while ω-PBE's density of transitions is different due to its asymmetric affect on singlets and triplets.

In Supplementary Figure A.12 we show the charge analysis and IPR for all 3 functionals, and in Supplementary Figure A.13-A.14 we show the attach and detach densities for representative surface-to-bulk and bulk-to-bulk excitations with the three different functionals.

The PBE and PBE0 functionals show very similar results, with low-energy excitations being surface to bulk transitions, and higher-energy excitations being a mix

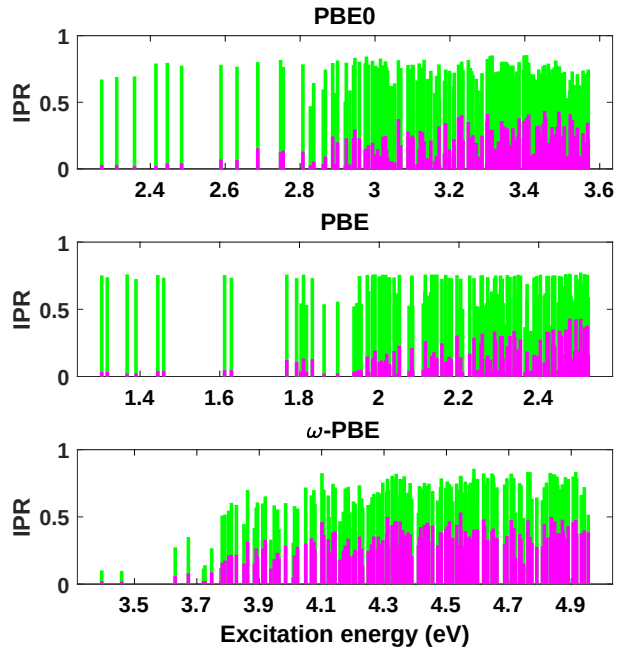

Figure A.12: IPR for the electron (green) and hole (magenta) for the first 75 singlet excitations and first 75 triplet excitations of $Cd_{38}Se_{38}$ with methylamine ligands, using the PBE0 functional (top), PBE functional (center), and ω-PBE functional (bottom).

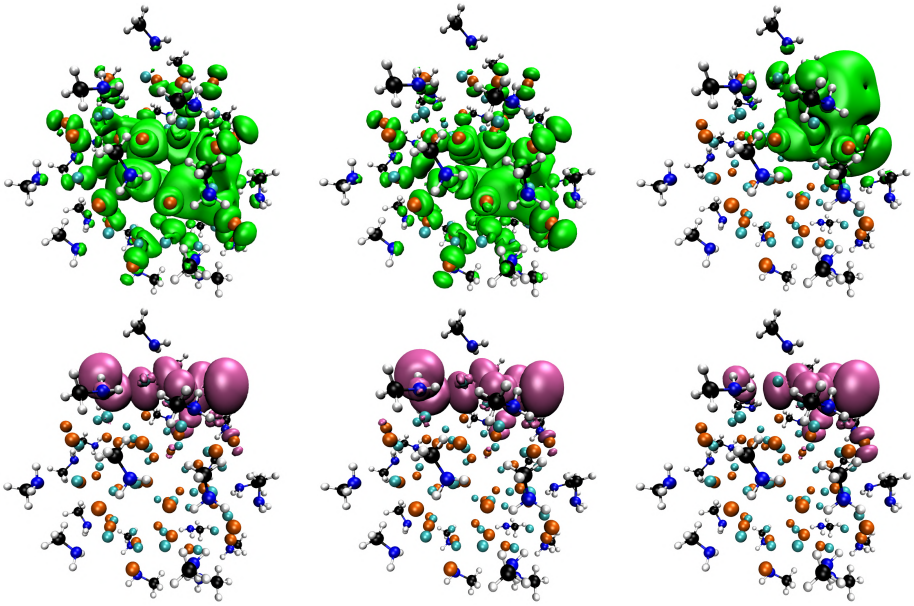

Figure A.13: Attach (top) and detach (bottom) densities of the first singlet excitation for the $Cd_{38}Se_{38}$ NC with PBE0 (left), PBE (center), and ω-PBE (right)

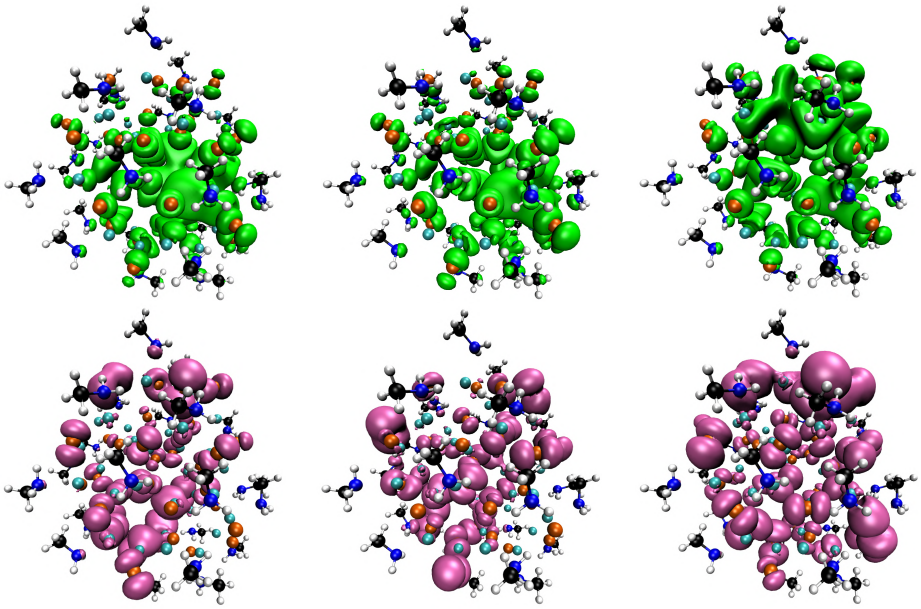

Figure A.14: Attach (top) and detach (bottom) densities of the brightest excitation from the center peak for the $Cd_{38}Se_{38}$ NC with PBE0 (left), PBE (center), and ω-PBE (right)

of surface to bulk and bulk to bulk transitions. Comparing the attach and detach densities between PBE and PBE0, we also see that the lower energy PBE excitations are indeed surface to bulk transitions that appear visually identical to the PBE0 excitations. However, in general, the higher energy “delocalized" or “bulk" holes in the PBE calculation appear to be more localized than in the PBE0 calculation, which can also be seen from their lower IPR values.

Comparing PBE0 and ω-PBE, we see from both the IPR and the attach densities that the low-energy electrons are significantly more localized than in the PBE0 calculation, and we see the appearance of surface to surface transitions that were not present in the PBE0 calculation. We also see that the higher energy holes are more delocalized than in PBE0. Despite these differences, the qualitative result remains that the low energy states are localized surface states and the higher energy states are a mixture of surface and bulk excitations.

Because our results are not sensitive to the functional used, we will conduct our simulations in the main text with PBE0, which is more computationally affordable

than ω-PBE.

A.5 Attach/detach densities with different ligands

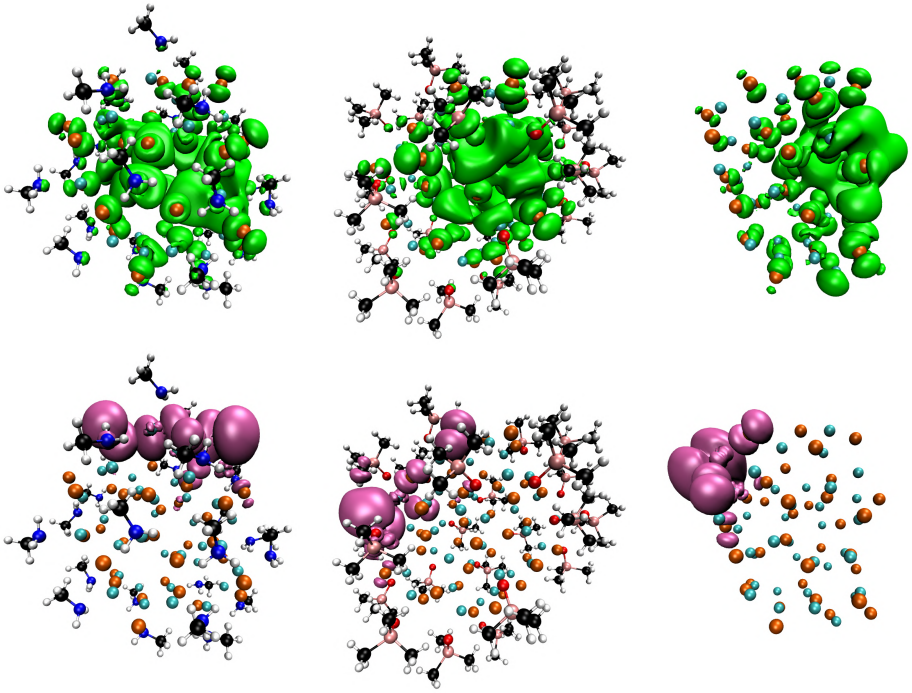

Figure A.15: Attach (top) and detach (bottom) densities of the first singlet excitation for the $Cd_{38}Se_{38}$ NC with methylamine ligands (left), Me_3PO ligands (center), and no ligands (right).

A.6 Reduced excitation space for $Cd_{91}Se_{91}$

For the TDDFT calculations on $Cd_{91}Se_{91}$, 500 core orbitals were frozen to allow a larger number of excitations to be calculated.

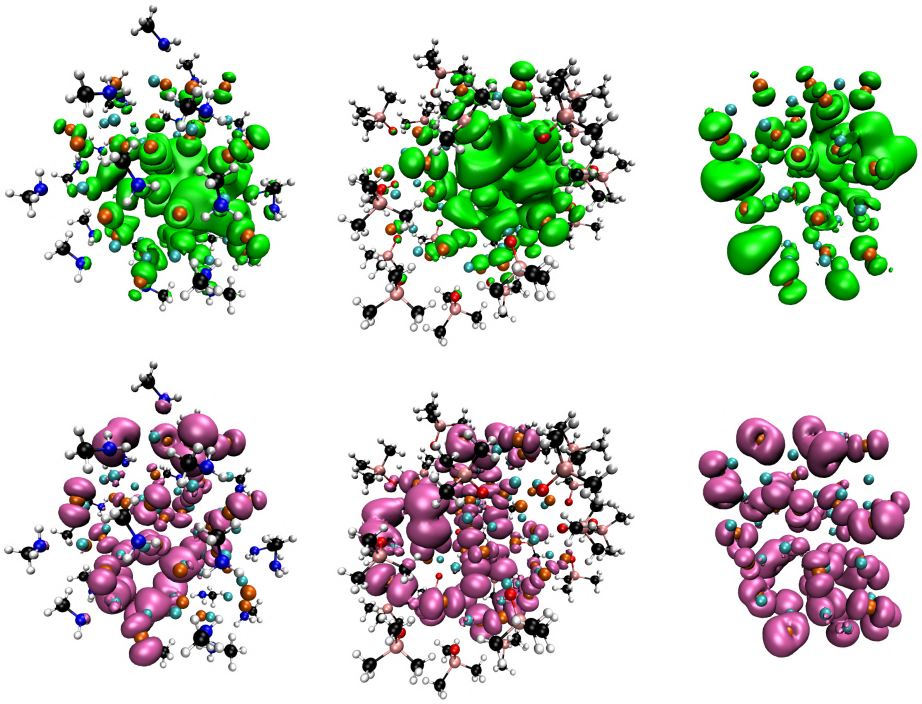

Figure A.16: Attach (top) and detach (bottom) densities of the brightest overall excitation for $Cd_{38}Se_{38}$ with methylamine ligands (left), Me_3PO ligands (center), and no ligands (right)

Appendix B

Supplementary Information for Chapter 3

B.1 Cd-Se distance cumulative distribution functions over the course of the optimization

The figures below show the cumulative distribution of bond distances for each system over the course of the optimization.

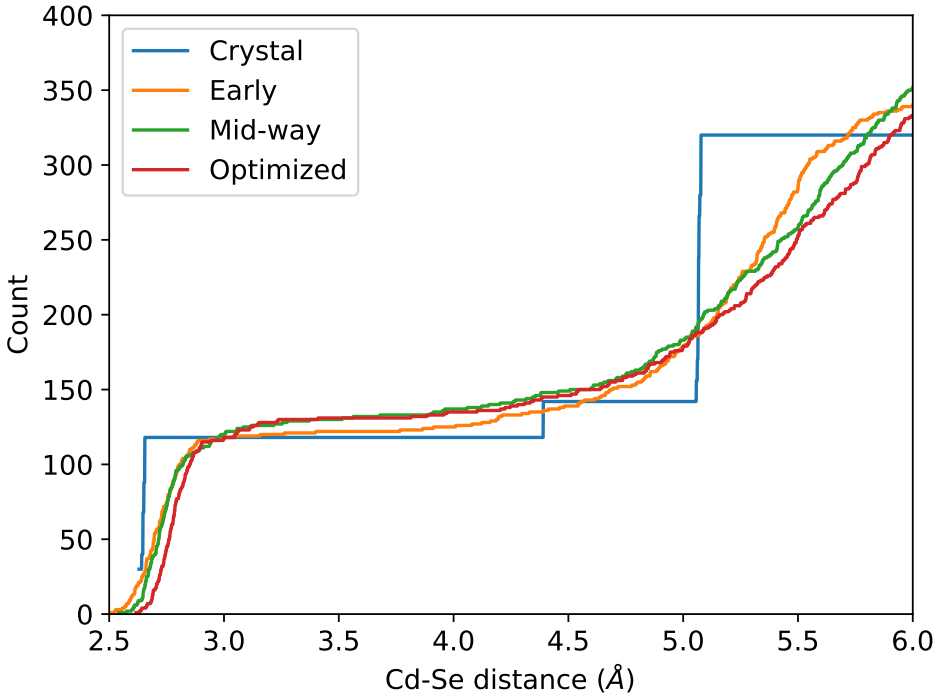

Figure B.1: Evolution of the cumulative distribution of bond lengths in $Cd_{38}Se_{38}$ with $MeNH_2$ during geometry optimization. The blue line is the crystal structure before optimization, the orange line is early in the optimization (31 meV per atom from the optimized structure), the green line is mid-way through the optimization (5 meV per atom from the optimized structure), and the red line is the optimized structure.

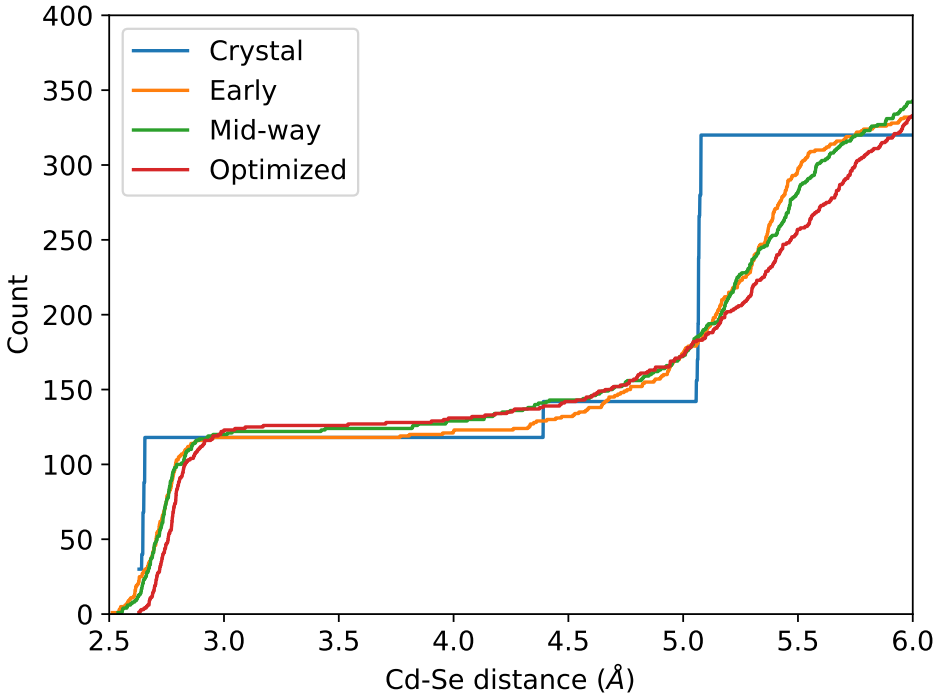

Figure B.2: Evolution of the cumulative distribution of bond lengths in $Cd_{38}Se_{38}$ with Me_3PO during geometry optimization. The blue line is the crystal structure before optimization, the orange line is early in the optimization (37 meV per atom from the optimized structure), the green line is mid-way through the optimization (3 meV per atom from the optimized structure), and the red line is the optimized structure.

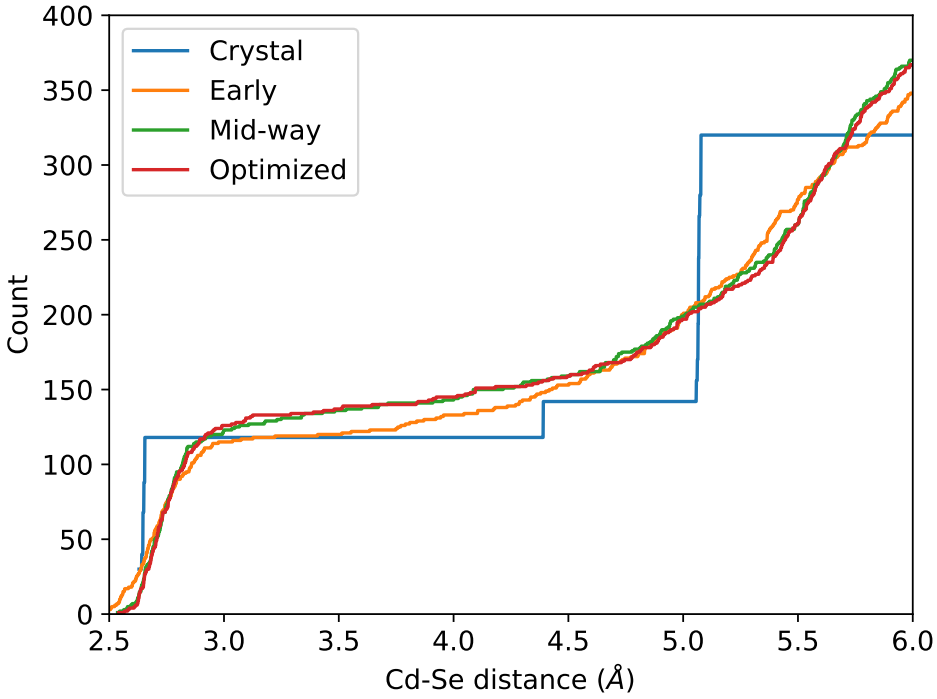

Figure B.3: Evolution of the cumulative distribution of bond lengths in $Cd_{38}Se_{38}$ with no ligands during geometry optimization. The blue line is the crystal structure before optimization, the orange line is early in the optimization (93 meV per atom from the optimized structure), the green line is mid-way through the optimization (7.5 meV per atom from the optimized structure), and the red line is the optimized structure.

B.2 Band structure

The following figures contain the band structure at several points over the course of the optimization for all structures.

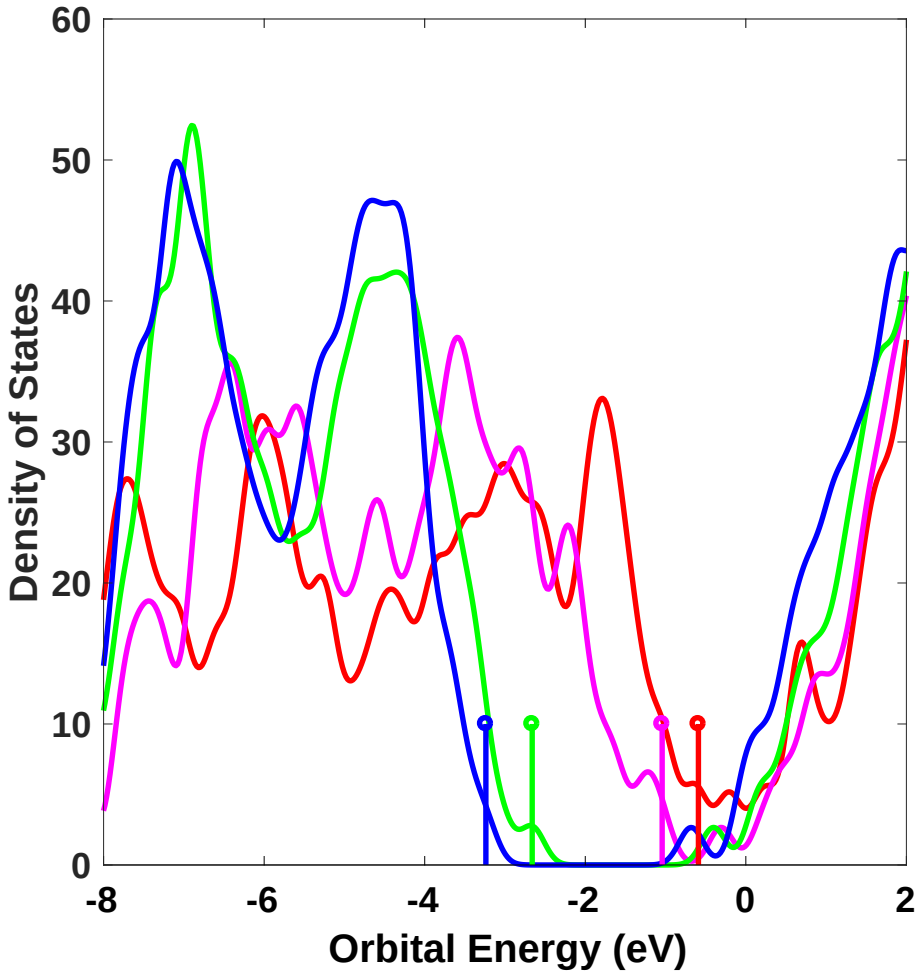

Figure B.4: Band structure of $Cd_{38}Se_{38}$ with Me_3PO ligands, at several points during the optimization. The red line is the band structure of the crystal structure before optimization, the pink line is early in the optimization (31 meV per atom from the optimized structure), the green line is mid-way through the optimization (5 meV per atom from the optimized structure), and the blue line is the optimized structure. The stems indicate the HOMO energy level for each structure.

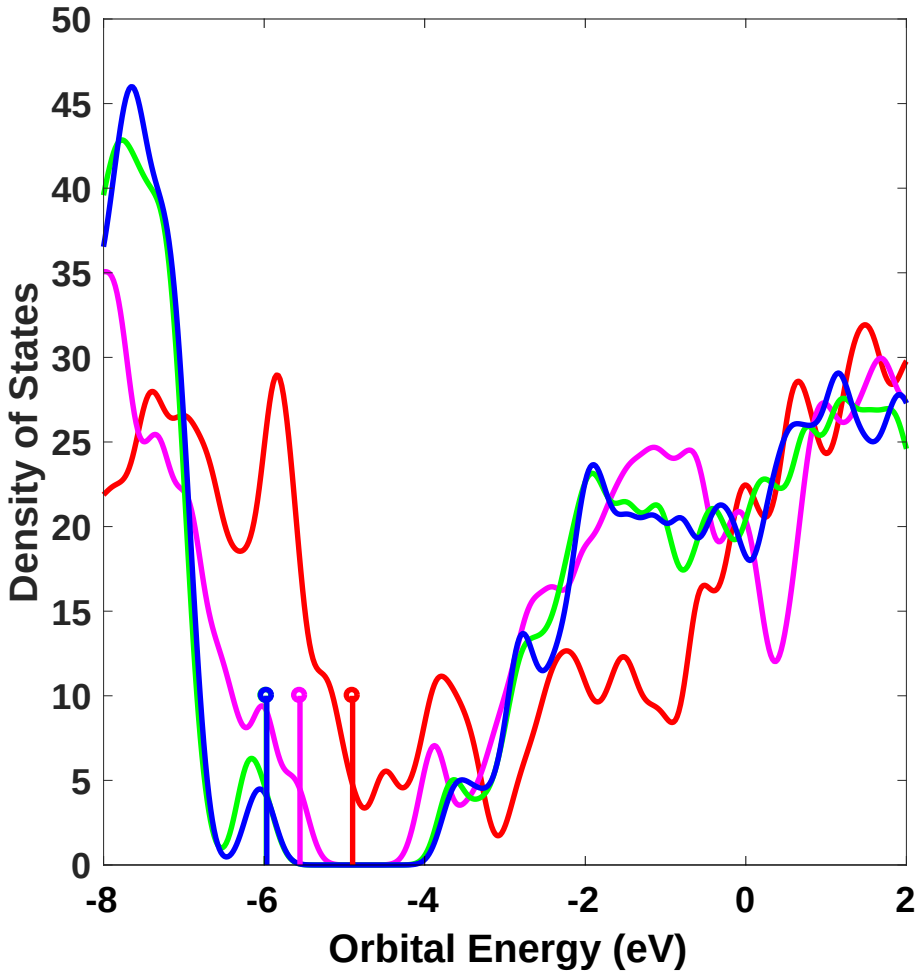

Figure B.5: Band structure of $Cd_{38}Se_{38}$ with no ligands, at several points during the optimization. The red line is the band structure of the crystal structure before optimization, the pink line is early in the optimization (93 meV per atom from the optimized structure), the green line is mid-way through the optimization (7.5 meV per atom from the optimized structure), and the blue line is the optimized structure. The stems indicate the HOMO energy level for each structure.

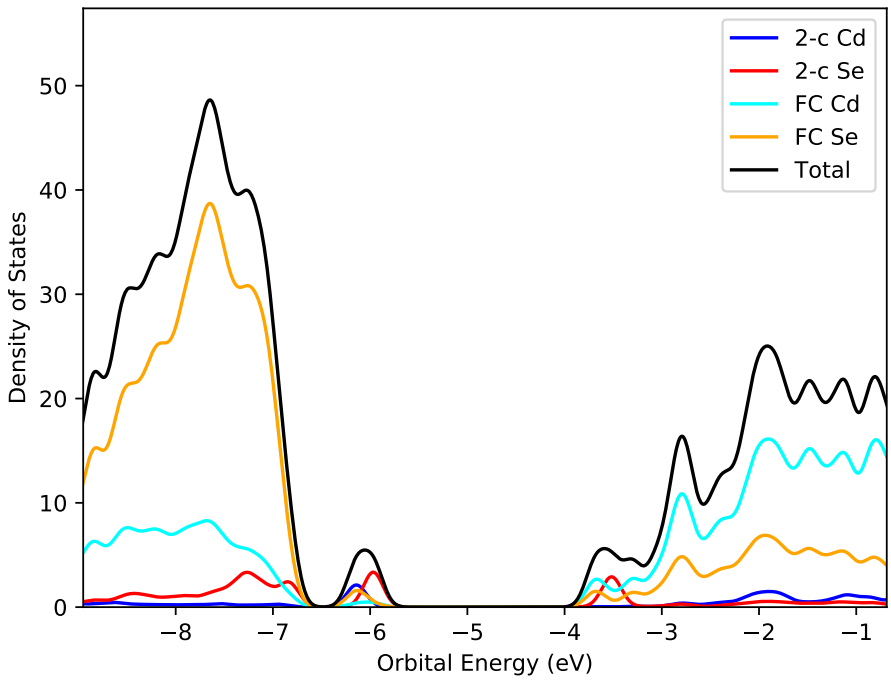

Figure B.6: Projected density of states for the $Cd_{38}Se_{38}$ structure with no ligands, showing the contribution of different types of atoms to the density of states. The blue line represents the contribution of 2-coordinate Cd atoms (including the clashing atoms), the red line represents 2-coordinate Se atoms (including the clashing atoms), the cyan line represents fully coordinated Cd (bonded to at least 3 Se atoms), and the orange line represents fully coordinated Se atoms (bonded to at least 3 Cd atoms). The red peak in the conduction band from 2-coordinate Se is from the clashing Se atoms, and the blue peak in the occupied orbitals from 2-coordinate Cd is from the clashing Cd atoms.

B.3 TDDFT spectra over the course of the optimization

B.3.1 $Cd_{38}Se_{38}$ with Me_3PO

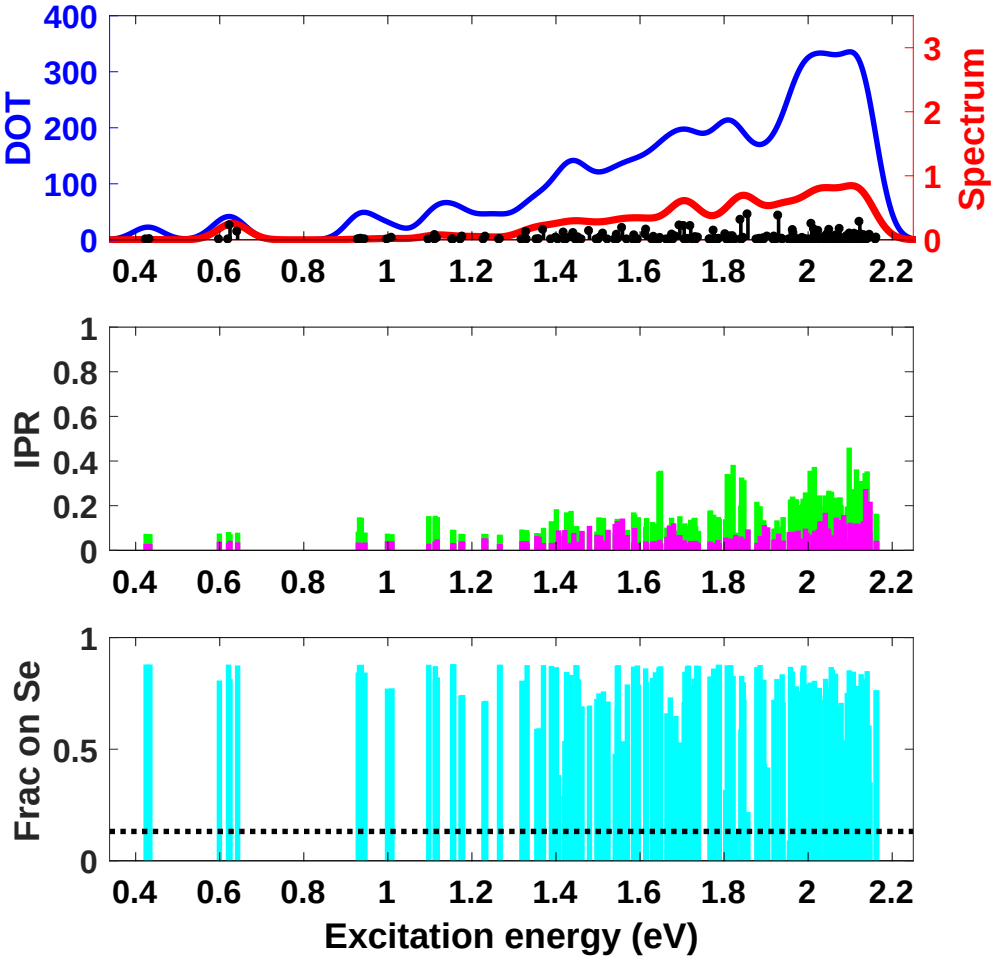

Figure B.7: TDDFT spectrum, IPR, and charge analysis for the $Cd_{38}Se_{38}$ dot with Me_3PO ligands, at a point early in the optimization (37 meV per atom from the optimized structure). The charge analysis shows the fraction of the hole density on undercoordinated Se atoms. The black dotted line indicates the fraction that would be expected on the 10 undercoordinated Se atoms if the excitation was fully delocalized over all 76 Cd and Se atoms.

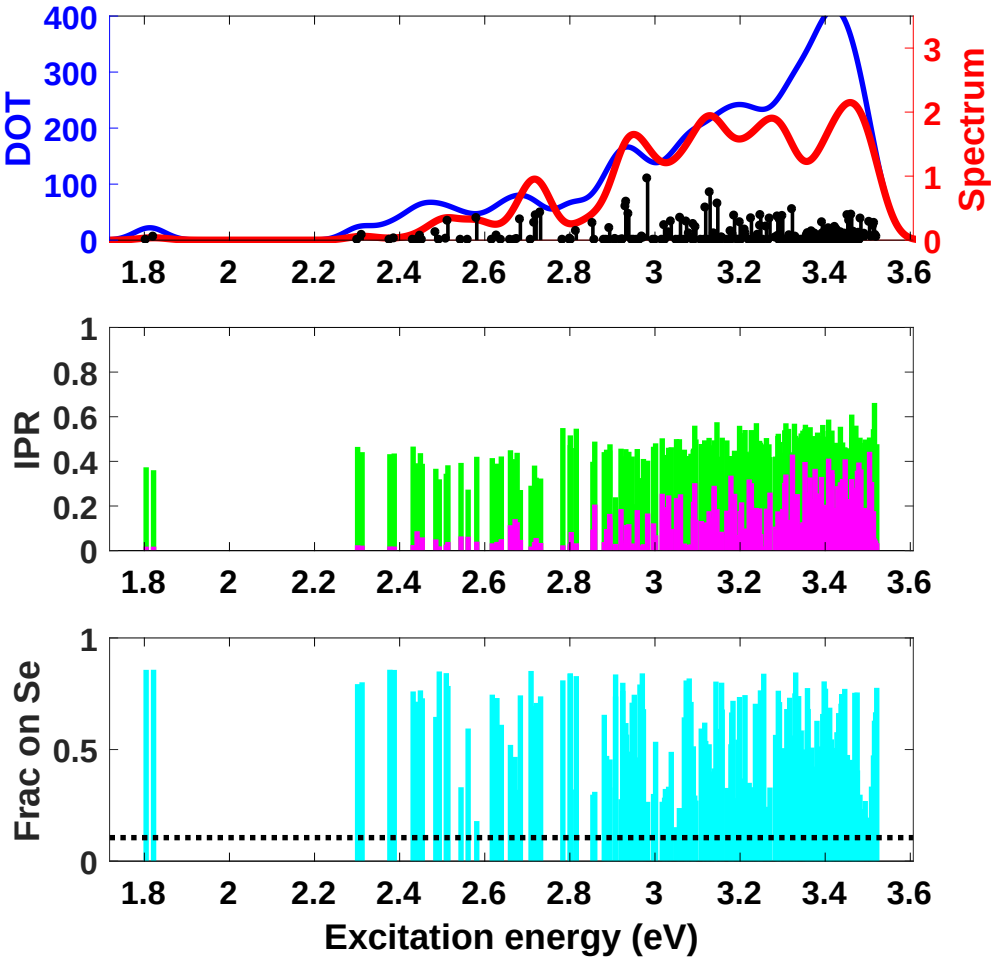

Figure B.8: TDDFT spectrum, IPR, and charge analysis for the $Cd_{38}Se_{38}$ dot with Me_3PO ligands, at a point mid-way through the optimization (5 meV per atom from the optimized structure). The charge analysis shows the fraction of the hole density on undercoordinated Se atoms. The black dotted line indicates the fraction that would be expected on the 8 undercoordinated Se atoms if the excitation was fully delocalized over all 76 Cd and Se atoms.

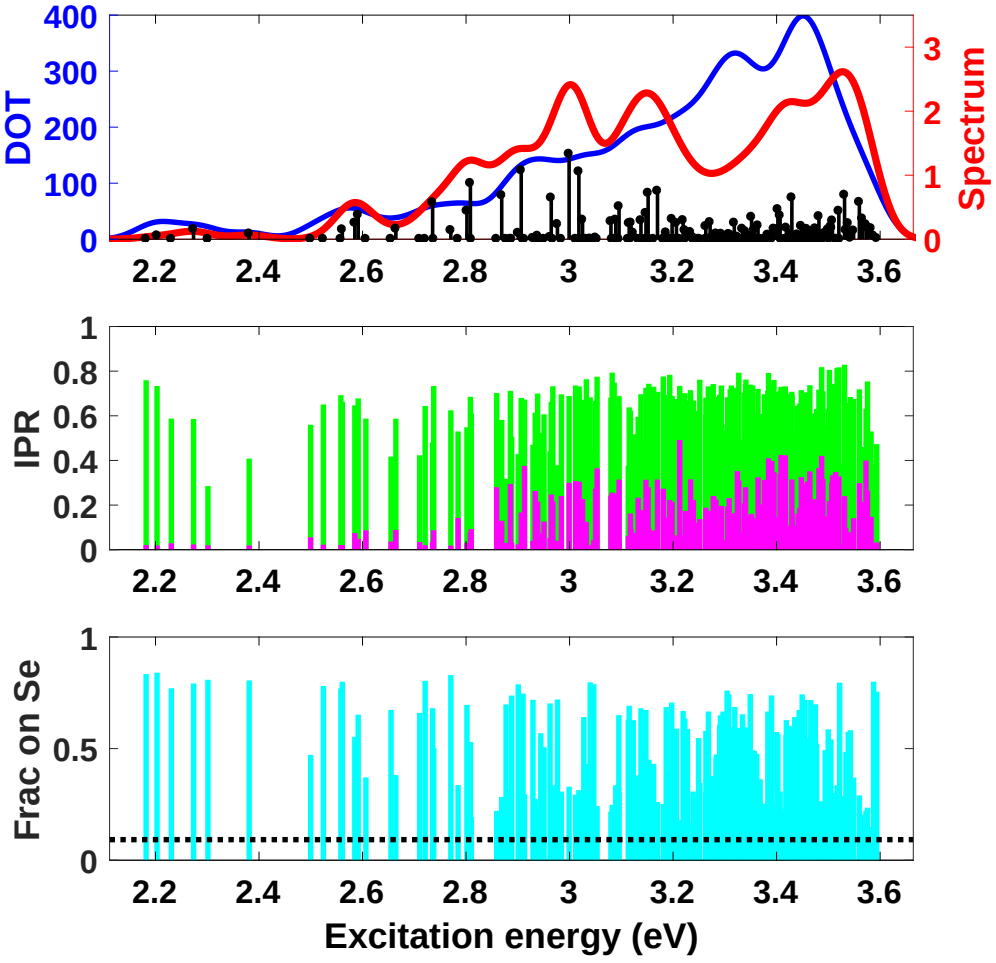

Figure B.9: TDDFT spectrum, IPR, and charge analysis for the $Cd_{38}Se_{38}$ dot with Me_3PO ligands, at the optimized structure. The charge analysis shows the fraction of the hole density on undercoordinated Se atoms. The black dotted line indicates the fraction that would be expected on the 7 undercoordinated Se atoms if the excitation was fully delocalized over all 76 Cd and Se atoms.

B.3.2 $Cd_{38}Se_{38}$ with no ligands

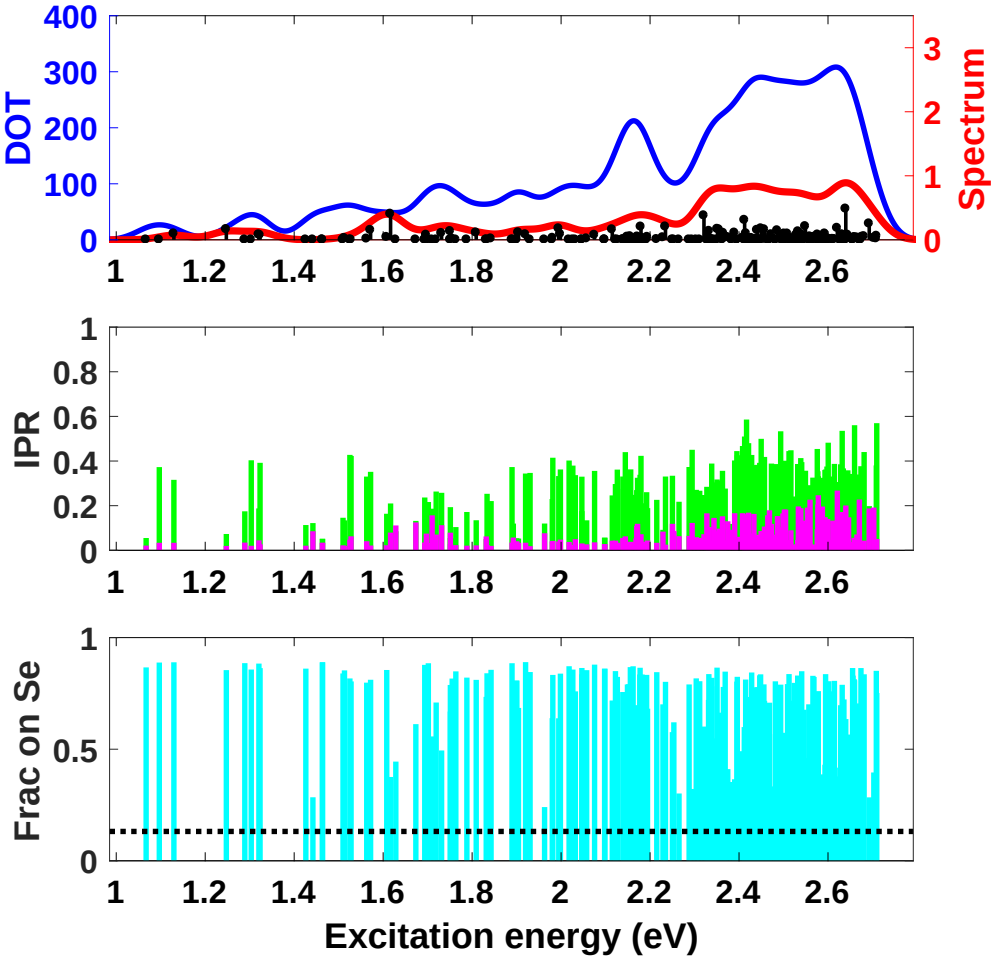

Figure B.10: TDDFT spectrum, IPR, and charge analysis for the $Cd_{38}Se_{38}$ dot with no ligands, at a point early in the optimization (93 meV per atom from the optimized structure). The charge analysis shows the fraction of the hole density on undercoordinated Se atoms. The black dotted line indicates the fraction that would be expected on the 10 undercoordinated Se atoms if the excitation was fully delocalized over all 76 Cd and Se atoms.

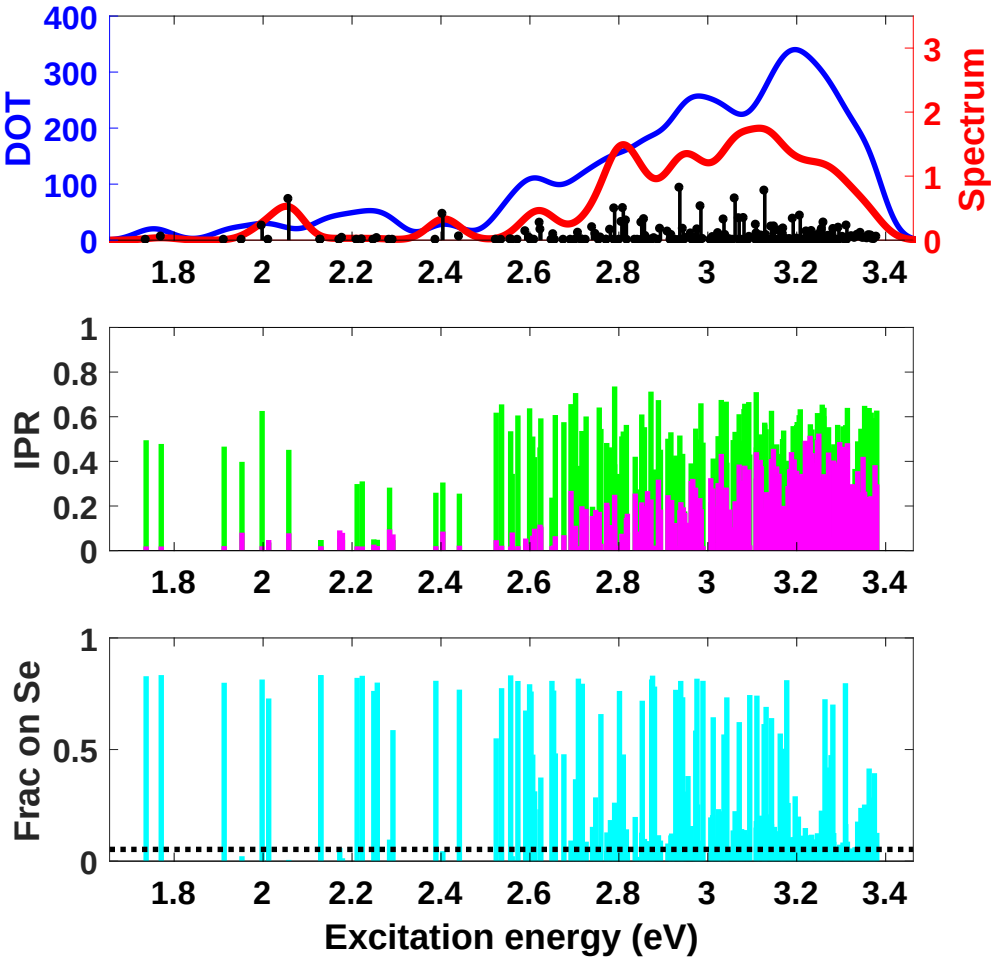

Figure B.11: TDDFT spectrum, IPR, and charge analysis for the $Cd_{38}Se_{38}$ dot with no ligands, at a point mid-way through the optimization (7.5 meV per atom from the optimized structure). The charge analysis shows the fraction of the hole density on undercoordinated Se atoms. The black dotted line indicates the fraction that would be expected on the 4 undercoordinated Se atoms if the excitation was fully delocalized over all 76 Cd and Se atoms.

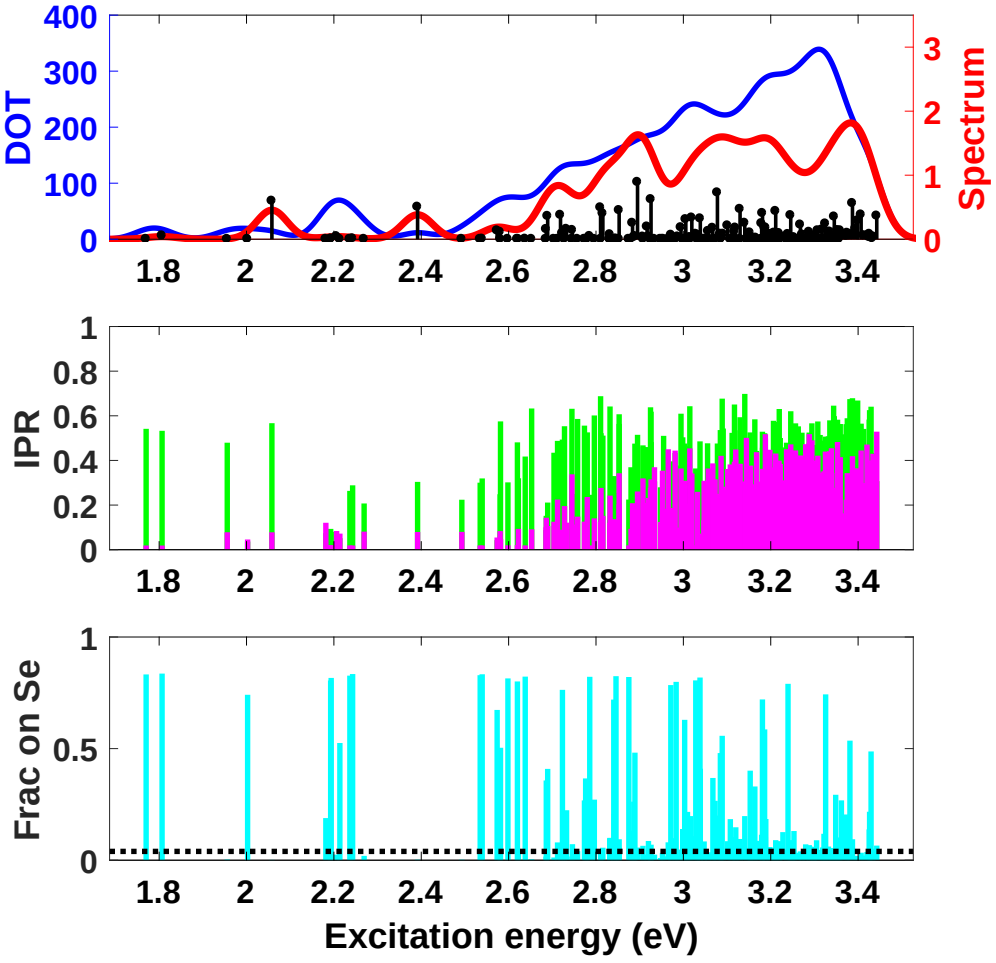

Figure B.12: TDDFT spectrum, IPR, and charge analysis for the $Cd_{38}Se_{38}$ dot with no ligands, at the optimized structure. The charge analysis shows the fraction of the hole density on undercoordinated Se atoms. The black dotted line indicates the fraction that would be expected on the 3 undercoordinated Se atoms if the excitation was fully delocalized over all 76 Cd and Se atoms.

B.4 Full charge breakdown over the course of optimization

B.4.1 $Cd_{38}Se_{38}$ with $MeNH_2$

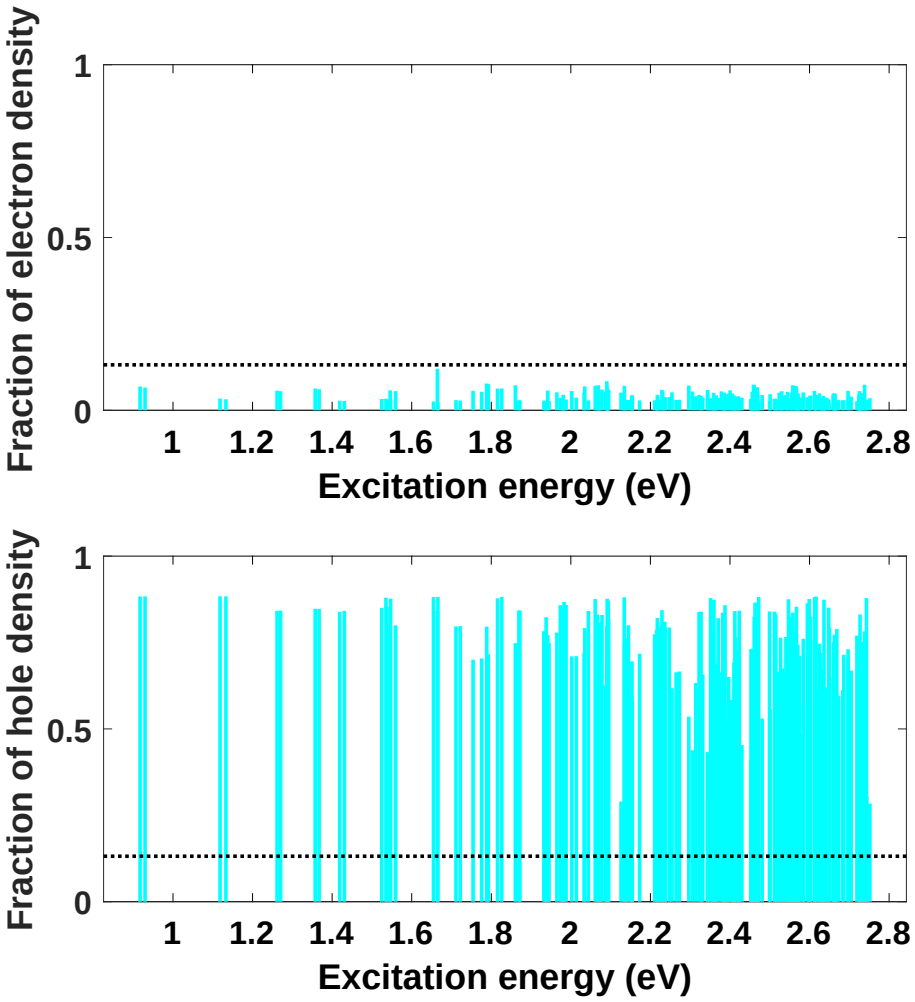

Figure B.13: Fraction of the excited state electron (top) and hole (bottom) Lowdin charge localized on the 10 undercoordinated Se atoms in $Cd_{38}Se_{38}$ with $MeNH_2$, at a point early in the optimization (31 meV per atom from the optimized structure). The black dotted line indicates the fraction of Lowdin charge that would be localized on these 10 atoms for an excitation delocalized over all 76 Cd and Se atoms.

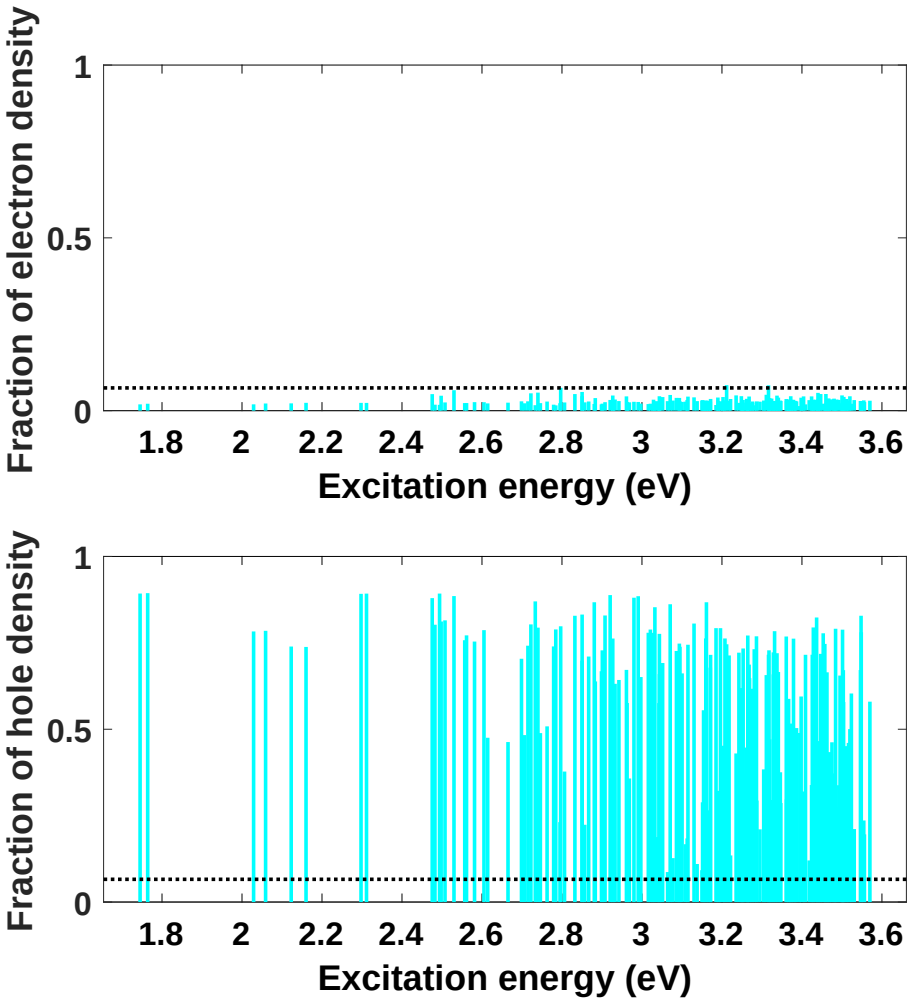

Figure B.14: Fraction of the excited state electron (top) and hole (bottom) Lowdin charge localized on the 5 undercoordinated Se atoms in $Cd_{38}Se_{38}$ with $MeNH_2$, at a point mid-way through the optimization (5 meV per atom from the optimized structure). The black dotted line indicates the fraction of Lowdin charge that would be localized on these 5 atoms for an excitation delocalized over all 76 Cd and Se atoms.

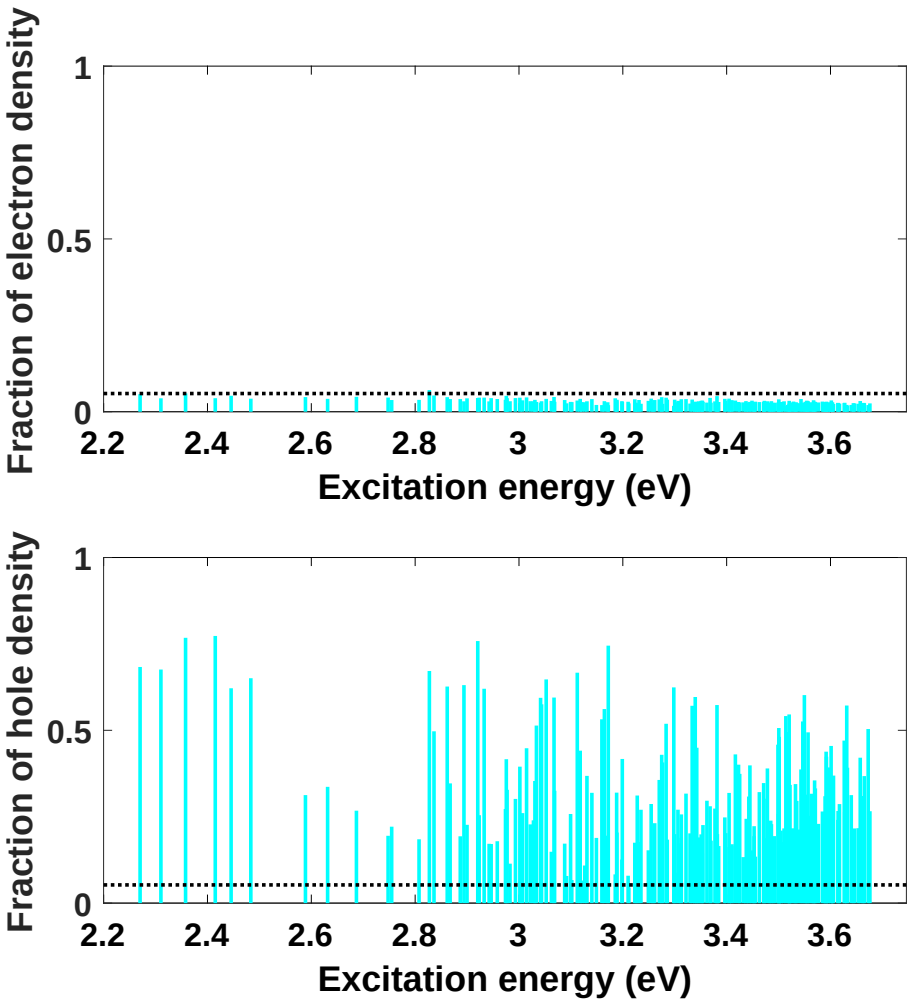

Figure B.15: Fraction of the excited state electron (top) and hole (bottom) Lowdin charge localized on the 4 undercoordinated Se atoms in $Cd_{38}Se_{38}$ with $MeNH_2$, for the optimized structure. The black dotted line indicates the fraction of Lowdin charge that would be localized on these 4 atoms for an excitation delocalized over all 76 Cd and Se atoms.

B.4.2 $Cd_{38}Se_{38}$ with Me_3PO

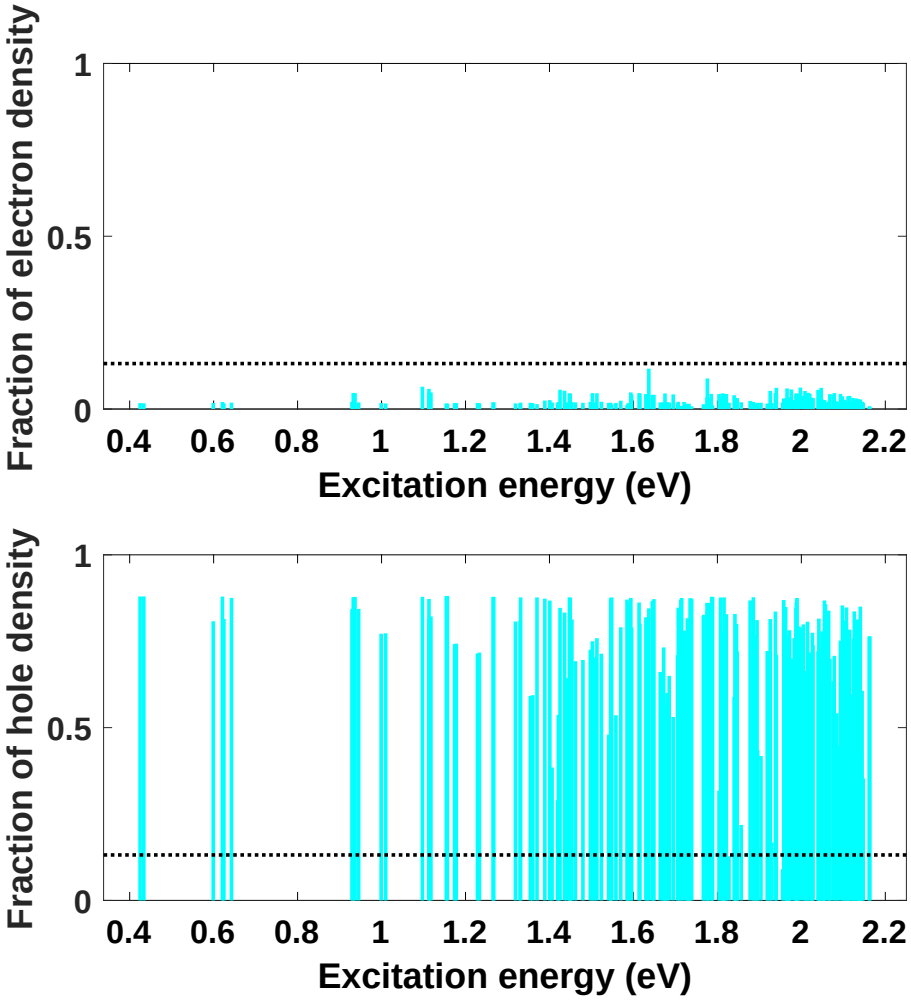

Figure B.16: Fraction of the excited state electron (top) and hole (bottom) Lowdin charge localized on the 10 undercoordinated Se atoms in $Cd_{38}Se_{38}$ with Me_3PO ligands, at a point early in the optimization (37 meV per atom from the optimized structure). The black dotted line indicates the fraction of Lowdin charge that would be localized on these 10 atoms for an excitation delocalized over all 76 Cd and Se atoms.

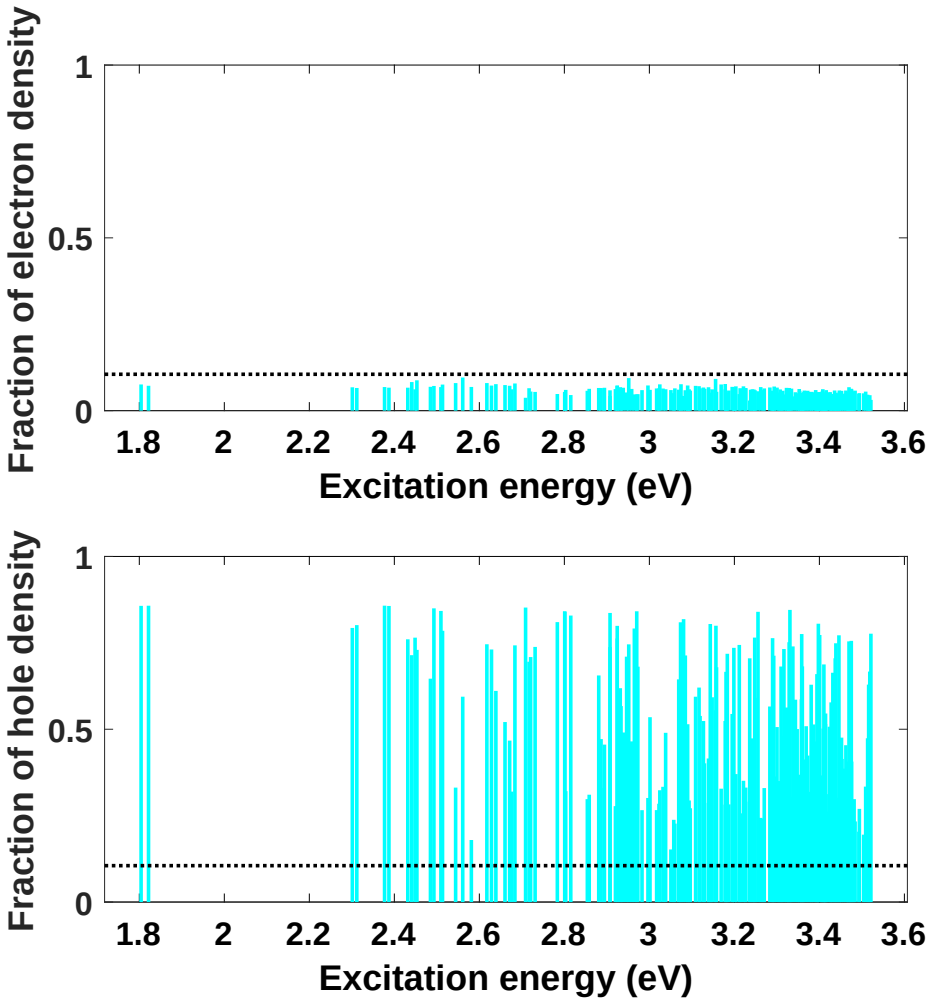

Figure B.17: Fraction of the excited state electron (top) and hole (bottom) Lowdin charge localized on the 8 undercoordinated Se atoms in $Cd_{38}Se_{38}$ with Me_3PO ligands, at a point mid-way through the optimization (3 meV per atom from the optimized structure). The black dotted line indicates the fraction of Lowdin charge that would be localized on these 8 atoms for an excitation delocalized over all 76 Cd and Se atoms.

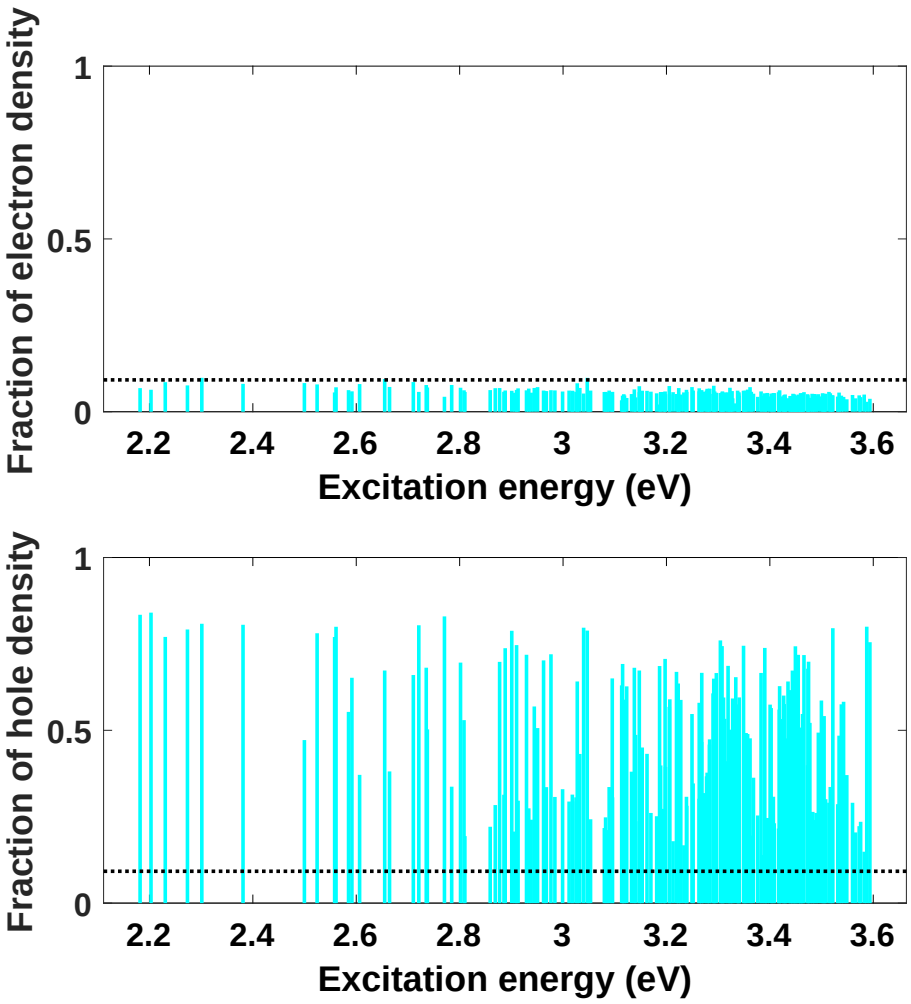

Figure B.18: Fraction of the excited state electron (top) and hole (bottom) Lowdin charge localized on the 7 undercoordinated Se atoms in $Cd_{38}Se_{38}$ with Me_3PO, for the optimized structure. The black dotted line indicates the fraction of Lowdin charge that would be localized on these 7 atoms for an excitation delocalized over all 76 Cd and Se atoms.

Appendix C

Supplementary Information for Chapter 5

C.1 MFSS model derivation

C.1.1 EL model

We consider the following processes that govern the populations of excitons (ϵ), charges (c), and vacancies (ϕ) at a given lattice site (a) and its nearest neighbor (nn):

$\phi^a \underset{k_{-ci}}{\overset{k_{ci}}{\rightleftharpoons}} \mathrm{c}^a$	Charge injection/leakage
$\mathrm{c}^a + \mathrm{c}^{\mathrm{nn}} \underset{k^a_{-\mathrm{rec}}}{\overset{k^a_{\mathrm{rec}}}{\rightleftharpoons}} \epsilon^a + \phi^{\mathrm{nn}}$	Charge recombination (on site a)
$\mathrm{c}^a + \mathrm{c}^{\mathrm{nn}} \underset{k^{nn}_{-\mathrm{rec}}}{\overset{k^{nn}_{\mathrm{rec}}}{\rightleftharpoons}} \phi^a + \epsilon^{\mathrm{nn}}$	Charge recombination (on nearest neighbor)
$\epsilon^a \xrightarrow{\mathrm{k}_r} \phi^a$	Exciton unimolecular decay
$\epsilon^a + \epsilon^{nn} \xrightarrow{\mathrm{k}^a_{\mathrm{EEA}}} \phi^a + \epsilon^{\mathrm{nn}}$	Exciton-exciton annihilation (on site a)
$\epsilon^a + \epsilon^{nn} \xrightarrow{\mathrm{k}^{\mathrm{nn}}_{\mathrm{EEA}}} \epsilon^a + \phi^{\mathrm{nn}}$	Exciton-exciton annihilation (on nearest neighbor)
$\epsilon^a + c^{nn} \xrightarrow{\mathrm{k}^a_{\mathrm{ECA}}} \phi^a + \mathrm{c}^{\mathrm{nn}}$	Exciton-charge annihilation (on site a)
$c^a + \epsilon^{nn} \xrightarrow{\mathrm{k}^{\mathrm{nn}}_{\mathrm{ECA}}} \mathrm{c}^a + \phi^{\mathrm{nn}}$	Exciton-charge annihilation (on nearest neighbor)
$c^a + \phi^{nn} \underset{k^a_{-\mathrm{DC}}}{\overset{k^a_{\mathrm{DC}}}{\rightleftharpoons}} \phi^a + \mathrm{c}^{\mathrm{nn}}$	Charge diffusion

$$\epsilon^a + \phi^{nn} \underset{k^a_{-\mathrm{DE}}}{\overset{k^a_{\mathrm{DE}}}{\rightleftharpoons}} \phi^a + \epsilon^{\mathrm{nn}} \qquad \text{Exciton diffusion}$$

We can then write the rate equations for each species at site a:

$$\begin{aligned}\frac{\mathrm{d}[\phi^a]}{\mathrm{d}t} = & -k^a_{ci}[\phi^a] + k_{-ci}[c^a] + k_u[\epsilon^a] + \sum_{nn}(k^a_{\mathrm{EEA}}[\epsilon^a][\epsilon^{nn}] + k^a_{\mathrm{ECA}}[\epsilon^a][c^{nn}] \\ & + k^{nn}_{\mathrm{rec}}[c^a][c^{nn}] - k^{nn}_{-\mathrm{rec}}[\phi^a][\epsilon^{nn}] + k^a_{\mathrm{DC}}[c^a][\phi^{nn}] - k^a_{-\mathrm{DC}}[\phi^a][c^{nn}] \\ & + k^a_{\mathrm{DE}}[\epsilon^a][\phi^{nn}] + k^a_{-\mathrm{DE}}[\phi^a][\epsilon^{nn}])\end{aligned} \tag{C.1}$$

$$\begin{aligned}\frac{\mathrm{d}[c^a]}{\mathrm{d}t} = & k^a_{ci}[\phi^a] - k_{-ci}[c^a] + \sum_{nn}(-k^a_{\mathrm{rec}}[c^a][c^{nn}] - k^{nn}_{\mathrm{rec}}[c^a][c^{nn}] + k^a_{-\mathrm{rec}}[\epsilon^a][\phi^{nn}] + k^{nn}_{-\mathrm{rec}}[\phi^a][\epsilon^{nn}] \\ & - k^a_{\mathrm{DC}}[c^a][\phi^{nn}] + k^a_{-\mathrm{DC}}[\phi^a][c^{nn}])\end{aligned} \tag{C.2}$$

$$\begin{aligned}\frac{\mathrm{d}[\epsilon^a]}{\mathrm{d}t} = & -k_u[\epsilon^a] + \sum_{nn}(k^a_{\mathrm{rec}}[c^a][c^{nn}] - k^a_{-\mathrm{rec}}[\epsilon^a][\phi^{nn}] - k^a_{\mathrm{EEA}}[\epsilon^a][\epsilon^{nn}] \\ & - k^a_{\mathrm{ECA}}[\epsilon^a][c^{nn}] - k^a_{\mathrm{DE}}[\epsilon^a][\phi^{nn}] + k^a_{-\mathrm{DE}}[\phi^a][\epsilon^{nn}])\end{aligned} \tag{C.3}$$

Note that the exciton-exciton annihilation and exciton-charge annihilation taking place on the nearest neighbor site does not actually affect the species at site a, and thus does not appear in the rate equation.

We define T, the total concnetration:

$$T = [\epsilon]^a + [c]^a + [\phi]^a \tag{C.4}$$

We divide the above equations by T, to convert the concentrations to fractions and

normalize the units on the rates:

$$\begin{aligned}\frac{1}{T}\frac{\mathrm{d}[\phi^a]}{\mathrm{d}t} = & -k^a_{ci}\frac{[\phi^a]}{T} + k_{-ci}\frac{[c^a]}{T} + k_u\frac{[\epsilon^a]}{T} + \sum_{nn}(Tk^a_{\mathrm{EEA}}\frac{[\epsilon^a]}{T}\frac{[\epsilon^{nn}]}{T} + Tk^a_{\mathrm{ECA}}\frac{[\epsilon^a]}{T}\frac{[c^{nn}]}{T} \\ & + Tk^{nn}_{\mathrm{rec}}\frac{[c^a]}{T}\frac{[c^{nn}]}{T} - Tk^{nn}_{-\mathrm{rec}}\frac{[\phi^a]}{T}\frac{[\epsilon^{nn}]}{T} + Tk^a_{\mathrm{DC}}\frac{[c^a]}{T}\frac{[\phi^{nn}]}{T} - Tk^a_{-\mathrm{DC}}\frac{[\phi^a]}{T}\frac{[c^{nn}]}{T} \\ & + Tk^a_{\mathrm{DE}}\frac{[\epsilon^a]}{T}\frac{[\phi^{nn}]}{T} + Tk^a_{-\mathrm{DE}}\frac{[\phi^a]}{T}\frac{[\epsilon^{nn}]}{T})\end{aligned} \tag{C.5}$$

$$\begin{aligned}\frac{1}{T}\frac{\mathrm{d}[c^a]}{\mathrm{d}t} = & k^a_{ci}\frac{[\phi^a]}{T} - k_{-ci}\frac{[c^a]}{T} + \sum_{nn}(-Tk^a_{\mathrm{rec}}\frac{[c^a]}{T}\frac{[c^{nn}]}{T} - Tk^{nn}_{\mathrm{rec}}\frac{[c^a]}{T}\frac{[c^{nn}]}{T} + Tk^a_{-\mathrm{rec}}\frac{[\epsilon^a]}{T}\frac{[\phi^{nn}]}{T} \\ & + Tk^{nn}_{-\mathrm{rec}}\frac{[\phi^a]}{T}\frac{[\epsilon^{nn}]}{T} - Tk^a_{\mathrm{DC}}\frac{[c^a]}{T}\frac{[\phi^{nn}]}{T} + Tk^a_{-\mathrm{DC}}\frac{[\phi^a]}{T}\frac{[c^{nn}]}{T})\end{aligned} \tag{C.6}$$

$$\begin{aligned}\frac{1}{T}\frac{\mathrm{d}[\epsilon^a]}{\mathrm{d}t} = & -k_u\frac{[\epsilon^a]}{T} + \sum_{nn}(Tk^a_{\mathrm{rec}}\frac{[c^a]}{T}\frac{[c^{nn}]}{T} - Tk^a_{-\mathrm{rec}}\frac{[\epsilon^a]}{T}\frac{[\phi^{nn}]}{T} - Tk^a_{\mathrm{EEA}}\frac{[\epsilon^a]}{T}\frac{[\epsilon^{nn}]}{T} \\ & - Tk^a_{\mathrm{ECA}}\frac{[\epsilon^a]}{T}\frac{[c^{nn}]}{T} - Tk^a_{\mathrm{DE}}\frac{[\epsilon^a]}{T}\frac{[\phi^{nn}]}{T} + Tk^a_{-\mathrm{DE}}\frac{[\phi^a]}{T}\frac{[\epsilon^{nn}]}{T})\end{aligned} \tag{C.7}$$

Defining $x_X = \frac{[X]}{T}$ and absorbing the extra factor of T into the bimolecular rate constants, we obtain:

$$\begin{aligned}\frac{\mathrm{d}x^a_\phi}{\mathrm{d}t} = & -k^a_{ci}x^a_\phi + k_{-ci}x^a_c + k_u x^a_\epsilon + \sum_{nn}(k^a_{\mathrm{EEA}}x^a_\epsilon x^{nn}_\epsilon + k^a_{\mathrm{ECA}}x^a_\epsilon x^{nn}_c \\ & + k^{nn}_{\mathrm{rec}}x^a_c x^{nn}_c - k^{nn}_{-\mathrm{rec}}x^a_\phi x^{nn}_\epsilon + k^a_{\mathrm{DC}}x^a_c x^{nn}_\phi - k^a_{-\mathrm{DC}}x^a_\phi x^{nn}_c \\ & + k^a_{\mathrm{DE}}x^a_\epsilon x^{nn}_\phi + k^a_{-\mathrm{DE}}x^a_\phi x^{nn}_\epsilon)\end{aligned} \tag{C.8}$$

$$\begin{aligned}\frac{\mathrm{d}x^a_c}{\mathrm{d}t} = & k^a_{ci}x^a_\phi - k_{-ci}x^a_c + \sum_{nn}(-k^a_{\mathrm{rec}}x^a_c x^{nn}_c - k^{nn}_{\mathrm{rec}}x^a_c x^{nn}_c + k^a_{-\mathrm{rec}}x^a_\epsilon x^{nn}_\phi \\ & + k^{nn}_{-\mathrm{rec}}x^a_\phi x^{nn}_\epsilon - k^a_{\mathrm{DC}}x^a_c x^{nn}_\phi + k^a_{-\mathrm{DC}}x^a_\phi x^{nn}_c)\end{aligned} \tag{C.9}$$

$$\begin{aligned}\frac{\mathrm{d}x^a_\epsilon}{\mathrm{d}t} = & -k_u x^a_\epsilon + \sum_{nn}(k^a_{\mathrm{rec}}x^a_c x^{nn}_c - k^a_{-\mathrm{rec}}x^a_\epsilon x^{nn}_\phi - k^a_{\mathrm{EEA}}x^a_\epsilon x^{nn}_\epsilon \\ & - k^a_{\mathrm{ECA}}x^a_\epsilon x^{nn}_c - k^a_{\mathrm{DE}}x^a_\epsilon x^{nn}_\phi + k^a_{-\mathrm{DE}}x^a_\phi x^{nn}_\epsilon)\end{aligned} \tag{C.10}$$

Where all the rate constants are in s^{-1}.

We then make the mean field approximation, replacing the sum over nearest neigh-

bors with an ensemble average:

$$\begin{aligned}\frac{\mathrm{d}x_\phi^a}{\mathrm{d}t} = & -k_{ci}^a x_\phi^a + k_{-ci} x_c^a + k_u x_\epsilon^a + N(k_{\mathrm{EEA}}^a x_\epsilon^a \bar{x}_\epsilon + k_{\mathrm{ECA}}^a x_\epsilon^a \bar{x}_c \\ & + k_{\mathrm{rec}} x_c \overline{x}_c^a - \overline{k_{-\mathrm{rec}} x_\epsilon} x_\phi^a + k_{\mathrm{DC}}^a x_c^a \bar{x}_\phi - k_{-\mathrm{DC}}^a x_\phi^a \bar{x}_c \\ & + k_{\mathrm{DE}}^a x_\epsilon^a \bar{x}_\phi + k_{-\mathrm{DE}}^a x_\phi^a \bar{x}_\epsilon)\end{aligned} \tag{C.11}$$

$$\begin{aligned}\frac{\mathrm{d}x_c^a}{\mathrm{d}t} = & k_{ci}^a x_\phi^a - k_{-ci} x_c^a + N(-k_{\mathrm{rec}}^a x_c^a \bar{x}_c - \overline{k_{\mathrm{rec}} x_c} x_c^a + k_{-\mathrm{rec}}^a x_\epsilon^a \bar{x}_\phi \\ & + \overline{k_{-\mathrm{rec}} x_\epsilon} x_\phi^a - k_{\mathrm{DC}}^a x_c^a \bar{x}_\phi + k_{-\mathrm{DC}}^a x_\phi^a \bar{x}_c)\end{aligned} \tag{C.12}$$

$$\begin{aligned}\frac{\mathrm{d}x_\epsilon^a}{\mathrm{d}t} = & -k_u x_\epsilon^a + N(k_{\mathrm{rec}}^a x_c^a \bar{x}_c - k_{-\mathrm{rec}}^a x_\epsilon^a \bar{x}_\phi - k_{\mathrm{EEA}}^a x_\epsilon^a \bar{x}_\epsilon \\ & - k_{\mathrm{ECA}}^a x_\epsilon^a \bar{x}_c - k_{\mathrm{DE}}^a x_\epsilon^a \bar{x}_\phi + k_{-\mathrm{DE}}^a x_\phi^a \bar{x}_\epsilon)\end{aligned} \tag{C.13}$$

$$1 = x_\epsilon^a + x_c^a + x_\phi^a \tag{C.14}$$

Where N is the number of nearest neighbors, and $\overline{Y}$ indicates an ensemble average of quantity Y over the lattice. Equations C.11-C.14 can be solved to yield expressions for the the concentrations of excitons, charges, and vacancies at site a:

$$
\begin{cases}
Dx_\phi & = (k_{-ci} + N\overline{k_{\mathrm{rec}}x_c} + Nk_{\mathrm{DC}}\bar{x_\phi})(k_u + Nk^a_{-\mathrm{rec}}\bar{x_\phi} + Nk^a_{\mathrm{EEA}}\bar{x_\epsilon} + Nk^a_{\mathrm{ECA}}\bar{x_c} + Nk_{\mathrm{DE}}\bar{x_\phi}) \\
& +Nk^a_{\mathrm{rec}}\bar{x_c}(k_u + Nk^a_{\mathrm{EEA}}\bar{x_\epsilon} + Nk^a_{\mathrm{ECA}}\bar{x_c} + Nk_{\mathrm{DE}}\bar{x_\phi}), \\
Dx_c & = (k^a_{ci} + N\overline{k_{-\mathrm{rec}}x_\epsilon} + Nk_{-\mathrm{DE}}\bar{x_c})(k_u + Nk^a_{-\mathrm{rec}}\bar{x_\phi} + Nk^a_{\mathrm{EEA}}\bar{x_\epsilon} + Nk^a_{\mathrm{ECA}}\bar{x_c} + Nk_{\mathrm{DE}}\bar{x_\phi}) \\
& +(Nk_{-\mathrm{DE}}\bar{x_\epsilon})Nk^a_{-\mathrm{rec}}\bar{x_\phi}, \\
Dx_\epsilon & = Nk^a_{\mathrm{rec}}\bar{x_c}(k^a_{ci} + N\overline{k_{-\mathrm{rec}}x_\epsilon} + Nk_{-\mathrm{DC}}\bar{x_c}) + Nk_{-\mathrm{DE}}\bar{x_\epsilon}) \\
& (k_{-ci} + Nk^a_{\mathrm{rec}}\bar{x_c} + N\overline{k_{\mathrm{rec}}x_c} + Nk_{\mathrm{DC}}\bar{x_\phi}), \\
D & = (k^a_{ci} + N\overline{k_{-\mathrm{rec}}x_\epsilon} + Nk_{-\mathrm{DC}}\bar{x_c})(Nk^a_{\mathrm{rec}}\bar{x_c} + k_u + Nk^a_{-\mathrm{rec}}\bar{x_\phi} + Nk^a_{\mathrm{EEA}}\bar{x_\epsilon} + Nk^a_{\mathrm{ECA}}\bar{x_c} + Nk_{\mathrm{DE}}\bar{x_\phi}) \\
& +Nk_{-\mathrm{DE}}\bar{x_\epsilon})(k_{-ci} + Nk^a_{\mathrm{rec}}\bar{x_c} + N\overline{k_{\mathrm{rec}}x_c} + Nk^a_{-\mathrm{rec}}\bar{x_\phi} + Nk_{\mathrm{DC}}\bar{x_\phi}) \\
& +(k_{-ci} + N\overline{k_{\mathrm{rec}}x_c} + Nk_{\mathrm{DC}}\bar{x_\phi})(k_u + Nk^a_{-\mathrm{rec}}\bar{x_\phi} + Nk^a_{\mathrm{EEA}}\bar{x_\epsilon} + Nk^a_{\mathrm{ECA}}\bar{x_c} + Nk_{\mathrm{DE}}\bar{x_\phi}) \\
& +Nk^a_{\mathrm{rec}}\bar{x_c}(k_u + Nk^a_{\mathrm{EEA}}\bar{x_\epsilon} + Nk^a_{\mathrm{ECA}}\bar{x_c} + Nk_{\mathrm{DE}}\bar{x_\phi}).
\end{cases}
\tag{C.15}
$$

Note that, because we do not consider disorder in the recombination rate here, the joint averages $\overline{k_{\mathrm{rec}}x_c}$ and $\overline{k_{-\mathrm{rec}}x_\epsilon}$ reduce to $k_{\mathrm{rec}}\bar{x_c}$ and $k_{-\mathrm{rec}}\bar{x_\epsilon}$, respectively. We only need to consider the averages:

$$
\bar{x_\epsilon} = \frac{1}{M}\sum_{a=1}^{M} x^a_\epsilon \tag{C.16}
$$

$$
\bar{x_\phi} = \frac{1}{M}\sum_{a=1}^{M} x^a_\phi \tag{C.17}
$$

$$
\bar{x_c} = \frac{1}{M}\sum_{a=1}^{M} x^a_c \tag{C.18}
$$

Equations C.16-C.18 must be solved self-consistently with C.15, as the ensemble averages depend on the single-site populations.

C.1.2 Photoluminescence model

To model photoluminescence experiments, such as the relative PLQY vs exciton density curve, we built a model of photoluminescence in an OLED. The details of the simulation are the same as above, but we consider the following processes that govern the kinetics at site a:

$$\phi^a \xrightarrow{\mathrm{k_{ei}}} \epsilon^a \qquad \text{Exciton injection}$$

$$\mathrm{c}^a + \mathrm{c}^{\mathrm{nn}} \underset{k^a_{-\mathrm{rec}}}{\overset{k^a_{\mathrm{rec}}}{\rightleftharpoons}} \epsilon^a + \phi^{\mathrm{nn}} \qquad \text{Charge recombination (on site a)}$$

$$\mathrm{c}^a + \mathrm{c}^{\mathrm{nn}} \underset{k^{nn}_{-\mathrm{rec}}}{\overset{k^{nn}_{\mathrm{rec}}}{\rightleftharpoons}} \phi^a + \epsilon^{\mathrm{nn}} \qquad \text{Charge recombination (on nearest neighbor)}$$

$$\epsilon^a \xrightarrow{\mathrm{k}_u} \phi^a \qquad \text{Exciton unimolecular decay}$$

$$\epsilon^a + \epsilon^{nn} \xrightarrow{\mathrm{k^{nn}_{EEA}}} \epsilon^a + \phi^{\mathrm{nn}} \qquad \text{Exciton-exciton annihilation (on site a)}$$

$$\epsilon^a + \epsilon^{nn} \xrightarrow{\mathrm{k^{a}_{EEA}}} \phi^a + \epsilon^{\mathrm{nn}} \qquad \text{Exciton-exciton annihilation (on nearest neighbor)}$$

$$\epsilon^a + c^{nn} \xrightarrow{\mathrm{k^{a}_{ECA}}} \phi^a + \mathrm{c}^{\mathrm{nn}} \qquad \text{Exciton-charge annihilation (on site a)}$$

$$c^a + \epsilon^{nn} \xrightarrow{\mathrm{k^{nn}_{ECA}}} \mathrm{c}^a + \phi^{\mathrm{nn}} \qquad \text{Exciton-exciton annihilation (on nearest neighbor)}$$

$$c^a + \phi^{nn} \underset{k^a_{-\mathrm{DC}}}{\overset{k^a_{\mathrm{DC}}}{\rightleftharpoons}} \phi^a + \mathrm{c}^{\mathrm{nn}} \qquad \text{Charge diffusion}$$

$$\epsilon^a + \phi^{nn} \underset{k^a_{-\mathrm{DE}}}{\overset{k^a_{\mathrm{DE}}}{\rightleftharpoons}} \phi^a + \epsilon^{\mathrm{nn}} \qquad \text{Exciton diffusion}$$

After following the procedure outlined above, we find the solution:

$$
\begin{cases}
Dx_\phi &= Nk^a_{rec}k^a_{ECA}\bar{x_c}^2 + (\overline{k_{rec}x_c} + k_{DC}\bar{x_\phi})(k_{-ei} + k_u + Nk^a_{EEA}\bar{x_\epsilon} + N(k^a_{-rec} + k_{DE})\bar{x_\phi}) \\
&\quad +(k_{-ei}k^a_{rec} + k_uk^a_{rec} + N(k^a_{EEA}k^a_{rec}\bar{x_\epsilon} + k^a_{ECA}\overline{k_{rec}x_c} + k_{DC}k^a_{ECA}\bar{x_\phi} + k_{DE}k^a_{rec}\bar{x_\phi}))\bar{x_c}\ , \\
Dx_c &= (k_{-DC}\bar{x_c} + \overline{k_{-rec}x_\epsilon})(k_{-ei} + k_u + Nk^a_{ECA}\bar{x_c} + Nk^a_{EEA}\bar{x_\epsilon}) \\
&\quad +((k_{-DC}\bar{x_c} + \overline{k_{-rec}x_\epsilon})k_{DE}N + k^a_{-rec}(k_{ei} + N((k_{-DC} + (k_{-DE} + \overline{k_{-rec}x_\epsilon})))\bar{x_\phi}\ , \\
Dx_\epsilon &= N(k_{-DC})k^a_{rec}\bar{x_c}^2 + (k_{ei} + N(k_{-DE})(\overline{k_{rec}x_c} + k_{DC}\bar{x_\phi}) \\
&\quad +(k_{ei}k^a_{rec} + N(k_{-DE} + \overline{k_{-rec}x_\epsilon})k^a_{rec}\bar{x_c}\ , \\
D &= \overline{k_{-rec}x_\epsilon}(k_{-ei} + k_u + Nk^a_{EEA}\bar{x_\epsilon} + Nk^a_{ECA}\bar{x_c} + Nk^a_{rec}\bar{x_c}) \\
&\quad +\overline{k_{rec}x_c}(k_{-ei} + k_{ei} + k_u + Nk_{-DE}\bar{x_\epsilon} + Nk^a_{EEA}\bar{x_\epsilon} + Nk^a_{ECA}\bar{x_c}) \\
&\quad +N(k_{-DC}k^a_{ECA} + (k_{-DC} + k^a_{ECA})k^a_{rec})\bar{x_c}^2 + (k_{-ei}k_{DC} + k^a_{-rec}k^a_{ei} + k_{DC}k^a_{ei} + k_{DC}k_u)\bar{x_\phi} \\
&\quad +N(k_{-DE} + k_{DC})\bar{x_\epsilon}\bar{x_\phi} + Nk_{DC}k^a_{EEA}\bar{x_\epsilon}\bar{x_\phi} + N(k^a_{-rec} + k_{DE})(\overline{k_{-rec}x_\epsilon} + \overline{k_{rec}x_c})\bar{x_\phi} \\
&\quad +Nk_{DC}(k^a_{-rec} + k_{DE})\bar{x_\phi}^2 + (k_{-ei}k^a_{rec} + k_{ei}k^a_{rec} + k_uk_{rec})\bar{x_c} + Nk^a_{rec}(k_{-DE} + k^a_{EEA})\bar{x_\epsilon}\bar{x_c} \\
&\quad +k_{DC}) + k_{DC}k^a_{ECA} + k_{DE}k^a_{rec})\bar{x_\phi}\bar{x_c} \\
&\quad +k_{-DC}(k_{-ei} + k_u + Nk^a_{EEA}\bar{x_\epsilon} + N(k^a_{-rec} + k_{DE})\bar{x_\phi})\bar{x_c}
\end{cases}
\tag{C.19}
$$

Which, again must be solved self-consistently.

C.2 Sensitivity analysis

Our sensitivity analysis procedure is as follows:

We define:

$$
\vec{T} = \frac{MFSS - Expt}{Expt} \tag{C.20}
$$

T is the pointwise differnce between the model and experiment.

We then build the Hessian matrix, using the second derivatives of T:

$$\chi(k_i, k_j) = \frac{\partial^2 T}{\partial k_i \partial k_j} \frac{1}{1 - R^2} \tag{C.21}$$

R^2 refers to the r-squared value obtained when fitting a fifth-degree polynomial to the experimental data, such that $1 - R^2$ is an estimate of the experimental error.

We then use the relation:

$$\chi_{ii}^{-1} = \sigma_i^2 \tag{C.22}$$

To estimate the uncertainty in each parameter.

C.3 Model fits with disorder in different parameters

To obtain the fits presented in the paper, we optimized the fit to each device three times, once with disorder in the EEA rate, once with disorder in the ECA rate, and once with no disorder. We then chose the set of rate constants that gave the best overall fit. Here, we report the best fit parameters for each of these three scenarios for each device.

C.3.1 CBP

Parameter	Disorder in EEA	No disorder	Disorder in ECA	Disorder in k_{u}
$k_{-\mathrm{ci}}$	$8.5426(9) \times 10^3$	$8.543(1) \times 10^3$	$8.578(1) \times 10^3$	$6.391(1) \times 10^3$
k_{rec}	$6.543(2) \times 10^8$	$6.733(2) \times 10^8$	$6.732(2) \times 10^8$	$2.977(1) \times 10^8$
k_{u}	$3.9(1) \times 10^5$	$3.89(9) \times 10^5$	$3.5(1) \times 10^5$	$2.7(4) \times 10^5$
k_{EEA}	$7.3(4) \times 10^7$	$1.05(5) \times 10^8$	$8.9(5) \times 10^7$	$3.9(1) \times 10^7$
k_{ECA}	$8.5(3) \times 10^7$	$8.0(2) \times 10^7$	$4.0(1) \times 10^7$	$4.19(6) \times 10^7$
σ^2	846	0	756	66.8
η	0.3714	0.3740	0.3711	0.3600

Table C.1: Parameters used to model the CBP device. All rate constants are in units of s^{-1}, σ^2 is in units of meV^2, and η is unitless. Parentheses indicate the uncertainty in the last digit.

C.3.2 Br_2CBP

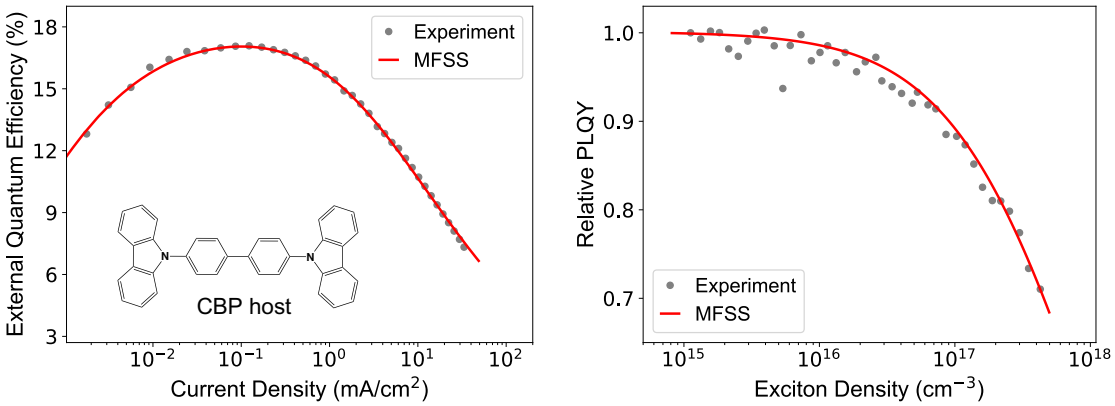

Figure C.1: Results for the CBP device, with disorder in the EEA rate constant.

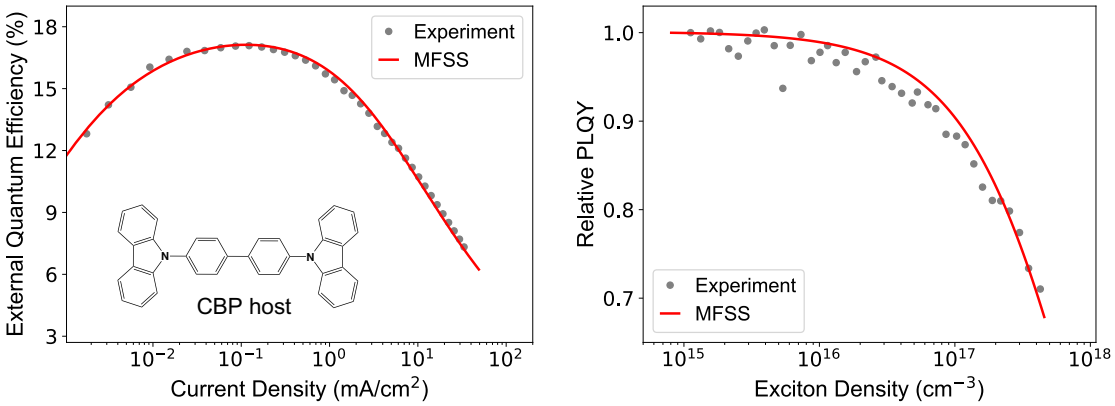

Figure C.2: Results for the CBP device, with disorder in the ECA rate constant.

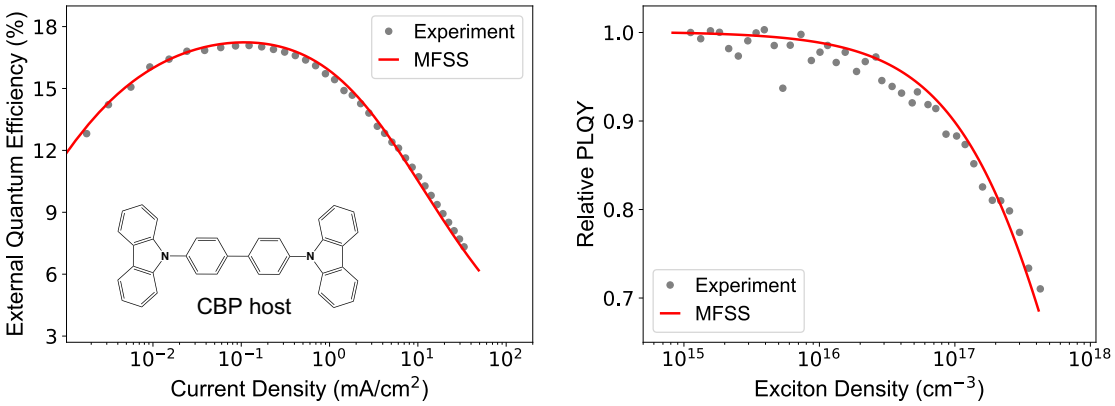

Figure C.3: Results for the CBP device, with no disorder.

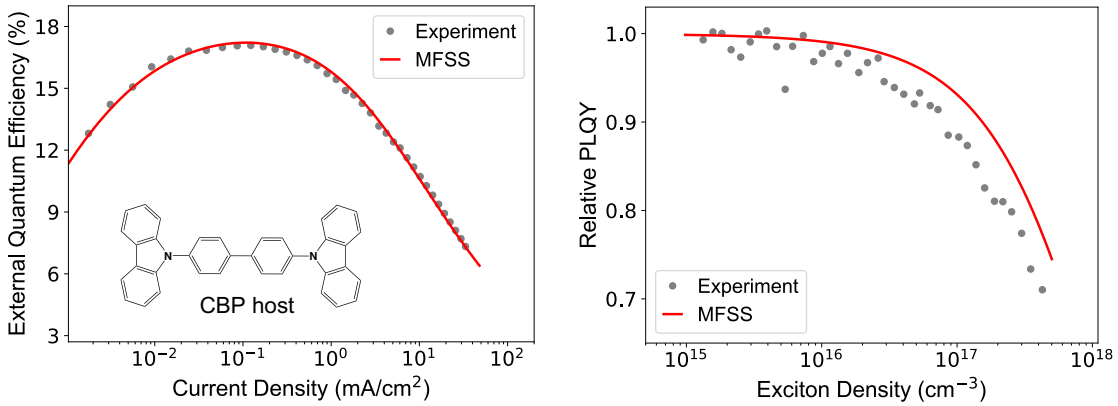

Figure C.4: Results for the CBP device, with disorder in k_u.

Parameter	Disorder in ECA	No disorder	Disorder in EEA	Disorder in k_u
k_{-ci}	$4.6752(1) \times 10^3$	$4.00046(8) \times 10^3$	$4.28025(8) \times 10^3$	$3.077(3) \times 10^3$
k_{rec}	$4.6115(2) \times 10^8$	$4.4413(2) \times 10^8$	$4.4849(2) \times 10^8$	$8.805(1) \times 10^7$
k_u	$3.64(1) \times 10^5$	$4.01(1) \times 10^5$	$4.02(1) \times 10^5$	$6.63(2) \times 10^5$
k_{EEA}	$1.136(8) \times 10^7$	$1.187(8) \times 10^7$	$8.00(5) \times 10^6$	$1.45(1) \times 10^7$
k_{ECA}	$6.72(2) \times 10^7$	$7.62(2) \times 10^7$	$7.52(3) \times 10^7$	$4.79(2) \times 10^7$
σ^2_{ECA}	641	0	1.11×10^3	227
η	0.3860	0.3719	0.3748	0.3272

Table C.2: Parameters used for the Br_2CBP device. All rate constants are in units of s^{-1}, σ^2 is in units of meV^2, and η is unitless. Parentheses indicate the uncertainty in the last digit.

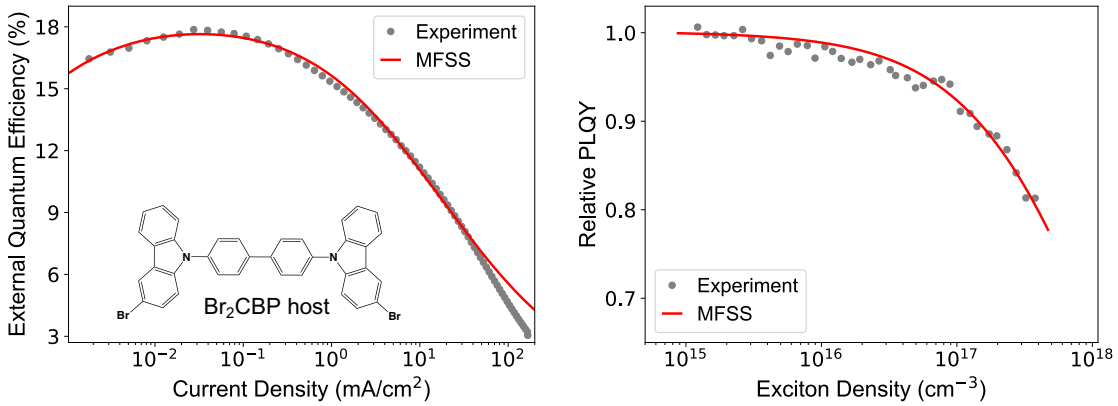

Figure C.5: Results for the Br_2CBP device, with disorder in the EEA rate constant.

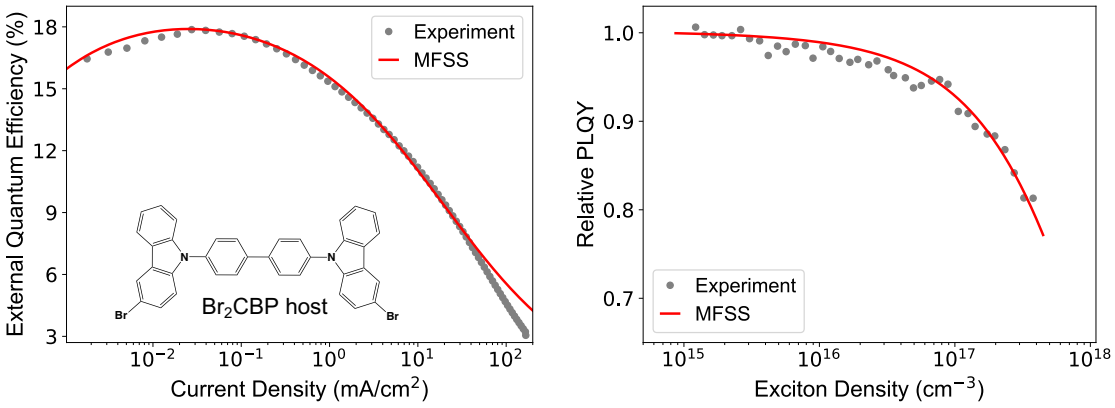

Figure C.6: Results for the Br_2CBP device, with disorder in the ECA rate constant.

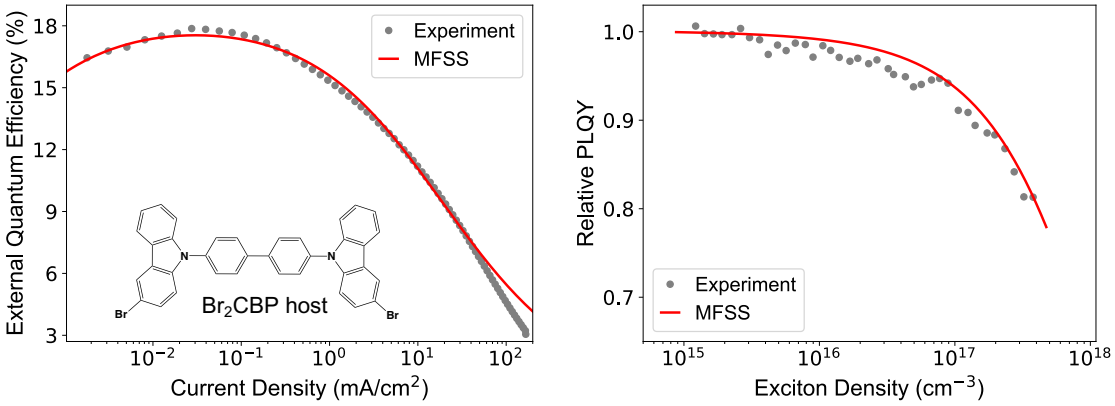

Figure C.7: Results for the Br_2CBP device, with no disorder.

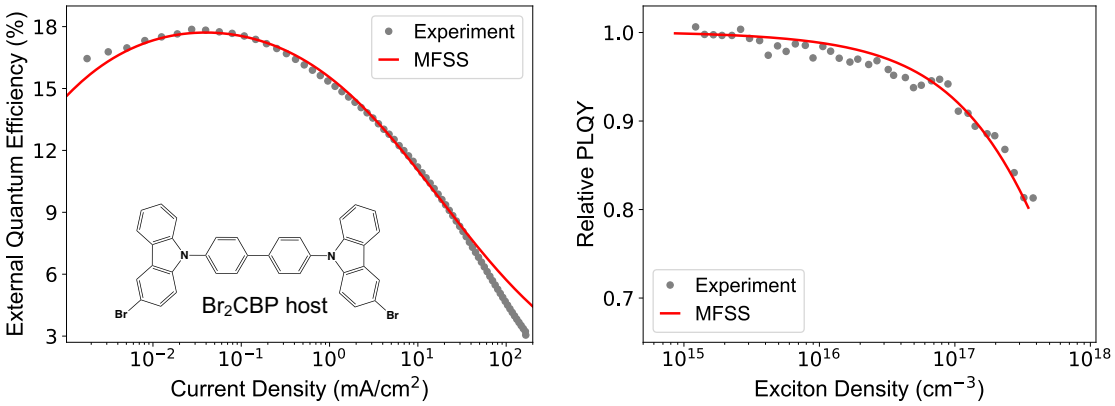

Figure C.8: Results for the Br_2CBP device, with disorder in k_u.

Bibliography

[1] Daniel E. Gómez, Marco Califano, and Paul Mulvaney. Optical properties of single semiconductor nanocrystals. *Phys. Chem. Chem. Phys.*, 8(43):4989–5011, 2006.

[2] Cherie R. Kagan, Efrat Lifshitz, Edward H. Sargent, and Dmitri V. Talapin. Building devices from colloidal quantum dots. *Science*, 353(6302):aac5523, August 2016.

[3] Arthur J Nozik, Matthew C Beard, Joseph M Luther, Matt Law, Randy J Ellingson, and Justin C Johnson. Semiconductor quantum dots and quantum dot arrays and applications of multiple exciton generation to third-generation photovoltaic solar cells. *Chemical reviews*, 110(11):6873–6890, 2010.

[4] Chia-Hao Marcus Chuang, Andrea Maurano, Riley E Brandt, Gyu Weon Hwang, Joel Jean, Tonio Buonassisi, Vladimir Bulović, and Moungi G Bawendi. Open-circuit voltage deficit, radiative sub-bandgap states, and prospects in quantum dot solar cells. *Nano letters*, 15(5):3286–3294, 2015.

[5] Liang-Yi Chang, Richard R Lunt, Patrick R Brown, Vladimir Bulović, and Moungi G Bawendi. Low-temperature solution-processed solar cells based on pbs colloidal quantum dot/cds heterojunctions. *Nano letters*, 13(3):994–999, 2013.

[6] Chia-Hao M. Chuang, Patrick R. Brown, Vladimir Bulović, and Moungi G. Bawendi. Improved performance and stability in quantum dot solar cells through band alignment engineering. *Nature Materials*, 13(8):796–801, August 2014.

[7] Gerasimos Konstantatos, Ian Howard, Armin Fischer, Sjoerd Hoogland, Jason Clifford, Ethan Klem, Larissa Levina, and Edward H Sargent. Ultrasensitive solution-cast quantum dot photodetectors. *Nature*, 442(7099):180–183, 2006.

[8] F Pelayo García de Arquer, Ardalan Armin, Paul Meredith, and Edward H Sargent. Solution-processed semiconductors for next-generation photodetectors. *Nature Reviews Materials*, 2(3):1–17, 2017.

[9] Vicki L Colvin, Michael C Schlamp, and A Paul Alivisatos. Light-emitting diodes made from cadmium selenide nanocrystals and a semiconducting polymer. *Nature*, 370(6488):354–357, 1994.

[10] Xingliang Dai, Zhenxing Zhang, Yizheng Jin, Yuan Niu, Hujia Cao, Xiaoyong Liang, Liwei Chen, Jianpu Wang, and Xiaogang Peng. Solution-processed, high-performance light-emitting diodes based on quantum dots. *Nature*, 515(7525):96–99, November 2014.

[11] Yasuhiro Shirasaki, Geoffrey J. Supran, Moungi G. Bawendi, and Vladimir Bulović. Emergence of colloidal quantum-dot light-emitting technologies. *Nature Photonics*, 7(1):13–23, January 2013.

[12] Igor L Medintz, H Tetsuo Uyeda, Ellen R Goldman, and Hedi Mattoussi. Quantum dot bioconjugates for imaging, labelling and sensing. *Nature materials*, 4(6):435–446, 2005.

[13] Paul Alivisatos. The use of nanocrystals in biological detection. *Nature Biotechnology*, 22(1):47–52, January 2004.

[14] Jin Young Kim, Oleksandr Voznyy, David Zhitomirsky, and Edward H. Sargent. 25th Anniversary Article: Colloidal Quantum Dot Materials and Devices: A Quarter-Century of Advances. *Advanced Materials*, 25(36):4986–5010, 2013.

[15] Peter Reiss, Myriam Protière, and Liang Li. Core/Shell Semiconductor Nanocrystals. *Small*, 5(2):154–168, 2009.

[16] V. I. Klimov, D. W. McBranch, C. A. Leatherdale, and M. G. Bawendi. Electron and hole relaxation pathways in semiconductor quantum dots. *Phys. Rev. B*, 60(19):13740–13749, November 1999.

[17] Al. L. Efros and M. Rosen. The Electronic Structure of Semiconductor Nanocrystals. *Annual Review of Materials Science*, 30(1):475–521, 2000.

[18] S. Pokrant and K.B. Whaley. Tight-binding studies of surface effects on electronic structure of CdSe nanocrystals: the role of organic ligands, surface reconstruction, and inorganic capping shells. *Eur. Phys. J. D*, 6(2):255–267, May 1999.

[19] Pranab Sarkar, Michael Springborg, and Gotthard Seifert. A theoretical study of the structural and electronic properties of CdSe/CdS and CdS/CdSe core/shell nanoparticles. *Chemical Physics Letters*, 405(1):103–107, March 2005.

[20] Kelly L. Sowers, Zhentao Hou, Jeffrey J. Peterson, Brett Swartz, Sougata Pal, Oleg Prezhdo, and Todd D. Krauss. Photophysical Properties of CdSe/CdS core/shell quantum dots with tunable surface composition. *Chemical Physics*, 471:24–31, June 2016.

[21] Youngjin Jang, Arthur Shapiro, Maya Isarov, Anna Rubin-Brusilovski, Aron Safran, Adam K. Budniak, Faris Horani, Joanna Dehnel, Aldona Sashchiuk, and Efrat Lifshitz. Interface control of electronic and optical properties in

IV–VI and II–VI core/shell colloidal quantum dots: a review. *Chem. Commun.*, 53(6):1002–1024, January 2017.

[22] Svetlana V. Kilina, Patrick K. Tamukong, and Dmitri S. Kilin. Surface Chemistry of Semiconducting Quantum Dots: Theoretical Perspectives. *Acc. Chem. Res.*, 49(10):2127–2135, October 2016.

[23] Zhi-Jun Li, Jiu-Ju Wang, Xu-Bing Li, Xiang-Bing Fan, Qing-Yuan Meng, Ke Feng, Bin Chen, Chen-Ho Tung, and Li-Zhu Wu. An Exceptional Artificial Photocatalyst, Nih-CdSe/CdS Core/Shell Hybrid, Made In Situ from CdSe Quantum Dots and Nickel Salts for Efficient Hydrogen Evolution. *Advanced Materials*, 25(45):6613–6618, 2013.

[24] Jon A. Bender, Emily K. Raulerson, Xin Li, Tamar Goldzak, Pan Xia, Troy Van Voorhis, Ming Lee Tang, and Sean T. Roberts. Surface States Mediate Triplet Energy Transfer in Nanocrystal–Acene Composite Systems. *J. Am. Chem. Soc.*, 140(24):7543–7553, June 2018.

[25] Yun Ye, Xiuli Wang, Sheng Ye, Yuxing Xu, Zhaochi Feng, and Can Li. Charge-Transfer Dynamics Promoted by Hole Trap States in CdSe Quantum Dots–Ni2+ Photocatalytic System. *J. Phys. Chem. C*, 121(32):17112–17120, August 2017.

[26] Gangcheng Yuan, Daniel E. Gómez, Nicholas Kirkwood, Klaus Boldt, and Paul Mulvaney. Two Mechanisms Determine Quantum Dot Blinking. *ACS Nano*, 12(4):3397–3405, April 2018.

[27] Pavel A. Frantsuzov, Sándor Volkán-Kacsó, and Bolizsár Jankó. Model of Fluorescence Intermittency of Single Colloidal Semiconductor Quantum Dots Using Multiple Recombination Centers. *Phys. Rev. Lett.*, 103(20):207402, November 2009.

[28] Svetlana Kilina, Sergei Ivanov, and Sergei Tretiak. Effect of Surface Ligands on Optical and Electronic Spectra of Semiconductor Nanoclusters. *J. Am. Chem. Soc.*, 131(22):7717–7726, June 2009.

[29] Nicola A. Hill and K. Birgitta Whaley. A theoretical study of the influence of the surface on the electronic structure of CdSe nanoclusters. *J. Chem. Phys.*, 100(4):2831–2837, February 1994.

[30] Marco Califano, Alberto Franceschetti, and Alex Zunger. Temperature Dependence of Excitonic Radiative Decay in CdSe Quantum Dots: The Role of Surface Hole Traps. *Nano Lett.*, 5(12):2360–2364, December 2005.

[31] Alberto Franceschetti and Alex Zunger. Optical transitions in charged CdSe quantum dots. *Phys. Rev. B*, 62(24):R16287–R16290, December 2000.

[32] Sean A. Fischer, Angela M. Crotty, Svetlana V. Kilina, Sergei A. Ivanov, and Sergei Tretiak. Passivating ligand and solvent contributions to the electronic

properties of semiconductor nanocrystals. *Nanoscale*, 4(3):904–914, January 2012.

[33] Brianna R. Watson, Benjamin Doughty, and Tessa R. Calhoun. Energetics at the Surface: Direct Optical Mapping of Core and Surface Electronic Structure in CdSe Quantum Dots Using Broadband Electronic Sum Frequency Generation Microspectroscopy. *Nano Lett.*, 19(9):6157–6165, September 2019.

[34] James K. Utterback, R. Peyton Cline, Katherine E. Shulenberger, Joel D. Eaves, and Gordana Dukovic. The Motion of Trapped Holes on Nanocrystal Surfaces. *J. Phys. Chem. Lett.*, 11(22):9876–9885, November 2020.

[35] Arjan J. Houtepen, Zeger Hens, Jonathan S. Owen, and Ivan Infante. On the Origin of Surface Traps in Colloidal II–VI Semiconductor Nanocrystals. *Chem. Mater.*, 29(2):752–761, January 2017.

[36] Ou Chen, Jing Zhao, Vikash P. Chauhan, Jian Cui, Cliff Wong, Daniel K. Harris, He Wei, Hee-Sun Han, Dai Fukumura, Rakesh K. Jain, and Moungi G. Bawendi. Compact high-quality CdSe–CdS core–shell nanocrystals with narrow emission linewidths and suppressed blinking. *Nature Mater*, 12(5):445–451, May 2013.

[37] Nicholas Kirkwood, Julius O. V. Monchen, Ryan W. Crisp, Gianluca Grimaldi, Huub A. C. Bergstein, Indy du Fossé, Ward van der Stam, Ivan Infante, and Arjan J. Houtepen. Finding and Fixing Traps in II–VI and III–V Colloidal Quantum Dots: The Importance of Z-Type Ligand Passivation. *J. Am. Chem. Soc.*, 140(46):15712–15723, November 2018.

[38] Jennifer A. Hollingsworth. Heterostructuring Nanocrystal Quantum Dots Toward Intentional Suppression of Blinking and Auger Recombination. *Chem. Mater.*, 25(8):1318–1331, April 2013.

[39] Umme Farva and Chinho Park. Influence of thermal annealing on the structural and optical properties of CdSe nanoparticles. *Solar Energy Materials and Solar Cells*, 94(2):303–309, February 2010.

[40] Al. L. Efros. Luminescence polarization of CdSe microcrystals. *Phys. Rev. B*, 46(12):7448–7458, September 1992.

[41] Lin-Wang Wang and Alex Zunger. Local-density-derived semiempirical pseudopotentials. *Phys. Rev. B*, 51(24):17398–17416, June 1995.

[42] P. E. Lippens and M. Lannoo. Calculation of the band gap for small CdS and ZnS crystallites. *Phys. Rev. B*, 39(15):10935–10942, May 1989.

[43] Svetlana Kilina, Dmitri Kilin, and Sergei Tretiak. Light-Driven and Phonon-Assisted Dynamics in Organic and Semiconductor Nanostructures. *Chem. Rev.*, 115(12):5929–5978, June 2015.

[44] Aaron Puzder, A. J. Williamson, François Gygi, and Giulia Galli. Self-Healing of CdSe Nanocrystals: First-Principles Calculations. *Phys. Rev. Lett.*, 92(21):217401, May 2004.

[45] M. Yu, G. W. Fernando, R. Li, F. Papadimitrakopoulos, N. Shi, and R. Ramprasad. First principles study of CdSe quantum dots: Stability, surface unsaturations, and experimental validation. *Appl. Phys. Lett.*, 88(23):231910, June 2006.

[46] Victor V. Albert, Sergei A. Ivanov, Sergei Tretiak, and Svetlana V. Kilina. Electronic Structure of Ligated CdSe Clusters: Dependence on DFT Methodology. *J. Phys. Chem. C*, 115(32):15793–15800, August 2011.

[47] Nathaniel K. Swenson, Mark A. Ratner, and Emily A. Weiss. Computational Study of the Influence of the Binding Geometries of Organic Ligands on the Photoluminescence Quantum Yield of CdSe Clusters. *J. Phys. Chem. C*, 120(12):6859–6868, March 2016.

[48] Andreas Dreuw and Martin Head-Gordon. Single-Reference ab Initio Methods for the Calculation of Excited States of Large Molecules. *Chem. Rev.*, 105(11):4009–4037, November 2005.

[49] E. Lifshitz, A. Glozman, I. D. Litvin, and H. Porteanu. Optically Detected Magnetic Resonance Studies of the Surface/Interface Properties of II-VI Semiconductor Quantum Dots. *J. Phys. Chem. B*, 104(45):10449–10461, November 2000.

[50] Jacek Jasieniak and Paul Mulvaney. From Cd-Rich to Se-Rich - the Manipulation of CdSe Nanocrystal Surface Stoichiometry. *J. Am. Chem. Soc.*, 129(10):2841–2848, March 2007.

[51] Jonathan Mooney, Michael M. Krause, Jonathan I. Saari, and Patanjali Kambhampati. Challenge to the deep-trap model of the surface in semiconductor nanocrystals. *Phys. Rev. B*, 87(8):081201, February 2013.

[52] Gianluca Grimaldi, Jaco J. Geuchies, Ward van der Stam, Indy du Fossé, Baldur Brynjarsson, Nicholas Kirkwood, Sachin Kinge, Laurens D.A. Siebbeles, and Arjan J. Houtepen. Spectroscopic Evidence for the Contribution of Holes to the Bleach of Cd-Chalcogenide Quantum Dots. *Nano Lett.*, 19(5):3002–3010, May 2019.

[53] Shangxin Lin, Jiongzhao Li, Chaodan Pu, Hairui Lei, Meiyi Zhu, Haiyan Qin, and Xiaogang Peng. Surface and intrinsic contributions to extinction properties of ZnSe quantum dots. *Nano Res.*, 13(3):824–831, March 2020.

[54] K. Leung and K. B. Whaley. Surface relaxation in CdSe nanocrystals. *J. Chem. Phys.*, 110(22):11012–11022, May 1999.

[55] Francisco M. Gómez-Campos and Marco Califano. Hole Surface Trapping in CdSe Nanocrystals: Dynamics, Rate Fluctuations, and Implications for Blinking. *Nano Lett.*, 12(9):4508–4517, September 2012.

[56] Hung-Lung Chou, Chih-Hsiang Tseng, K. Chandrasekara Pillai, Bing-Joe Hwang, and Liang-Yih Chen. Adsorption and binding of capping molecules for highly luminescent CdSe nanocrystals – DFT simulation studies. *Nanoscale*, 2(12):2679–2684, December 2010.

[57] Mauro Del Ben, Remco W. A. Havenith, Ria Broer, and Mauro Stener. Density Functional Study on the Morphology and Photoabsorption of CdSe Nanoclusters. *J. Phys. Chem. C*, 115(34):16782–16796, September 2011.

[58] M. Yu, G. W. Fernando, R. Li, F. Papadimitrakopoulos, N. Shi, and R. Ramprasad. Discrete size series of CdSe quantum dots: a combined computational and experimental investigation. *J Computer-Aided Mater Des*, 14(1):167–174, April 2007.

[59] O. Voznyy and E.H. Sargent. Atomistic Model of Fluorescence Intermittency of Colloidal Quantum Dots. *Phys. Rev. Lett.*, 112(15):157401, April 2014.

[60] Yingqi Cui, Xianhui Cui, Li Zhang, Yujuan Xie, and Mingli Yang. Theoretical characterization on the size-dependent electron and hole trapping activity of chloride-passivated CdSe nanoclusters. *The Journal of Chemical Physics*, 148(13):134308, April 2018.

[61] C. Bullen and P. Mulvaney. The Effects of Chemisorption on the Luminescence of CdSe Quantum Dots. *Langmuir*, 22(7):3007–3013, March 2006.

[62] M. Claudia Troparevsky, Leeor Kronik, and James R. Chelikowsky. Optical properties of CdSe quantum dots. *The Journal of Chemical Physics*, 119(4):2284–2287, July 2003.

[63] Silvana Botti and Miguel A. L. Marques. Identification of fullerene-like CdSe nanoparticles from optical spectroscopy calculations. *Phys. Rev. B*, 75(3):035311, January 2007.

[64] Li Wang, Kouhei Nonaka, Tomoki Okuhata, Tetsuro Katayama, and Naoto Tamai. Quasi-Type II Carrier Distribution in CdSe/CdS Core/Shell Quantum Dots with Type I Band Alignment. *J. Phys. Chem. C*, 122(22):12038–12046, June 2018.

[65] Degui Kong, Yanyan Jia, Yueping Ren, Zhaoxiong Xie, Kaifeng Wu, and Tianquan Lian. Shell-Thickness-Dependent Biexciton Lifetime in Type I and Quasi-Type II CdSe@CdS Core/Shell Quantum Dots. *J. Phys. Chem. C*, 122(25):14091–14098, June 2018.

[66] Bao-Hua Zhu, Hui-Chao Zhang, Zong-Yan Zhang, Yi-Ping Cui, and Jia-Yu Zhang. Effect of shell thickness on two-photon absorption and refraction of colloidal CdSe/CdS core/shell nanocrystals. *Appl. Phys. Lett.*, 99(23):231903, December 2011.

[67] U. Banin, M. Bruchez, A. P. Alivisatos, T. Ha, S. Weiss, and D. S. Chemla. Evidence for a thermal contribution to emission intermittency in single CdSe/CdS core/shell nanocrystals. *J. Chem. Phys.*, 110(2):1195–1201, December 1998.

[68] Daniel E. Gómez, Joel van Embden, Paul Mulvaney, Mark J. Fernée, and Halina Rubinsztein-Dunlop. Exciton-Trion Transitions in Single CdSe-CdS Core-Shell Nanocrystals. *ACS Nano*, 3(8):2281–2287, August 2009.

[69] Jingbo Li and Lin-Wang Wang. First principle study of core/shell structure quantum dots. *Appl. Phys. Lett.*, 84(18):3648–3650, April 2004.

[70] V. Kocevski, J. Rusz, O. Eriksson, and D. D. Sarma. First-principles study of the influence of different interfaces and core types on the properties of CdSe/CdS core-shell nanocrystals. *Scientific Reports*, 5(1):10865, June 2015.

[71] V. Kocevski, O. Eriksson, C. Gerard, D. D. Sarma, and J. Rusz. Influence of dimensionality and interface type on optical and electronic properties of CdS/ZnS core-shell nanocrystals—A first-principles study. *J. Chem. Phys.*, 143(16):164701, October 2015.

[72] Caroline Murawski, Karl Leo, and Malte C. Gather. Efficiency Roll-Off in Organic Light-Emitting Diodes. *Adv. Mater.*, 25(47):6801–6827, December 2013.

[73] Irma Slowik, Axel Fischer, Hartmut Fröb, Simone Lenk, Sebastian Reineke, and Karl Leo. Novel organic light-emitting diode design for future lasing applications. *Organic Electronics*, 48:132 – 137, 2017.

[74] F. J. Duarte, L. S. Liao, and K. M. Vaeth. Coherence characteristics of electrically excited tandem organic light-emitting diodes. *Opt. Lett.*, 30(22):3072–3074, November 2005.

[75] Alexander J. C. Kuehne and Malte C. Gather. Organic Lasers: Recent Developments on Materials, Device Geometries, and Fabrication Techniques. *Chem. Rev.*, 116(21):12823–12864, November 2016.

[76] Sébastien Chénais and Sébastien Forget. Recent advances in solid-state organic lasers. *Polym. Int.*, 61(3):390–406, March 2012.

[77] I. D. W. Samuel and G. A. Turnbull. Organic Semiconductor Lasers. *Chem. Rev.*, 107(4):1272–1295, April 2007.

[78] R. Brückner, A. A. Zakhidov, R. Scholz, M. Sudzius, S. I. Hintschich, H. Fröb, V. G. Lyssenko, and K. Leo. Phase-locked coherent modes in a patterned metal-organic microcavity. *Nat Photon*, 6(5):322–326, May 2012.

[79] Y. Yang, G. A. Turnbull, and I. D. W. Samuel. Hybrid optoelectronics: A polymer laser pumped by a nitride light-emitting diode. *Appl. Phys. Lett.*, 92(16):163306, April 2008.

[80] Hisahiro Sasabe and Junji Kido. Multifunctional Materials in High-Performance OLEDs: Challenges for Solid-State Lighting. *Chem. Mater.*, 23(3):621–630, February 2011.

[81] B. W. D'Andrade and S. R. Forrest. White Organic Light-Emitting Devices for Solid-State Lighting. *Advanced Materials*, 16(18):1585–1595, September 2004.

[82] Y. Chang and Z. Lu. White Organic Light-Emitting Diodes for Solid-State Lighting. *Journal of Display Technology*, 9(6):459–468, June 2013.

[83] Min-Ho Park, Tae-Hee Han, Young-Hoon Kim, Su-Hun Jeong, Yeongjun Lee, Hong-Kyu Seo, Himchan Cho, and Tae-Woo Lee. Flexible organic light-emitting diodes for solid-state lighting. *JPE*, 5(1):053599, July 2015.

[84] Simonas Krotkus, Daniel Kasemann, Simone Lenk, Karl Leo, and Sebastian Reineke. Adjustable white-light emission from a photo-structured micro-OLED array. *Light: Science & Applications*, 5(7):e16121, July 2016.

[85] Lei Ding, Shou-Cheng Dong, Zuo-Quan Jiang, Hua Chen, and Liang-Sheng Liao. Orthogonal Molecular Structure for Better Host Material in Blue Phosphorescence and Larger OLED White Lighting Panel. *Advanced Functional Materials*, 25(4):645–650, 2015.

[86] Colin J. Humphreys. Solid-State Lighting. *MRS Bulletin*, 33(4):459–470, April 2008.

[87] M. A. Baldo, C. Adachi, and S. R. Forrest. Transient analysis of organic electrophosphorescence. II. Transient analysis of triplet-triplet annihilation. *Phys. Rev. B*, 62(16):10967–10977, October 2000.

[88] Sebastian Reineke, Karsten Walzer, and Karl Leo. Triplet-exciton quenching in organic phosphorescent light-emitting diodes with Ir-based emitters. *Phys. Rev. B*, 75(12):125328, March 2007.

[89] Dandan Song, Suling Zhao, Yichun Luo, and Hany Aziz. Causes of efficiency roll-off in phosphorescent organic light emitting devices: Triplet-triplet annihilation versus triplet-polaron quenching. *Appl. Phys. Lett.*, 97(24):243304, December 2010.

[90] Taro Furukawa, Hajime Nakanotani, Munetomo Inoue, and Chihaya Adachi. Dual enhancement of electroluminescence efficiency and operational stability by rapid upconversion of triplet excitons in OLEDs. *Scientific Reports*, 5:8429, February 2015.

[91] Sebastian Wehrmeister, Lars Jäger, Thomas Wehlus, Andreas F. Rausch, Thilo C. G. Reusch, Tobias D. Schmidt, and Wolfgang Brütting. Combined Electrical and Optical Analysis of the Efficiency Roll-Off in Phosphorescent Organic Light-Emitting Diodes. *Phys. Rev. Applied*, 3(2):024008, February 2015.

[92] J. Kalinowski, W. Stampor, J. Mężyk, M. Cocchi, D. Virgili, V. Fattori, and P. Di Marco. Quenching effects in organic electrophosphorescence. *Phys. Rev. B*, 66(23):235321, December 2002.

[93] Murat Mesta, Marco Carvelli, Rein J. de Vries, Harm van Eersel, Jeroen J. M. van der Holst, Matthias Schober, Mauro Furno, Björn Lüssem, Karl Leo, Peter Loebl, and *et al.* Molecular-scale simulation of electroluminescence in a multilayer white organic light-emitting diode. *Nat. Mater.*, 12(7):652–658, July 2013.

[94] Arnout Ligthart, Xander de Vries, Le Zhang, Mike C. W. M. Pols, Peter A. Bobbert, Harm van Eersel, and Reinder Coehoorn. Effect of Triplet Confinement on Triplet–Triplet Annihilation in Organic Phosphorescent Host–Guest Systems. *Advanced Functional Materials*, 28(52):1804618, 2018.

[95] Weifeng Zhou, Christoph Zimmermann, and Christoph Jungemann. Master equation study of excitonic processes limiting the luminous efficacy in phosphorescent organic light-emitting diodes. *Journal of Applied Physics*, 125(16):165501, April 2019.

[96] Reinder Coehoorn, Harm van Eersel, Peter Bobbert, and René Janssen. Kinetic Monte Carlo Study of the Sensitivity of OLED Efficiency and Lifetime to Materials Parameters. *Advanced Functional Materials*, 25(13):2024–2037, April 2015.

[97] H. van Eersel, P. A. Bobbert, R. A. J. Janssen, and R. Coehoorn. Monte Carlo study of efficiency roll-off of phosphorescent organic light-emitting diodes: Evidence for dominant role of triplet-polaron quenching. *Appl. Phys. Lett.*, 105(14):143303, October 2014.

[98] Yufei Shen and Noel C. Giebink. Monte Carlo Simulations of Nanoscale Electrical Inhomogeneity in Organic Light-Emitting Diodes and Its Impact on Their Efficiency and Lifetime. *Phys. Rev. Applied*, 4(5):054017, November 2015.

[99] S. Gottardi, M. Barbry, R. Coehoorn, and H. van Eersel. Efficiency loss processes in hyperfluorescent OLEDs: A kinetic Monte Carlo study. *Appl. Phys. Lett.*, 114(7):073301, February 2019.

[100] Nadav Geva, Valerie Vaissier, James Shepherd, and Troy Van Voorhis. Mean field treatment of heterogeneous steady state kinetics. *Chemical Physics Letters*, 685:185–190, October 2017.

[101] Tamar Goldzak*, Alexandra R. McIsaac*, and Troy Van Voorhis. Colloidal CdSe nanocrystals are inherently defective. *Nature Communications*, 12(1):890, February 2021.

[102] Louis Brus. Electronic wave functions in semiconductor clusters: experiment and theory. *J. Phys. Chem.*, 90(12):2555–2560, June 1986.

[103] A. P. Alivisatos. Semiconductor Clusters, Nanocrystals, and Quantum Dots. *Science*, 271(5251):933–937, February 1996.

[104] M G Bawendi, M L Steigerwald, and L E Brus. The Quantum Mechanics of Larger Semiconductor Clusters ("Quantum Dots"). *Annual Review of Physical Chemistry*, 41(1):477–496, October 1990.

[105] C. B. Murray, D. J. Norris, and M. G. Bawendi. Synthesis and characterization of nearly monodisperse CdE (E = sulfur, selenium, tellurium) semiconductor nanocrystallites. *J. Am. Chem. Soc.*, 115(19):8706–8715, September 1993.

[106] Xiaogang Peng, Liberato Manna, Weidong Yang, Juanita Wickham, Erik Scher, Andreas Kadavanich, and A. P. Alivisatos. Shape control of CdSe nanocrystals. *Nature*, 404(6773):59, March 2000.

[107] Jacek Jasieniak, Lisa Smith, Joel van Embden, Paul Mulvaney, and Marco Califano. Re-examination of the Size-Dependent Absorption Properties of CdSe Quantum Dots. *J. Phys. Chem. C*, 113(45):19468–19474, November 2009.

[108] D. J. Norris, Al. L. Efros, M. Rosen, and M. G. Bawendi. Size dependence of exciton fine structure in CdSe quantum dots. *Phys. Rev. B*, 53(24):16347–16354, June 1996.

[109] C R Kagan, C B Murray, M Nirmal, and M G Bawendi. Electronic Energy Transfer in CdSe Quantum Dot Solids. *PHYSICAL REVIEW LETTERS*, 76(9):4, 1996.

[110] K. T. Shimizu, R. G. Neuhauser, C. A. Leatherdale, S. A. Empedocles, W. K. Woo, and M. G. Bawendi. Blinking statistics in single semiconductor nanocrystal quantum dots. *Physical Review B*, 63(20), May 2001.

[111] Christophe Galland, Yagnaseni Ghosh, Andrea Steinbrück, Milan Sykora, Jennifer A. Hollingsworth, Victor I. Klimov, and Han Htoon. Two types of luminescence blinking revealed by spectroelectrochemistry of single quantum dots. *Nature*, 479(7372):203–207, November 2011.

[112] Sander F. Wuister, Celso de Mello Donegá, and Andries Meijerink. Influence of Thiol Capping on the Exciton Luminescence and Decay Kinetics of CdTe and CdSe Quantum Dots. *J. Phys. Chem. B*, 108(45):17393–17397, November 2004.

[113] Helen Hsiu-Ying Wei, Christopher M. Evans, Brett D. Swartz, Amanda J. Neukirch, Jeremy Young, Oleg V. Prezhdo, and Todd D. Krauss. Colloidal Semiconductor Quantum Dots with Tunable Surface Composition. *Nano Lett.*, 12(9):4465–4471, September 2012.

[114] N. Chestnoy, T. D. Harris, R. Hull, and L. E. Brus. Luminescence and photophysics of cadmium sulfide semiconductor clusters: the nature of the emitting electronic state. *J. Phys. Chem.*, 90(15):3393–3399, July 1986.

[115] Aisea Veamatahau, Bo Jiang, Tom Seifert, Satoshi Makuta, Kay Latham, Masayuki Kanehara, Toshiharu Teranishi, and Yasuhiro Tachibana. Origin of surface trap states in CdS quantum dots: relationship between size dependent photoluminescence and sulfur vacancy trap states. *Phys. Chem. Chem. Phys.*, 17(4):2850–2858, December 2014.

[116] Alina M Schimpf, Kathryn E Knowles, Gerard M Carroll, and Daniel R Gamelin. Electronic doping and redox-potential tuning in colloidal semiconductor nanocrystals. *Accounts of chemical research*, 48(7):1929–1937, 2015.

[117] Nicola A. Hill and K. Birgitta Whaley. A theoretical study of the influence of the surface on the electronic structure of CdSe nanoclusters. *The Journal of Chemical Physics*, 100(4):2831, August 1998.

[118] Nicholas J. Thompson, Mark W. B. Wilson, Daniel N. Congreve, Patrick R. Brown, Jennifer M. Scherer, Thomas S. Bischof, Mengfei Wu, Nadav Geva, Matthew Welborn, Troy Van Voorhis, Vladimir Bulović, Moungi G. Bawendi, and Marc A. Baldo. Energy harvesting of non-emissive triplet excitons in tetracene by emissive PbS nanocrystals. *Nature Materials*, 13(11):1039–1043, November 2014.

[119] Nadav Geva, James J. Shepherd, Lea Nienhaus, Moungi G. Bawendi, and Troy Van Voorhis. Morphology of Passivating Organic Ligands around a Nanocrystal. *The Journal of Physical Chemistry C*, 122(45):26267–26274, November 2018.

[120] Carlo Adamo and Vincenzo Barone. Toward reliable density functional methods without adjustable parameters: The PBE0 model. *J. Chem. Phys.*, 110(13):6158–6170, March 1999.

[121] Alejandro J Garza and Gustavo E Scuseria. Predicting band gaps with hybrid density functionals. *The journal of physical chemistry letters*, 7(20):4165–4170, 2016.

[122] Martin Head-Gordon, Ana M. Grana, David Maurice, and Christopher A. White. Analysis of Electronic Transitions as the Difference of Electron Attachment and Detachment Densities. *J. Phys. Chem.*, 99(39):14261–14270, September 1995.

[123] Ryan M. Richard and John M. Herbert. Time-Dependent Density-Functional Description of the 1La State in Polycyclic Aromatic Hydrocarbons: Charge-Transfer Character in Disguise? *J. Chem. Theory Comput.*, 7(5):1296–1306, May 2011.

[124] Carlo Giansante and Ivan Infante. Surface Traps in Colloidal Quantum Dots: A Combined Experimental and Theoretical Perspective. *J. Phys. Chem. Lett.*, 8(20):5209–5215, October 2017.

[125] Dmitri V. Talapin, Andrey L. Rogach, Andreas Kornowski, Markus Haase, and Horst Weller. Highly Luminescent Monodisperse CdSe and CdSe/ZnS Nanocrystals Synthesized in a Hexadecylamine-Trioctylphosphine Oxide-Trioctylphospine Mixture. *Nano Lett.*, 1(4):207–211, April 2001.

[126] Emily A. Weiss. Designing the Surfaces of Semiconductor Quantum Dots for Colloidal Photocatalysis. *ACS Energy Lett.*, 2(5):1005–1013, May 2017.

[127] Zhifeng Ding, Bernadette M. Quinn, Santosh K. Haram, Lindsay E. Pell, Brian A. Korgel, and Allen J. Bard. Electrochemistry and electrogenerated chemiluminescence from silicon nanocrystal quantum dots. *Science*, 296(5571):1293–1297, 2002.

[128] N. C. Greenham, Xiaogang Peng, and A. P. Alivisatos. Charge separation and transport in conjugated-polymer/semiconductor-nanocrystal composites studied by photoluminescence quenching and photoconductivity. *Phys. Rev. B*, 54(24):17628–17637, December 1996.

[129] William A. Tisdale, Kenrick J. Williams, Brooke A. Timp, David J. Norris, Eray S. Aydil, and X.-Y. Zhu. Hot-Electron Transfer from Semiconductor Nanocrystals. *Science*, 328(5985):1543–1547, June 2010.

[130] Al. L. Efros, M. Rosen, M. Kuno, M. Nirmal, D. J. Norris, and M. Bawendi. Band-edge exciton in quantum dots of semiconductors with a degenerate valence band: Dark and bright exciton states. *Phys. Rev. B*, 54(7):4843–4856, August 1996.

[131] Iwan Moreels, Gabriele Rainò, Raquel Gomes, Zeger Hens, Thilo Stöferle, and Rainer F. Mahrt. Band-Edge Exciton Fine Structure of Small, Nearly Spherical Colloidal CdSe/ZnS Quantum Dots. *ACS Nano*, 5(10):8033–8039, October 2011.

[132] M. Kuno, J. K. Lee, B. O. Dabbousi, F. V. Mikulec, and M. G. Bawendi. The band edge luminescence of surface modified CdSe nanocrystallites: Probing the luminescing state. *J. Chem. Phys.*, 106(23):9869–9882, June 1997.

[133] Sarah M. Harrell, James R. McBride, and Sandra J. Rosenthal. Synthesis of Ultrasmall and Magic-Sized CdSe Nanocrystals. *Chem. Mater.*, 25(8):1199–1210, April 2013.

[134] Jeremy A. Scher, Michael G. Bayne, Amogh Srihari, Shikha Nangia, and Arindam Chakraborty. Development of effective stochastic potential method using random matrix theory for efficient conformational sampling of semiconductor nanoparticles at non-zero temperatures. *J. Chem. Phys.*, 149(1):014103, July 2018.

[135] Aaron Puzder, A. J. Williamson, Jeffrey C. Grossman, and Giulia Galli. Surface Chemistry of Silicon Nanoclusters. *Phys. Rev. Lett.*, 88(9):097401, February 2002.

[136] Yihan Shao, Zhengting Gan, Evgeny Epifanovsky, Andrew T. B. Gilbert, Michael Wormit, Joerg Kussmann, Adrian W. Lange, Andrew Behn, Jia Deng, Xintian Feng, Debashree Ghosh, Matthew Goldey, Paul R. Horn, Leif D. Jacobson, Ilya Kaliman, Rustam Z. Khaliullin, Tomasz Kuś, Arie Landau, Jie Liu, Emil I. Proynov, Young Min Rhee, Ryan M. Richard, Mary A. Rohrdanz, Ryan P. Steele, Eric J. Sundstrom, H. Lee Woodcock III, Paul M. Zimmerman, Dmitry Zuev, Ben Albrecht, Ethan Alguire, Brian Austin, Gregory J. O. Beran, Yves A. Bernard, Eric Berquist, Kai Brandhorst, Ksenia B. Bravaya, Shawn T. Brown, David Casanova, Chun-Min Chang, Yunqing Chen, Siu Hung Chien, Kristina D. Closser, Deborah L. Crittenden, Michael Diedenhofen, Robert A. DiStasio Jr, Hainam Do, Anthony D. Dutoi, Richard G. Edgar, Shervin Fatehi, Laszlo Fusti-Molnar, An Ghysels, Anna Golubeva-Zadorozhnaya, Joseph Gomes, Magnus W. D. Hanson-Heine, Philipp H. P. Harbach, Andreas W. Hauser, Edward G. Hohenstein, Zachary C. Holden, Thomas-C. Jagau, Hyunjun Ji, Benjamin Kaduk, Kirill Khistyaev, Jaehoon Kim, Jihan Kim, Rollin A. King, Phil Klunzinger, Dmytro Kosenkov, Tim Kowalczyk, Caroline M. Krauter, Ka Un Lao, Adèle D. Laurent, Keith V. Lawler, Sergey V. Levchenko, Ching Yeh Lin, Fenglai Liu, Ester Livshits, Rohini C. Lochan, Arne Luenser, Prashant Manohar, Samuel F. Manzer, Shan-Ping Mao, Narbe Mardirossian, Aleksandr V. Marenich, Simon A. Maurer, Nicholas J. Mayhall, Eric Neuscamman, C. Melania Oana, Roberto Olivares-Amaya, Darragh P. O'Neill, John A. Parkhill, Trilisa M. Perrine, Roberto Peverati, Alexander Prociuk, Dirk R. Rehn, Edina Rosta, Nicholas J. Russ, Shaama M. Sharada, Sandeep Sharma, David W. Small, Alexander Sodt, Tamar Stein, David Stück, Yu-Chuan Su, Alex J. W. Thom, Takashi Tsuchimochi, Vitalii Vanovschi, Leslie Vogt, Oleg Vydrov, Tao Wang, Mark A. Watson, Jan Wenzel, Alec White, Christopher F. Williams, Jun Yang, Sina Yeganeh, Shane R. Yost, Zhi-Qiang You, Igor Ying Zhang, Xing Zhang, Yan Zhao, Bernard R. Brooks, Garnet K. L. Chan, Daniel M. Chipman, Christopher J. Cramer, William A. Goddard III, Mark S. Gordon, Warren J. Hehre, Andreas Klamt, Henry F. Schaefer III, Michael W. Schmidt, C. David Sherrill, Donald G. Truhlar, Arieh Warshel, Xin Xu, Alán Aspuru-Guzik, Roi Baer, Alexis T. Bell, Nicholas A. Besley, Jeng-Da Chai, Andreas Dreuw, Barry D. Dunietz, Thomas R. Furlani, Steven R. Gwaltney, Chao-Ping Hsu, Yousung Jung, Jing Kong, Daniel S. Lambrecht, WanZhen Liang, Christian Ochsenfeld, Vitaly A. Rassolov, Lyudmila V.

Slipchenko, Joseph E. Subotnik, Troy Van Voorhis, John M. Herbert, Anna I. Krylov, Peter M. W. Gill, and Martin Head-Gordon. Advances in molecular quantum chemistry contained in the Q-Chem 4 program package. *Molecular Physics*, 113(2):184–215, January 2015.

[137] John P. Perdew, Kieron Burke, and Matthias Ernzerhof. Generalized Gradient Approximation Made Simple. *Phys. Rev. Lett.*, 77(18):3865–3868, October 1996.

[138] R. Ditchfield, W. J. Hehre, and J. A. Pople. Self-Consistent Molecular-Orbital Methods. IX. An Extended Gaussian-Type Basis for Molecular-Orbital Studies of Organic Molecules. *J. Chem. Phys.*, 54(2):724–728, January 1971.

[139] W. J. Hehre, R. Ditchfield, and J. A. Pople. Self—Consistent Molecular Orbital Methods. XII. Further Extensions of Gaussian—Type Basis Sets for Use in Molecular Orbital Studies of Organic Molecules. *J. Chem. Phys.*, 56(5):2257–2261, March 1972.

[140] P. Jeffrey Hay and Willard R. Wadt. Ab initio effective core potentials for molecular calculations. Potentials for the transition metal atoms Sc to Hg. *J. Chem. Phys.*, 82(1):270–283, January 1985.

[141] Willard R. Wadt and P. Jeffrey Hay. Ab initio effective core potentials for molecular calculations. Potentials for main group elements Na to Bi. *J. Chem. Phys.*, 82(1):284–298, January 1985.

[142] Eran Rabani. Structure and electrostatic properties of passivated CdSe nanocrystals. *J. Chem. Phys.*, 115(3):1493–1497, July 2001.

[143] Somesh Kr. Bhattacharya and Anjali Kshirsagar. First principle study of free and surface terminated CdTe nanoparticles. *Eur. Phys. J. D*, 48(3):355–364, July 2008.

[144] Liberato Manna, Wang, Roberto Cingolani, and A. Paul Alivisatos. First-Principles Modeling of Unpassivated and Surfactant-Passivated Bulk Facets of Wurtzite CdSe: A Model System for Studying the Anisotropic Growth of CdSe Nanocrystals. *J. Phys. Chem. B*, 109(13):6183–6192, April 2005.

[145] Hairui Lei, Yonghong Wang, Shaojie Liu, Meiyi Zhu, Chaodan Pu, Shangxin Lin, Haiyan Qin, and Xiaogang Peng. Delocalized Surface Electronic States on Polar Facets of Semiconductor Nanocrystals. *ACS Nano*, 14(12):16614–16623, December 2020.

[146] Vladimir Baturin, Sergey Lepeshkin, Natalia Bushlanova, and Yurii Uspenskii. Atomistic origins of charge traps in CdSe nanoclusters. *Phys. Chem. Chem. Phys.*, 22(45):26299–26305, November 2020.

[147] Svetlana V. Kilina, Amanda J. Neukirch, Bradley F. Habenicht, Dmitri S. Kilin, and Oleg V. Prezhdo. Quantum Zeno Effect Rationalizes the Phonon Bottleneck in Semiconductor Quantum Dots. *Phys. Rev. Lett.*, 110(18):180404, May 2013.

[148] Dmitri S. Kilin, Kiril Tsemekhman, Oleg V. Prezhdo, Eduard I. Zenkevich, and Christian von Borczyskowski. Ab initio study of exciton transfer dynamics from a core–shell semiconductor quantum dot to a porphyrin-sensitizer. *Journal of Photochemistry and Photobiology A: Chemistry*, 190(2):342–351, August 2007.

[149] Mariami Rusishvili, Stefan Wippermann, Dmitri V. Talapin, and Giulia Galli. Stoichiometry of the Core Determines the Electronic Structure of Core–Shell III–V/II–VI Nanoparticles. *Chem. Mater.*, 32(22):9798–9804, November 2020.

[150] Thomas D. Kühne, Marcella Iannuzzi, Mauro Del Ben, Vladimir V. Rybkin, Patrick Seewald, Frederick Stein, Teodoro Laino, Rustam Z. Khaliullin, Ole Schütt, Florian Schiffmann, Dorothea Golze, Jan Wilhelm, Sergey Chulkov, Mohammad Hossein Bani-Hashemian, Valéry Weber, Urban Borštnik, Mathieu Taillefumier, Alice Shoshana Jakobovits, Alfio Lazzaro, Hans Pabst, Tiziano Müller, Robert Schade, Manuel Guidon, Samuel Andermatt, Nico Holmberg, Gregory K. Schenter, Anna Hehn, Augustin Bussy, Fabian Belleflamme, Gloria Tabacchi, Andreas Glöß, Michael Lass, Iain Bethune, Christopher J. Mundy, Christian Plessl, Matt Watkins, Joost VandeVondele, Matthias Krack, and Jürg Hutter. CP2K: An electronic structure and molecular dynamics software package - Quickstep: Efficient and accurate electronic structure calculations. *J. Chem. Phys.*, 152(19):194103, May 2020.

[151] S. Goedecker, M. Teter, and J. Hutter. Separable dual-space Gaussian pseudopotentials. *Phys. Rev. B*, 54(3):1703–1710, July 1996.

[152] Joost VandeVondele and Jürg Hutter. Gaussian basis sets for accurate calculations on molecular systems in gas and condensed phases. *J. Chem. Phys.*, 127(11):114105, September 2007.

[153] D. Pan, Q. Wang, S. Jiang, X. Ji, and L. An. Synthesis of Extremely Small CdSe and Highly Luminescent CdSe/CdS Core–Shell Nanocrystals via a Novel Two-Phase Thermal Approach. *Advanced Materials*, 17(2):176–179, 2005.

[154] Anielle Christine A. Silva, Ernesto S. Freitas Neto, Sebastião W. da Silva, Paulo C. Morais, and Noelio O. Dantas. Modified Phonon Confinement Model and Its Application to CdSe/CdS Core–Shell Magic-Sized Quantum Dots Synthesized in Aqueous Solution by a New Route. *J. Phys. Chem. C*, 117(4):1904–1914, January 2013.

[155] Abhilash Sugunan, Yichen Zhao, Somak Mitra, Lin Dong, Shanghua Li, Sergei Popov, Saulius Marcinkevicius, Muhammet S. Toprak, and Mamoun Muhammed. Synthesis of tetrahedral quasi-type-II CdSe–CdS core–shell quantum dots. *Nanotechnology*, 22(42):425202, September 2011. Publisher: IOP Publishing.

[156] Partha Maity, Tushar Debnath, and Hirendra N. Ghosh. Ultrafast Charge Carrier Delocalization in CdSe/CdS Quasi-Type II and CdS/CdSe Inverted Type I Core–Shell: A Structural Analysis through Carrier-Quenching Study. *J. Phys. Chem. C*, 119(46):26202–26211, November 2015. Publisher: American Chemical Society.

[157] Alexandra R. McIsaac, Valerie Vaissier Welborn, Markus Einzinger, Nadav Geva, Hayley Weir, Marc A. Baldo, and Troy Van Voorhis. Investigation of External Quantum Efficiency Roll-Off in OLEDs Using the Mean-Field Steady-State Kinetic Model. *J. Phys. Chem. C*, 124(27):14424–14431, July 2020.

[158] L. Zhang, H. van Eersel, P. A. Bobbert, and R. Coehoorn. Clarifying the mechanism of triplet–triplet annihilation in phosphorescent organic host–guest systems: A combined experimental and simulation study. *Chemical Physics Letters*, 652:142–147, May 2016.

[159] Kenichi Goushi, Kou Yoshida, Keigo Sato, and Chihaya Adachi. Organic light-emitting diodes employing efficient reverse intersystem crossing for triplet-to-singlet state conversion. *Nature Photonics*, 6(4):253–258, April 2012.

[160] Hiroki Uoyama, Kenichi Goushi, Katsuyuki Shizu, Hiroko Nomura, and Chihaya Adachi. Highly efficient organic light-emitting diodes from delayed fluorescence. *Nature*, 492(7428):234–238, December 2012.

[161] Takashi Kobayashi, Akitsugu Niwa, Kensho Takaki, Shota Haseyama, Takashi Nagase, Kenichi Goushi, Chihaya Adachi, and Hiroyoshi Naito. Contributions of a Higher Triplet Excited State to the Emission Properties of a Thermally Activated Delayed-Fluorescence Emitter. *Phys. Rev. Applied*, 7(3):034002, March 2017.

[162] Markus Einzinger, Tianyu Zhu, Piotr de Silva, Christian Belger, Timothy M. Swager, Troy Van Voorhis, and Marc A. Baldo. Shorter Exciton Lifetimes via an External Heavy-Atom Effect: Alleviating the Effects of Bimolecular Processes in Organic Light-Emitting Diodes. *Advanced Materials*, 29(40):1701987, 2017.

[163] Toshiya Yonehara, Kenichi Goushi, Tomoaki Sawabe, Isao Takasu, and Chihaya Adachi. Comparison of transient state and steady state exciton–exciton annihilation rates based on Förster-type energy transfer. *Japanese Journal of Applied Physics*, 54(7):071601, 2015.

[164] Sebastian Reineke, Thomas C. Rosenow, Björn Lüssem, and Karl Leo. Improved High-Brightness Efficiency of Phosphorescent Organic LEDs Comprising Emitter Molecules with Small Permanent Dipole Moments. *Advanced Materials*, 22(29):3189–3193, August 2010.

[165] H. van Eersel, P. A. Bobbert, and R. Coehoorn. Kinetic Monte Carlo study of triplet-triplet annihilation in organic phosphorescent emitters. *Journal of Applied Physics*, 117(11):115502, March 2015.